

DESIGN AND PERFORMANCE ANALYSIS OF GAS AND LIQUID RADIAL TURBINES

By

Xu Tan

A DISSERTATION

Submitted to  
Michigan State University  
in partial fulfillment of the requirements  
for the degree of

Mechanical Engineering – Doctor of Philosophy

2016

## **ABSTRACT**

### **DESIGN AND PERFORMANCE ANALYSIS OF GAS AND LIQUID RADIAL TURBINES**

By

Xu Tan

In the first part of the research, pumps running in reverse as turbines are studied. This work uses experimental data of wide range of pumps representing the centrifugal pumps' configurations in terms of specific speed. Based on specific speed and specific diameter an accurate correlation is developed to predict the performances at best efficiency point of the centrifugal pump in its turbine mode operation. The proposed prediction method yields very good results to date compared to previous such attempts. The present method is compared to nine previous methods found in the literature. The comparison results show that the method proposed in this paper is the most accurate. The proposed method can be further complemented and supplemented by more future tests to increase its accuracy. The proposed method is meaningful because it is based both specific speed and specific diameter.

The second part of the research is focused on the design and analysis of the radial gas turbine. The specification of the turbine is obtained from the solar biogas hybrid system. The system is theoretically analyzed and constructed based on the purchased compressor. Theoretical analysis results in a specification of 100lb/min, 900°C inlet total temperature and 1.575atm inlet total pressure.

1-D and 3-D geometry of the rotor is generated based on Aungier's method. 1-D loss model analysis and 3-D CFD simulations are performed to examine the performances of the rotor. The total-to-total efficiency of the rotor is more than 90%. With the help of CFD analysis,

modifications on the preliminary design obtained optimized aerodynamic performances. At last, the theoretical performance analysis on the hybrid system is performed with the designed turbine.

Copyright by  
XU TAN  
2016

## **ACKNOWLEDGMENTS**

In the beginning of this dissertation, I must express my special gratitude to people who supported me to finish this work. First, to my beautiful wife Ting and lovely son Alex who are the power that drives me move forward, they give me a home where I can relax and charge. Second, I thank my parents who brought me to this world and raised me up. Third, to my parents-in-law, they allowed me their beloved daughter and helped me take care of my wife and son when they were in China. Fourth, special thanks to Dr. Engeda, he provided me not only the funding but also the valuable knowledges and experiences to finish the research. Fifth, I thank the other members of my committee, Dr. Benard, Dr. Mueller and Dr. Liao, for their patience and cooperation that allowed me to finish the comprehensive exam and dissertation. Lastly, special thanks to my friends and colleagues Raul and Chris Bolin for providing me important information in my studies.

## TABLE OF CONTENTS

LIST OF TABLES.....	ix
LIST OF FIGURES.....	xi
KEY TO SYMBOLS.....	xvii
CHAPTER 1. INTRODUCTION AND BACKGROUND .....	1
1.1. Radial Turbines.....	1
1.2. Application Area.....	2
1.3. Types of IFR turbines.....	3
1.4. Performance characteristic of IFR turbines .....	6
1.4.1. Turbine characteristics .....	6
1.4.2. Thermodynamics of the IFR turbines .....	11
1.5. Radial turbine design .....	14
1.5.1. Preliminary 1-D optimization .....	14
1.5.2. Quasi-3D design.....	18
1.5.3. Full 3D design.....	20
1.6. Scope, goals and organization of the thesis .....	21
CHAPTER 2. COMPONENT OF RADIAL TURBINE .....	23
2.1. The Volute.....	23
2.2. Inlet Nozzle .....	25
2.3. The Turbine Rotor.....	27
2.4. Vaneless Space .....	31
2.5. The diffuser.....	32
CHAPTER 3. PERFORMANCE PREDICTION OF CENTRIFUGAL PUMPS WHEN RUNNING AS HYDRAULIC TURBINES.....	34
3.1. Introduction .....	34
3.1.1. Significance of pump type to select the appropriate pat.....	40
3.1.2. Performance and operation at BEP and off design areas .....	41
3.1.3. Challenges.....	44
3.1.4. Performance prediction of pump as turbine.....	46
3.1.5. Performance improvement in PAT .....	51
3.2. Previous Prediction Method .....	52
3.2.1. Theoretical.....	52
3.2.2. Experimental.....	54
3.2.3. Numerical studies .....	55
3.3. Performance prediction .....	62
3.3.1. Prediction method.....	62

3.3.2. Prediction results.....	63
3.3.3. Comparison with previous methods .....	65
3.3.4. Comparison with published experiment results .....	69
3.4. Summary .....	71
CHAPTER 4. BIO-SOLAR HYBRID SYSTEM .....	74
4.1. Concept of the Bio-solar Hybrid System .....	74
4.2. Design and Construction of the system .....	75
4.2.1. Design of the system .....	75
4.2.2. The setup of the system .....	78
4.2.3. System without recuperator .....	80
4.2.4. System with Recuperator .....	82
4.3. Summary .....	85
CHAPTER 5. DESIGN AND ANALYSIS OF IFR TURBINE .....	87
5.1. 1D Preliminary Design.....	89
5.1.1. Thermodynamics properties of the working fluid .....	89
5.1.2. 1D preliminary design .....	91
5.2. Quasi 3-D blade design .....	99
5.2.1. Meridional Rotor End-Wall Contours .....	99
5.2.2. Design of Straight-Line Element Rotor Camber lines .....	103
5.3. 1-D Analysis.....	105
5.3.1. Loss Models <sup>[69]</sup> .....	105
5.3.2. 1-D Analysis results.....	106
5.4. 3D analysis.....	108
5.4.1. Model construction and meshing of the rotor in BladeGen .....	108
5.4.2. Pre-setting of 3-D analysis .....	111
5.5. 3-D analysis results.....	113
5.5.1. Velocity triangles .....	113
5.5.2. 3-D performances analysis results .....	115
5.5.3. Pressure on blade and velocity near blade .....	116
5.5.4. Flow at the inlet.....	120
5.5.5. Temperature and entropy contours on blade.....	123
5.5.6. Pressure, temperature, entropy, and velocity on meridional surface .....	124
5.5.7. Modification of meridional shroud profile .....	126
5.6. Comparison with generalized stage performance chart for design .....	131
5.7. Performances of the turbine with different working fluids.....	132
5.8. Off-design analysis .....	132
5.9. Performance analysis of the biogas-solar hybrid system with the designed turbine .....	135
5.9.1. The efficiencies of the system with the designed turbine .....	135
5.9.2. The efficiencies of the system at off-design conditions.....	136
5.10. 1-D optimization on the inlet velocities.....	139
5.10.1. Study on inlet absolute flow angle .....	139

5.10.2. Study on inlet relative flow angle .....	140
5.10.3. CFD analyses of the turbine with optimized inlet flow angle .....	142
5.11. Summary .....	143
CHAPTER 6. CONCLUSIONS .....	145
6.1. Conclusions from the research of pump as turbine .....	145
6.2. Conclusions from the research of solar biogas hybrid system .....	147
6.3. Conclusions from the design and analysis of the radial turbine .....	147
6.4. Next steps of the project .....	148
6.4.1. Studies on the solar biogas hybrid system .....	149
6.4.2. Studies on the design and analysis of the radial turbine.....	149
6.4.3. CFD simulations with different turbulence models.....	150
6.4.4. Structural analysis on the rotor .....	150
REFERENCES.....	151



## LIST OF TABLES

Table 3.1 Pumps tested – geometry details .....	41
Table 3.2 Comparison of five pumps $n_s = 0.33, 0.58, 0.83, 1.20$ and $1.52$ carefully selected .....	44
Table 3.3 Classifications of previous prediction methods .....	56
Table 3.4 Predicted performances compared with tested data.....	63
Table 3.5 Prediction results based on published data.....	71
Table 4.1 Consumptions of different kinds of fuels of the system without recuperator .....	82
Table 4.2 Consumptions of different kinds of fuels of the system with recuperator .....	85
Table 4.3 Design Specification of the Turbine .....	86
Table 5.1 Specifications for the turbine.....	87
Table 5.2 Gas components for different fuels and different systems .....	90
Table 5.3 Specific heat capacities and specific heat ratios for different gases at inlet, $900^\circ\text{C}$ .....	91
Table 5.4 1-D design results for different kinds of components .....	98
Table 5.5 Evaluation of the design.....	99
Table 5.6 Difference between the $A_m$ and average of $A_4$ and $A_5$ .....	100
Table 5.7 1-D analysis results.....	107
Table 5.8 Mesh statistics of the rotor .....	110
Table 5.9 Flow angles in 1-D calculation and 3-D simulation .....	111
Table 5.10 Values of inlet velocities .....	114
Table 5.11 Values of outlet velocities.....	115
Table 5.12 Results of performances analysis by CFX .....	116

Table 5.13 CFD Analysis results for the modified design.....	129
Table 5.14 The performances of the turbine with different combinations of working fluids ...	132
Table 5.15 System efficiencies at the design point .....	135
Table 5.16 1-D geometry with the relative inlet flow angle for the best total to static efficiencies .....	142
Table 5.17 CFX analysis results for the turbines with optimized inlet relative flow angle.....	143

## LIST OF FIGURES

Figure 1.1 Schematic of Francis Turbine.....	1
Figure 1.2 Sketch of Ljungström Steam Turbine.....	2
Figure 1.3 (a) Sketch of a cantilever turbine (b) Velocity Triangles at rotor inlet and outlet of a cantilever turbine.....	4
Figure 1.4 Layout of a 90° IFR turbine .....	5
Figure 1.5 Diagram of typical high-speed turbine characteristic <sup>[2]</sup> .....	8
Figure 1.6 Diagram Between efficiency vs Specific Speed for different Turbine <sup>[2]</sup> .....	10
Figure 1.7 Balje Diagram .....	10
Figure 1.8 h-s Diagram in an inward-flow radial turbine.....	11
Figure 1.9 Main Components of an inward-flow Radial Turbine.....	14
Figure 1.10 Position numbers designated to radial turbine components.....	15
Figure 1.11 Generalized stage performance chart for design .....	17
Figure 1.12 Hub-to-shroud sketch of a rotor blade.....	18
Figure 1.13 Blade-to-blade sketch of a rotor.....	19
Figure 1.14 The schematic of the solar-biogas hybrid energy system .....	21
Figure 2.1 The sketch of the volute geometry.....	23
Figure 2.2 Sketch of nozzle geometry.....	26
Figure 2.3 Front view of the rotor .....	30
Figure 2.4 Side view of the rotor .....	31
Figure 2.5 Sketch of the vaneless annular passage .....	32
Figure 2.6 Sketch of the diffuser geometry .....	33
Figure 3.1 Pump and Turbine mode operation for a pump with $n_s=1.20$ at constant rpm .....	36
Figure 3.2a Turbine mode operation for a pump with $n_s= 0.58$ at variable rpm .....	38

Figure 3.2b Turbine mode operation for a pump with $n_s = 1.20$ at variable rpm .....	38
Figure 3.3 Application areas of conventional hydraulic turbines and PATs .....	39
Figure 3.4 Configurations of the tested pumps - overhung end-suction with volute .....	41
Figure 3.5 Limiting boundaries of PAT .....	43
Figure 3.6 Turbine mode performance comparison for a pump with $n_s = 0.58$ & $1.20$ .....	43
Figure 3.7 Velocity triangles at the outlet of the pump and inlet of the turbine.....	45
Figure 3.8 Velocity triangles in turbine mode at part-load and over-load conditions.....	46
Figure 3.9 PAT flow corresponding to the head at zero turbine power output.....	46
Figure 3.10 Efficiency in Pump Mode vs Flow-Coefficient .....	57
Figure 3.11 Efficiency in Turbine Mode vs Flow-Coefficient .....	57
Figure 3.12 Head-Coefficient vs Flow-Coefficient in Pump Mode.....	58
Figure 3.13 Head-Coefficient vs Flow-Coefficient in Turbine Mode .....	58
Figure 3.14 Power-Coefficient vs Flow-Coefficient in Pump Mode.....	59
Figure 3.15 Power-Coefficient vs Flow-Coefficient in Turbine Mode.....	59
Figure 3.16 Specific Speeds between Pump Mode and Turbine Mode .....	60
Figure 3.17 Power Specific Speeds between Pump Mode and Turbine Mode .....	60
Figure 3.18 Specific Diameters between Pump Mode and Turbine Mode .....	61
Figure 3.19 Efficiency Ratio vs Specific Speed in Pump Mode .....	61
Figure 3.20a Comparison of Different Prediction Methods (pump 1) .....	67
Figure 3.20b Comparison of Different Prediction Methods (pump 2) .....	67
Figure 3.20c Comparison of Different Prediction Methods (pump 3).....	68
Figure 3.20d Comparison of Different Prediction Methods (pump 4) .....	68
Figure 3.21 Specific Speeds between Pump Mode and Turbine Mode with extra published data .....	69

Figure 3.22 Specific Diameters between Pump Mode and Turbine Mode with extra published data .....	70
Figure 4.1 Concept of the System.....	74
Figure 4.2 Model of the System.....	75
Figure 4.3 The scheme and calculation results of the system.....	76
Figure 4.4 Characteristics map of the compressor.....	77
Figure 4.5 3D model of the system.....	79
Figure 4.6 The actual setup of the system.....	79
Figure 4.7 System Performances vs Solar Heat without Recuperator .....	80
Figure 4.8 System Performances vs Pressure Ratio without Recuperator .....	80
Figure 4.9 System Performances vs Combustion Temperature without Recuperator .....	81
Figure 4.10 Fuel Efficiency Changes with Isentropic Efficiencies of the Turbine and Compressor without Recuperator.....	81
Figure 4.11 System Performances vs Solar Heat with Recuperator .....	82
Figure 4.12 System Performances vs exhaust temperature with recuperator .....	83
Figure 4.13 System performances vs Combustion Temperature with recuperator.....	83
Figure 4.14 System Performances vs Pressure Ratio with recuperator .....	84
Figure 4.15 Fuel efficiency changes with isentropic efficiency of the turbine and compressor with recuperator .....	85
Figure 5.1 Position numbers designated to radial turbine components.....	87
Figure 5.2 Scheme of the design process .....	88
Figure 5.3 Inlet velocity triangle of rotor.....	93
Figure 5.4 Outlet velocity triangle of the rotor .....	95
Figure 5.5 Flow chart of 1-D design .....	96
Figure 5.6 End-Wall Contours .....	101
Figure 5.7 Power-Law Shroud Contour.....	102

Figure 5.8 Power-Law shroud contours with $n$ from 2 to 9.....	102
Figure 5.9 Camber line along the contours when $n=5$ .....	104
Figure 5.10 Blade angles along the contours when $n=5$ .....	104
Figure 5.11 Meridional view in Blade Gen.....	108
Figure 5.12 Blade angles and camber lines in Blade Gen .....	109
Figure 5.13 Meshing of the rotor.....	110
Figure 5.14 Structure simulated in CFX .....	112
Figure 5.15 Flow angles in stationary frame in the rotor .....	113
Figure 5.16 Inlet velocity triangles.....	114
Figure 5.17 Outlet velocity triangles.....	114
Figure 5.18 Pressure on the blade and velocity near the blade for the design of $n=3$ .....	117
Figure 5.19 Pressure on blade and velocity near the blade for the design of $n=4$ .....	118
Figure 5.20 Pressure on blade and velocity near the blade for the design of $n=5$ .....	118
Figure 5.21 Pressure on blade and velocity near the blade for the design of $n=6$ .....	119
Figure 5.22 Pressure on blade and velocity near the blade for the design of $n=7$ .....	119
Figure 5.23 Pressure on blade and velocity near the blade for the design of $n=8$ .....	120
Figure 5.24 Pressure on blade and velocity near the blade for the design of $n=9$ .....	120
Figure 5.25 Streamlines in blade-to-blade view at spans of 0.1, 0.5 and 0.9 for designs of $n=3$ 121	
Figure 5.26 Streamlines in blade-to-blade view at spans of 0.1, 0.5 and 0.9 for designs of $n=4$ 121	
Figure 5.27 Streamlines in blade-to-blade view at spans of 0.1, 0.5 and 0.9 for designs of $n=5$ 121	
Figure 5.28 Streamlines in blade-to-blade view at spans of 0.1, 0.5 and 0.9 for designs of $n=6$ 122	
Figure 5.29 Streamlines in blade-to-blade view at spans of 0.1, 0.5 and 0.9 for designs of $n=7$ 122	
Figure 5.30 Streamlines in blade-to-blade view at spans of 0.1, 0.5 and 0.9 for designs of $n=8$ 122	
Figure 5.31 Streamlines in blade-to-blade view at spans of 0.1, 0.5 and 0.9 for designs of $n=9$ 123	

Figure 5.32 Total temperature and entropy on blade for $n=5$ .....	123
Figure 5.33 Total temperature and entropy on blade for $n=6$ .....	124
Figure 5.34 Pressure contour on meridional surface .....	124
Figure 5.35 Velocity vectors on meridional surface .....	125
Figure 5.36 Temperature contours on meridional surface .....	125
Figure 5.37 Entropy contours on meridional surface .....	126
Figure 5.38 Modification of meridional shroud profile on the design of $n=5$ .....	127
Figure 5.39 Pressure contours on the blade for the modified model .....	127
Figure 5.40 Temperature contours on the blade for the modified model .....	128
Figure 5.41 Entropy on blade for the modified model .....	128
Figure 5.42 Pressure on meridional surface .....	129
Figure 5.43 Temperature on meridional surface .....	129
Figure 5.44 Entropy on meridional surface .....	130
Figure 5.45 Streamline in blade-to-blade view at span of 0.1, 0.5, and 0.9 .....	130
Figure 5.46 Comparison between the designs and generalized performance chart .....	131
Figure 5.47 Flow chart of off design analysis .....	133
Figure 5.48 Pressure ratios at different mass flow .....	134
Figure 5.49 Total to static efficiencies at different mass flow .....	134
Figure 5.50 Total to total efficiencies at different mass flow .....	135
Figure 5.51 Scheme of the calculation of the efficiencies at off-design conditions .....	136
Figure 5.52 Characteristics of the compressor with lines to seek its performance .....	137
Figure 5.53 Performances of the system without the recuperator at various mass flows .....	138
Figure 5.54 Performances of the system with the recuperator at various mass flows .....	138
Figure 5.55 Total to static efficiencies of different turbines with different inlet absolute flow angles .....	139

Figure 5.56 Total to total efficiencies of different turbines with different absolute inlet flow angles ..... 140

Figure 5.57 Total to static efficiencies of different turbines with different absolute inlet flow angles ..... 140

Figure 5.58 Total to total efficiencies of different turbines with different absolute inlet flow angles ..... 141



## KEY TO SYMBOLS

A = area

b = rotor passage width

B = blade width (m)

C = absolute velocity

$C_p$  = specific heat at constant pressure

$C_{os}$  = Spouting velocity.

D = diameter (m)

$D_s = \frac{D_o H_b^{0.25}}{Q_b^{0.5}}$  = specific diameter

G = gravitational constant ( $m/s^2$ )

H = head (m)

i = incidence, in degrees

$K_a$  = discharge coefficients for axial tip clearances

$K_r$  = discharge coefficients for radial tip clearances

$K_{ar}$  = a cross-coupling coefficient for both axial and radial tip clearance

L = enthalpy losses for each loss mechanism

$\dot{m}$  = mass flow rate

M = Mach number

$M_{rel}$  = relative Mach number

N = rotational speed, in RPM

$N_s = \frac{\omega Q_b^{0.5}}{(gH_b)^{0.75}}$  = specific speed

P = power (kW) or static pressure (kPa)

$P_c$  = static pressure at critical point

Q = rate of flow ( $m^3/s$ )

r = mean radius

Re = Reynolds number

t = blade passage throat; blade thickness

T = static temperature

$t_{leading}$  = blade leading edge thickness

U = blade speed (m/s)

W = relative velocity or  $\dot{m}\Delta h_o$  output power

Z = Number of the blades

$\Delta H$  = prediction error in head (%)

$\Delta h_o$  = total enthalpy change

$\Delta h_{id}$  = total-to-static ideal enthalpy drop

$\Delta Q$  = prediction error in flow rate (%)

$\Delta z_R$  = stage axial length

*Greek symbols*

$\alpha$  = absolute flow angle, in degrees

$\beta$  = blade angle, in degrees

$\gamma$  = ratio of the constant volume and constant pressure heat capacity

$\mu$  = dynamic viscosity

$\rho$  = static density

$\rho_o$  = total density

$\varepsilon_a$  = axial clearance

$\varepsilon_r$  = axial clearance

$\varepsilon_b$  = back face clearance

$\eta = \frac{P_t}{\rho g H_t Q_t}$  or  $\eta = \frac{\rho g H_p Q_p}{P_p}$  = efficiency of pumps or turbines

$\eta_h = \frac{g H_p}{U_o C_{u0}}$  or  $\eta_h = \frac{U_o C_{u0}}{g H_t}$  = hydraulic efficiency

$\Phi = \frac{Q}{\omega D_o^3}$  = flow coefficient

$\Psi = \frac{g H}{(\omega D_o)^2}$  = head coefficient

$\mu = \frac{P}{\rho \omega^3 D_o^5}$  = power coefficient

$\omega$  = rotational speed (rad/s)

$\rho$  = density of water ( $\text{m}^3/\text{s}$ )

*Subscripts*

1 = Volute exit

2 = Nozzle inlet

3 = Nozzle exit

4 = Rotor inlet

5 = Rotor outlet

6 = Diffuser outlet

b = best efficiency point or blade width

c = tip clearance losses

e = exit energy losses

h = hub at rotor

i = inlet position

inc = incidence losses

m = meridional component of velocity

o = outlet position

p = pump

p = passage losses

r = ratio

t = total thermodynamic parameter

ts = total to static

tt= total to total

rms = root mean square

s = shroud at rotor

t = turbine

u = tangential component of velocity

w = windage losses

## CHAPTER 1. INTRODUCTION AND BACKGROUND

### 1.1. Radial Turbines

Radial turbines have been used for over 180 years and it was first conceived to produce hydraulic power. There are basically two types of radial turbine: radial-outflow and radial inflow. The first successful hydraulic radial turbine for commercial use is developed by a French engineer (1830), Fourneyron, which is radial-outflow type. Later the first radial-inflow hydraulic turbine that gave excellent results and was highly regarded was built by Francis and Boyden in United States (1847)<sup>[1]</sup>. This type of machine is now known as the Francis turbine, a simplified arrangement of it being shown in Figure 1.1.

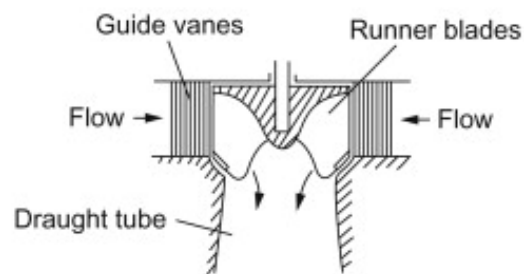


Figure 1.1 Schematic of Francis Turbine

In the figure, it can be observed that the flow comes from radial direction and exit in the axial direction.

Single stage radial-outflow turbine has several disadvantages, one of which is low specific work. However, Kearton (1951) and Shepherd (1956) pointed that multi-stage radial-outflow steam turbine could be in practical use due to the tremendous increase in the specific volume. Ljungström<sup>[2]</sup> steam turbine, as an exemplar shown in Figure 1.2, is unique because it has multiple stages yet without any stationary stage. Each of the stages of the two rows of blades rotates in opposite direction so that they can both be regarded as rotors.

Between the two directions radial turbines, the inward-flow radial (IFR) turbine covers wider ranges of power, rates of mass flow, and rotational speeds, from very large Francis turbines used in hydroelectric power generation and developing hundreds of megawatts down to tiny closed cycle gas turbines for space power generation of a few kilowatts<sup>[3]</sup>. For the goals, scope and area in this thesis, the research is solely focused on the inward-flow turbine.

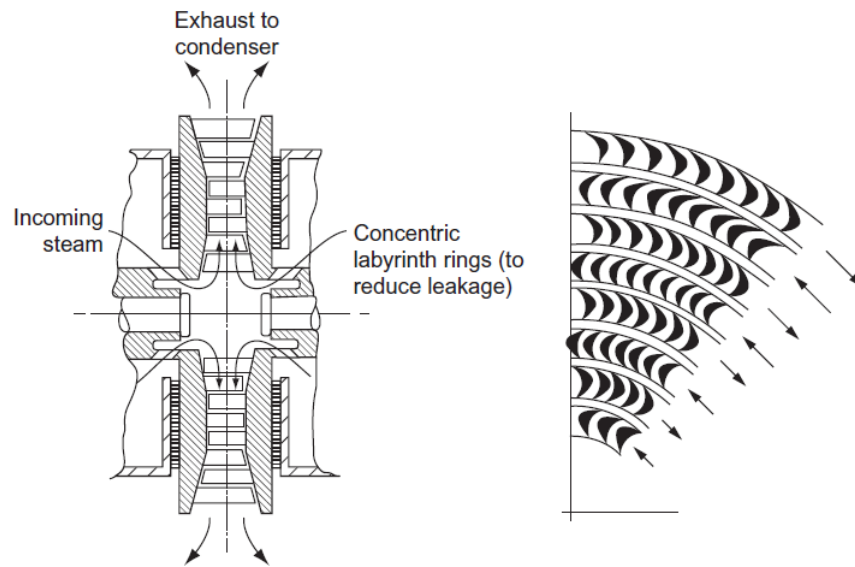


Figure 1.2 Sketch of Ljungström Steam Turbine

## 1.2. Application Area

Besides IFR hydraulic turbines, the IFR gas turbines, as well, have been applied extensively for powering automotive turbocharges, aircraft auxiliary power units, expansion units in gas liquefaction, and other cryogenic systems and as a component of the small (10 kW) gas turbines used for space power generation (Anon, 1971). In addition, it is considered for primary power use in automobiles and in helicopters. With advanced technology, a cooled IFR turbine could offer significant improvement in efficiency and performance, according to the study of Huntsman, Hodson, and Hill (1992), at Rolls-Royce<sup>[4, 5]</sup>.

Compared to axial-flow turbines over a limited range of specific speed, IFR turbines provide about the same efficiency and produce greater work obtained per stage. Other remarkable advantages offered by IFR turbine are its ease of manufacture and superior ruggedness. When the mass flow and power application are relatively low yet with a high pressure drop, the inward-flow radial turbine is preferred rather than an axial turbine <sup>[2, 6]</sup>.

### **1.3. Types of IFR turbines**

In an IFR turbine, the energy is transferred from the fluid to the rotor by passing from a large radius to a smaller radius. However, there are two sub-classifications of IFR turbine: Cantilever turbine and 90° IRF turbine <sup>[2]</sup>.

Figure 1.3(a) shows a cantilever turbine where the blades are limited to the region of the rotor tip, extending from the rotor in the axial direction. In practice the cantilever blades are usually of the impulse type (i.e., low reaction), by which it is implied that there is little change in relative velocity at inlet and outlet of the rotor. There is no fundamental reason why the blading should not be of the reaction type. However, the resulting expansion through the rotor would, require an increase in flow area. This extra flow area is extremely difficult to accommodate in a small radial distance, especially as the radius decreases through the rotor row.



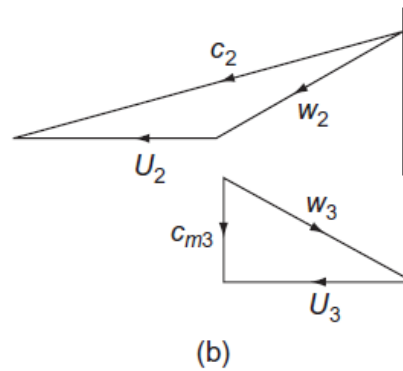
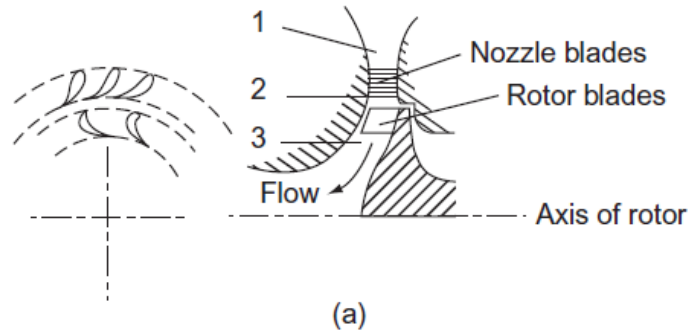


Figure 1.3 (a) Sketch of a cantilever turbine (b) Velocity Triangles at rotor inlet and outlet of a cantilever turbine

Aerodynamically, the cantilever turbine is similar to an axial-impulse turbine and can even be designed by similar methods. Figure 1.3(b) shows the velocity triangles at rotor inlet and outlet. The fact that the flow is radially inwards hardly alters the design procedure because the blade radius ratio  $r_2/r_3$  is close to unity anyway.

Figure 1.4 shows a typical layout of a  $90^\circ$  IFR turbine; the inlet blade angle is generally made zero, a fact dictated by the material strength and often high gas temperature. From station 2, the rotor vanes extend radially inward and turn the flow into the axial direction. The exit part of the vanes, called the exducer, is curved to remove most if not all of the absolute tangential component of velocity. The  $90^\circ$  IFR turbine or centripetal turbine is very similar in

appearance to the centrifugal compressor, but with the flow direction and blade motion reversed.

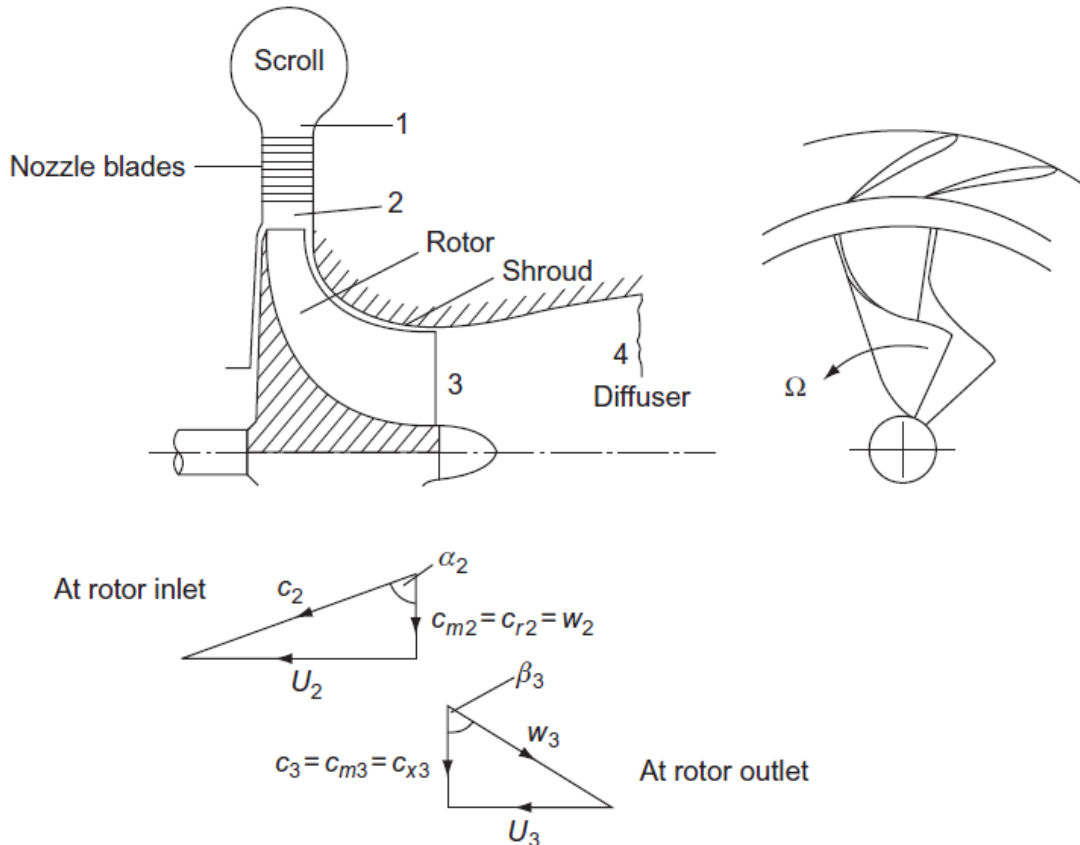


Figure 1.4 Layout of a 90° IFR turbine

The fluid discharging from turbine rotor may have a considerable velocity  $c_3$ , then an axial diffuser would normally be incorporated to recover most of the kinetic energy  $\frac{1}{2}c_3^2$ . In hydraulic turbines a diffuser is used as well and is called the draught tube.

In the velocity triangles in Figure 1.4, the relative velocity  $w_2$  is radially inward (zero incidence), and the absolute velocity at the exit  $c_3$  is axial. This configuration of velocity triangle is called the nominal design condition.

Due to higher structural strength and efficiency, 90° IFR turbines are usually preferred over cantilever IFR turbines. Therefore, this thesis specifically studies the 90° IFR turbines, and all the inward-flow radial turbines mentioned later indicate the 90° IFR turbines.

#### 1.4. Performance characteristic of IFR turbines

##### 1.4.1. Turbine characteristics

In this section, groups of variables developed by means of dimensional analysis. These dimensionless groups are able to represent some characteristics of the machine based on pressure drops and mass flow. What's more important, they help reduce the laboratory testing efforts by deducting a number of variables. Specially and generally, developing dimensionless groups of variables have the following benefits:

1. Prediction of a prototype performance from tests conducted on a scaled model (similitude)
2. A unique representation of the performance (Mach number, Reynolds number, etc.).
3. Determination of a best machine on the basis of efficiency for a specific head, speed, and flow rate.

The performance parameters  $\Delta h_{0s}$ ,  $\eta$  and  $P$  for a turbine are a function of many variables, which can be expressed as <sup>[2, 7, 8]</sup>:

$$\Delta h_{0s}, \eta, P = f(\mu, N, D, \dot{m}, \rho_{01}, a_{01}, \gamma) \quad (1-1)$$

Selecting  $\rho_{01}$ ,  $N$  and  $D$  reduces the variables in Equation 1-1 into five dimensionless groups as:

$$\frac{\Delta h_{0s}}{N^2 D^2}, \eta, \frac{P}{\rho_{01} N^3 D^5} = f\left\{\frac{\dot{m}}{\rho_{01} N D^3}, \frac{\rho_{01} N D^2}{\mu}, \frac{ND}{a_{01}}, \gamma\right\} \quad (1-2)$$

In Equation 1-2, the flow coefficient  $\phi = \dot{m}/(\rho_{01} N D^3)$  can be transformed into

$\phi = \dot{m}/(\rho_{01}a_{01}D^2)$ . As  $ND$  is proportional to blade speed, the group  $ND/a_{01}$  is regarded as a *blade Mach number*.

For the isentropic compression or expansion of ideal gas, the relations among the enthalpy change, pressures and temperatures are:

$$\frac{T_{02s}}{T_{01}} = \left(\frac{p_{02}}{p_{01}}\right)^{(\gamma-1)/\gamma} \quad (1-3)$$

$$\Delta h_{0s} = C_p T_{01} \left[ \left(\frac{p_{02}}{p_{01}}\right)^{(\gamma-1)/\gamma} - 1 \right] \quad (1-4)$$

Because  $C_p = \gamma R/(\gamma - 1)$  and  $a_{01} = \sqrt{\gamma RT_{01}}$ ,

$$\frac{\Delta h_{0s}}{a_{01}^2} \propto f\left(\frac{p_{02}}{p_{01}}\right) \quad (1-5)$$

Now flow coefficient can be expressed as:

$$\frac{\dot{m}}{\rho_{01}a_{01}D^2} = \frac{\dot{m}RT_{01}}{p_{01}\sqrt{\gamma RT_{01}}D^2} = \frac{\dot{m}\sqrt{RT_{01}}}{D^2 p_{01}\sqrt{\gamma}} \quad (1-6)$$

As  $\dot{m} \equiv \rho_{01}D^2(ND)$ , the power coefficient can be rewritten as:

$$\hat{P} = \frac{P}{\rho_{01}N^3D^5} = \frac{\dot{m}C_p\Delta T_0}{\{\rho_{01}D^2(ND)\}(ND)^2} = \frac{C_p\Delta T_0}{(ND)^2} \equiv \frac{\Delta T_0}{T_{01}} \quad (1-7)$$

According to all the above dimensionless groups, Equation 1-2 now is:

$$\frac{p_{02}}{p_{01}}, \eta, \frac{\Delta T_0}{T_{01}} = f\left\{\frac{\dot{m}\sqrt{RT_{01}}}{D^2 p_{01}}, \frac{ND}{\sqrt{RT_{01}}}, Re, \gamma\right\} \quad (1-8)$$

In Equation 1-8, the term  $(\dot{m}\sqrt{RT_{01}})/(D^2 p_{01})$  is usually referred as the *flow capacity*.

For a turbine of specific size that work with a single gas, in industry  $\gamma$ ,  $R$  and  $D$  are customarily eliminated. In addition, if the machine runs at high Reynolds numbers (or over a small speed range,  $Re$  can be neglected too. Then, Equation 1-8 becomes:

$$\frac{p_{02}}{p_{01}}, \eta, \frac{\Delta T_0}{T_{01}} = f\left\{\frac{\dot{m}\sqrt{T_{01}}}{P_{01}}, \frac{N}{\sqrt{T_{01}}}\right\} \quad (1-9)$$

However, eliminating diameter  $D$  and gas constant  $R$  makes the variable groups no longer non-dimensional. The two terms in Equation 1-9 are defined as *corrected flow* and *corrected speed*.

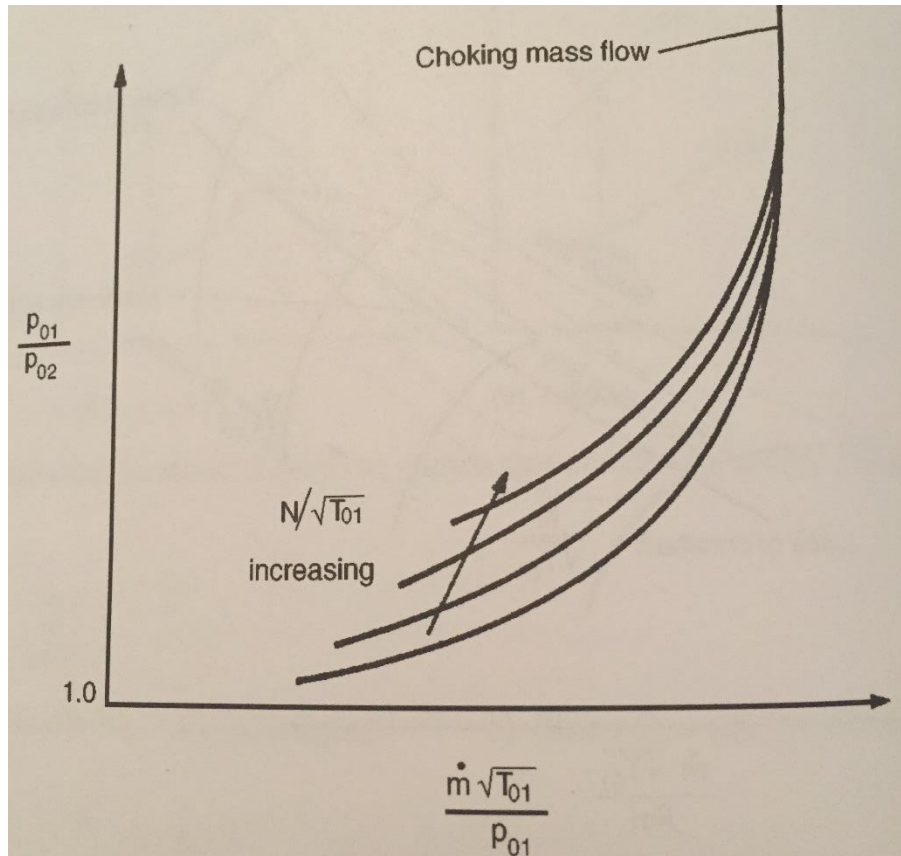


Figure 1.5 Diagram of typical high-speed turbine characteristic <sup>[2]</sup>

With the above dimensionless groups, multiple performance and characteristics are able to be conveniently presented in one chart. Figure 1.5 shows a typical high-speed turbine characteristic. Turbines are able to operate with a high-pressure ratio across each stage because the boundary layers on the surfaces of the turbine blades are accelerating and therefore stable. The high-pressure ratios soon lead to choking in the turbine stator blades and therefore a fixed non-dimensional mass flow through the machine. Once the turbine stators are fully choked, the operating point is independent of  $N/\sqrt{T_{01}}$  because the rotation of the

blades has virtually no influence on either the turbine pressure ratio or the non-dimensional mass flow rate.

The turbomachine designer is often faced with the basic problem of deciding what type of machine will be the best choice for a given duty. At the outset of the design process, some overall requirements of the machine will usually be known. For a hydraulic pump, these would include the head required,  $H$ , the volume flow rate,  $Q$ , and the rotational speed,  $N$ . In contrast, if a high-speed gas turbine was being considered, the initial specification would probably cover the mass flow rate,  $m$ , the specific work,  $\Delta h_0$ , the specific work,  $\Delta h_0$ , and the preferred rotational speed,  $N$ .

Two non-dimensional parameters called the specific speed (Balje),  $N_s$ , and specific diameter,  $D_s$ , are often used to decide upon the choice of the most appropriate machine with some empirical charts such as Figure 1.6 and Figure 1.7. The specific speed is derived from the non-dimensional groups defined in Equation 1-10 that the characteristic diameter  $D$  of the turbomachine is eliminated. The value of  $N_s$  gives the designer a guide to the type of machine that will provide the normal requirement of high efficiency at the design condition. Similarly, the specific diameter is derived from these groups by eliminating the speed <sup>[7-10]</sup>,  $N$  as in Equation 1-11.

$$N_s = \frac{NQ_{exit}^{1/2}}{\Delta h_{ideal}^{3/4}} \quad (1-10)$$

$$D_s = \frac{D\Delta h_{ideal}^{1/4}}{Q_{exit}^{1/2}} \quad (1-11)$$

Figure 1.6 is a graph that shows the relation between specific speed and overall efficiency. Figure 1.7 is the chart relating specific speed, specific diameter and efficiency. Then,

with known parameters such as flow rate and specific work, specific work can be decided by choosing the optimum efficiency from Figure 1.6. Furthermore, with Figure 1.7 from Balje specific diameter can be determined.

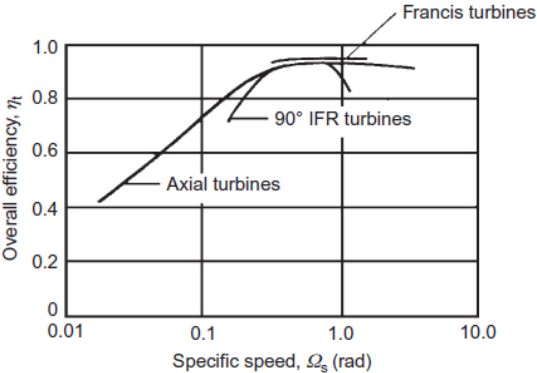


Figure 1.6 Diagram Between efficiency vs Specific Speed for different Turbine [2]

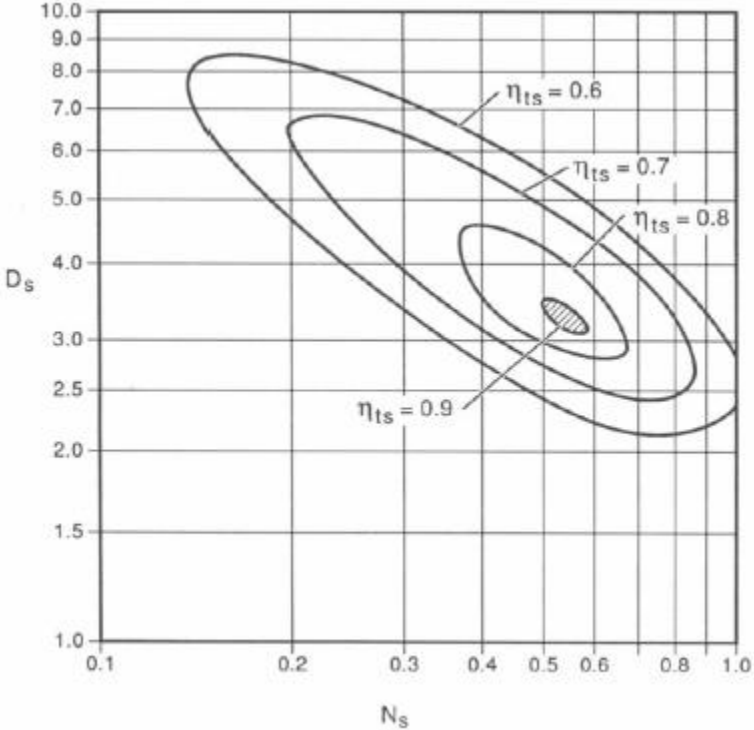


Figure 1.7 Balje Diagram

### 1.4.2. Thermodynamics of the IFR turbines

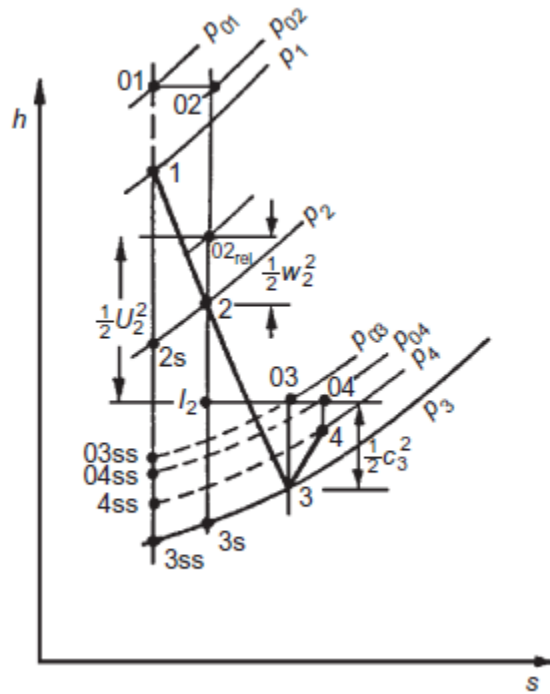


Figure 1.8 h-s Diagram in an inward-flow radial turbine

Figure 1.8 demonstrates the thermodynamic processes for the fluid working through the radial turbine <sup>[11-13]</sup>: (a) the scroll and nozzle blade row, (b) a radial rotor, (c) a diffuser. The whole processes are assumed to be adiabatic, yet irreversible, which means the entropy increases in each process.

Across the scroll and nozzle blade (1-2), the stagnation enthalpy is assumed to be constant,  $h_{01} = h_{02}$ . Then

$$h_1 - h_2 = \frac{1}{2}(c_2^2 - c_1^2) \quad (1-12)$$

Reference point 2 is at the inlet radius  $R_2$ , therefore the annular space between nozzle exit and blade inlet is counted in the process 1-2. Hence any friction loss occurring in this space is lumped with the irreversibility in the nozzle.



For an adiabatic irreversible process in a rotating component, a parameter rothalpy

$I = h_{0rel} - \frac{1}{2}U^2$  is introduced, which should be constant. So the process in the rotor 2-3:

$$h_{02rel} - \frac{1}{2}U_2^2 = h_{03rel} - \frac{1}{2}U_3^2 \quad (1-13)$$

In Equation 1-13,  $h_{0rel} = h + \frac{1}{2}w^2$  gives:

$$h_2 - h_3 = \frac{1}{2}[(U_2^2 - U_3^2) - (w_2^2 - w_3^2)] \quad (1-14)$$

The stagnation enthalpy in the diffuser 3-4 doesn't change, therefore:

$$h_4 - h_3 = \frac{1}{2}(c_3^2 - c_4^2) \quad (1-15)$$

The specific work done in the rotor is:

$$\Delta W = h_{01} - h_{03} = U_2 c_{\theta 2} - U_3 c_{\theta 3} \quad (1-16)$$

For  $h_{01} = h_{02}$ :

$$\Delta W = h_{02} - h_{03} = h_2 - h_3 + \frac{1}{2}(c_2^2 - c_3^2) = \frac{1}{2}[(U_2^2 - U_3^2) - (w_2^2 - w_3^2) + (c_2^2 - c_3^2)] \quad (1-17)$$

Each term in Equation 1-17 makes a contribution to the specific work done on the rotor.

Because of the relatively large difference between  $r_3$  and  $r_2$  leading to huge difference between

$U_3$  and  $U_2$ , the first term  $\frac{1}{2}(U_2^2 - U_3^2)$ , makes a significant contribution to the total specific

work. For the axial-flow turbine, where  $U_3 = U_2$ , of course, no contribution to the specific work is

obtained from this term. Therefore, that is one of the reasons why inward-flow radial turbine

can produce more work per stage than an axial turbine at the same inlet condition. Also, this is

the main advantages of inward-flow over outward flow, because the same term would do

negative contribution in an outward-flow radial turbine. For the second term in Equation 1-17,

a positive contribution to the specific work is obtained when  $w_3 > w_2$ . In fact, accelerating the relative velocity through the rotor is a most useful aim of the designer as this is conducive to achieving a low loss flow. The third term in Equation 1-17 indicates that the absolute velocity at rotor inlet should be larger than at rotor outlet so as to increase the work input to the rotor.

Having known the inlet and outlet condition, the efficiency can be calculated. However, two kinds of efficiencies can be used to evaluate the turbine: Total to static efficiency and total to total efficiency.

The definition of total to static (enthalpy) efficiency is presented in Equation 1-18

$$\eta_{ts} = \frac{\text{Shaft power output of an actual turbine}}{(\text{Shaft power output} + \text{Power wasted in exhaust kinetic energy}) \text{ of an ideal turbine}} \quad (1-18)$$

Assuming for ideal gas  $\Delta h = C_p \Delta T$  and  $C_p$  is constant yields:

$$\begin{aligned} \eta_{ts} &= \frac{c_p(T_{01} - T_{03})}{C_p(T_{01} - T_{03ss}) + C_p(T_{03ss} - T_{3ss})} \\ &= \frac{T_{01} - T_{03}}{T_{01} - T_{3ss}} \end{aligned} \quad (1-19)$$

With the same assumptions in Equation 1-19, Total to total (enthalpy) is defined as Equation 1-20, and sometime is referred as isentropic efficiency:

$$\begin{aligned} \eta_t &= \frac{\text{Actual work output}}{\text{Ideal work output}} = \frac{T_{01} - T_{03}}{T_{01} - T_{03ss}} \\ &= \frac{1 - T_{03}/T_{01}}{1 - (P_{03}/P_{01})^{(\gamma-1)/\gamma}} \\ &= \frac{T_{01} - T_{03}}{T_{01}(1 - \pi^{(\gamma-1)/\gamma})} \end{aligned} \quad (1-20)$$

The difference between the sorts of efficiencies is that the total to total only consider the loss in the nozzle and rotor, while the total to static efficiency counts the kinetic energy in the exhaust as part of total loss<sup>[14-16]</sup>.

When examining a single stage (except the last one) in a multi-stage rotor, the exit kinetic energy is not lost, because it will move to the next stage. Nevertheless, total to static efficiency is normally used because most inward-flow radial turbines have only one stage.

## 1.5. Radial turbine design

The design process usually contains two processes: design and analysis. After designing the geometry of the turbine, it is necessary to analysis performance of the designed turbine such as efficiency and off-design performance in order to verify the design.

The design process usually follows three steps: Preliminary one-dimensional optimization, Quasi-3D design and full 3D analysis

### 1.5.1. Preliminary 1-D optimization

The components to be preliminarily designed in 1-D are shown in Figure 1.9. Basically, the design procedure is focused on the inlet volute, nozzle row, rotor and exhaust diffuser. The vaneless annular passages before and after the nozzle row are automatically inserted because they are insignificant. The design requires specific aerodynamic and geometric calculations at locations of all the inlet and exit of all components. The positions are designated with numbers from 1 to 6 shown as in Figure 1.10 <sup>[7. 17]</sup>.

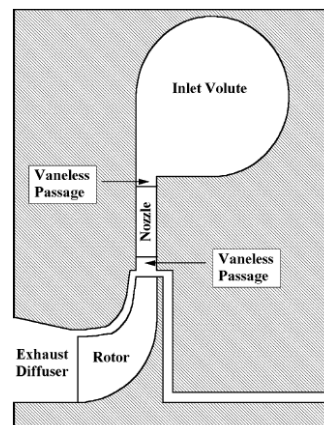


Figure 1.9 Main Components of an inward-flow Radial Turbine

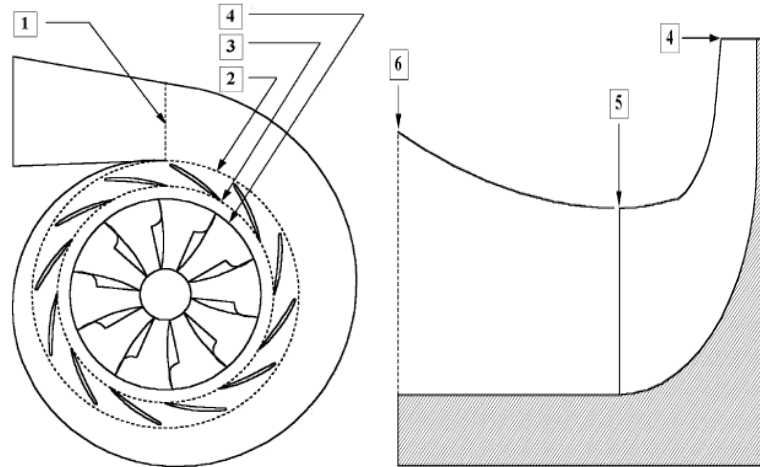


Figure 1.10 Position numbers designated to radial turbine components

The stage performance is conveniently specified as total-to-static performance referenced to the rotor exit (station 5). The stage total-to-total performance and the influence of an exhaust diffuser can be forecast as part of the preliminary design to guide the designer in adjusting the performance specifications if appropriate. Hence, the basic stage design specifications to be supplied by the designer are

- Stage inlet total temperature,  $T_{t1}$ .
- Stage inlet total pressure,  $P_{t1}$ .
- Stage mass flow rate.
- Total-to-static pressure ratio,  $P_{t1}/P_5$ .
- Specific speed,  $N_s$ .
- Total-to-static efficiency,  $\eta_{ts}$ .
- Total-to-static velocity ratio,  $v_5$ .
- Equation of state for the working fluid.

The specific speed defined in dimensionless form as Equation 1-10 now becomes:

$$N_s = \frac{\omega Q_5^{1/2}}{\Delta h_{ideal}^{3/4}} \quad (1-21)$$

In the equation,  $Q_5 = \dot{m}/\rho_5$ .

Most of the basic stage design specifications mentioned above are easily available from the proposed application, except  $n_s$ ,  $v_s$  and  $\eta_s$ . However, the choices for  $n_s$ ,  $v_s$  and  $\eta_s$  really determine the quality of the design. The selection of these three parameters is usually based on empirically generalized performance correlations. Many researchers, e.g, Wood, Linhardt, Rohlik and Balje, have made contributions to establish the generalized correlations of radial-inflow turbine performance.

These typically provide estimates of the expected efficiency and recommended values of velocity ratio as a function of specific speed. Those correlations are based on various definitions of specific speed and differ with regard to whether total-to-total or total-to-static performance is estimated.

Figure 1.11 shows a generalized stage performance chart used for the present preliminary design system. This chart provides estimates of the expected efficiency and recommended values of velocity ratio as a function of specific speed.

Figure 1.11 can initially predict the optimum efficiency and the corresponding speed. As a general rule, the preferred range of values for specific speed is 0.45 to 0.75. However, the specific speed is not really an arbitrary parameter, since size, speed, Mach number levels, mechanical integrity, etc. may impose definite constraints that preclude choices in the preferred range.

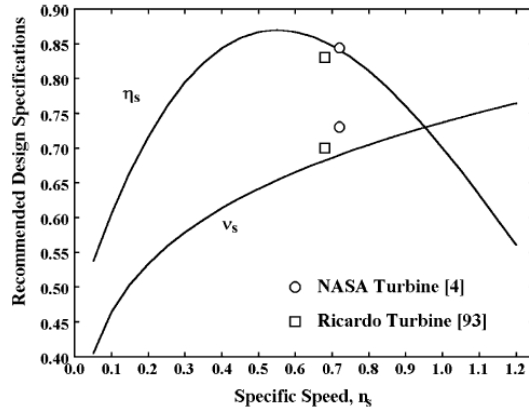


Figure 1.11 Generalized stage performance chart for design

The best approach is for the preliminary design system to display Figure 1.12 on demand to guide the designer in selecting the design specifications. It is also useful to provide the option to use these correlations to define default values of  $\eta_s$  and  $v_s$  as a function of the specified specific speed so that the designer can either use them directly or supply alternate values. Both of these features are easily incorporated using the following analytical equations, which correspond to the curves shown in Figure 1.12 [4].

$$v_s = 0.737N_s^{0.2} \quad (1-22)$$

$$\eta_s = 0.87 - 1.07(N_s - 0.55)^2 - 0.5(N_s - 0.55)^3 \quad (1-23)$$

Once a preliminary design has been accomplished, the performance analysis can be used to improve the estimate for  $\eta_s$ .

The preliminary design of the complete stage requires many additional specifications to select well-matched and optimized stage components. If the designer must specify all of these component design parameters to obtain a design, the preliminary design system will be rather ineffective. A better approach used is to supply default values for all component design specifications such that the preliminary design system can generate a candidate stage design from the basic stage design specifications. The designer can optimize the design by adjusting

any of the default specifications for the components. It is always more efficient to optimize component specifications from a reasonable set of existing values than to select a complete set of specifications. Much of the design optimization process can be accomplished within the preliminary design system.

### 1.5.2. Quasi-3D design

The nozzle-blade preliminary aerodynamic design procedure described in the previous section is easily modified to provide a sound basis for the detailed aerodynamic design also. That approach is almost always sufficient to achieve design objectives for both aerodynamic performance and mechanical integrity. However, 1-D preliminary design and analysis ignore the details of geometry, so the given specifications are not sufficient to ensure that the components will perform as predicted. Therefore, detailed quasi-3D design and analysis for the gaspath are required.

Quasi-3D employs two 2-D flow analyses to approximate the three dimensional flow. These two 2-D surfaces are hub-to-shroud and blade-to-blade geometries, shown as Figure 1.12 and Figure 1.13 respectively.

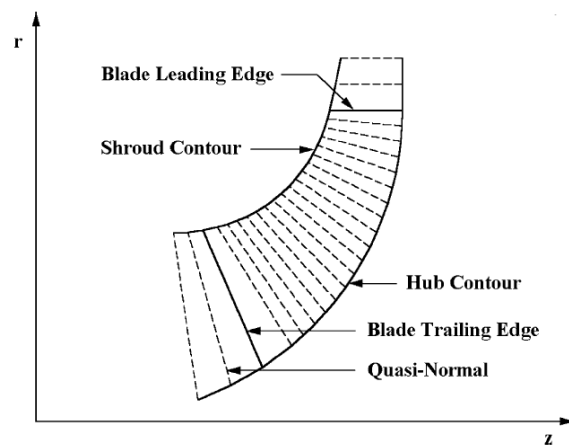


Figure 1.12 Hub-to-shroud sketch of a rotor blade

Hub-to-shroud geometry defines the blade by distributions of the polar angle,  $\theta$  (or blade angle,  $\beta$ ) and the blade thickness,  $t_b$ , along the camberline. Three types of blade geometry are considered to design. <sup>[18-23]</sup>

- Two-dimensional, axial element blades:  $\theta_c = \theta_c(r)$ ,  $t_b = t_b(r)$
- Two-dimensional, radial element blades:  $\theta_c = \theta_c(z)$ ,  $t_b = t_b(z)$
- Three-dimensional straight-line blades:  $\theta_c = \theta_c(\xi)$ ,  $t_b = t_b(\xi)$ ,  $\xi = (m - m_2)/(m_1 - m_2)$ .

$\xi$  is the dimensionless meridional distance along the contours from the trailing edge to the leading edge. Then, the blades are constructed by connecting the blade surfaces on the two end-wall contours with straight-line elements.

Axial element blades are suitable for nozzle blade design, while impellers often apply radial element blades to eliminate centrifugal blade bending stresses. As to straight-line element blades generally offer superior impeller aerodynamic performance potential when acceptable mechanical integrity can be achieved. However, the ways of constructing the geometry will not be introduced in this section.

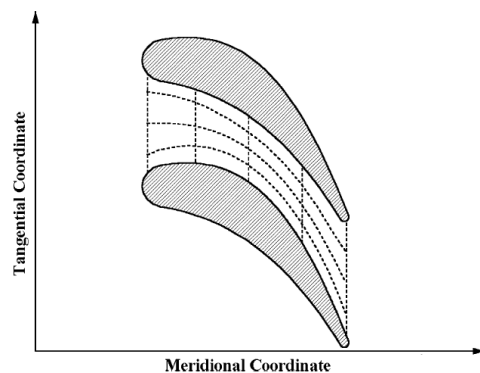


Figure 1.13 Blade-to-blade sketch of a rotor

Figure 1.13 is the blade-to-blade geometry. Prediction of the flow through cascades of blades is fundamental to all aspects of turbomachinery aerodynamic design and analysis. The



flow through the annular cascades of blades in any turbomachine is really a three-dimensional flow problem. But the simpler two-dimensional blade-to-blade flow problem offers many advantages. It provides a natural view of cascade fluid dynamics to help designers develop an understanding of the basic flow processes involved. Indeed, very simple two-dimensional cascade flow models were used in this educational role long before computational methods and computers had evolved enough to produce useful design results.

Today, blade-to-blade flow analysis is a practical design and analysis tool that provides useful approximations to many problems of interest. Inviscid blade-to-blade flow analysis addresses the general problem of two-dimensional flow on a stream surface in an annular cascade. Two-dimensional boundary layer analysis can be included to provide an approximate evaluation of viscous effects. Blade-to-blade flow analysis provides a practical method to calculate blade-loading diagrams. Indeed, blade-to-blade flow analysis is an essential part of a modern aerodynamic design system. Nonetheless, that approach ignores the secondary flows that develop due to the migration of low momentum boundary layer fluid across the stream surfaces. Its accuracy becomes highly questionable when significant flow separation is present. These limitations require particular care when analyzing the diffusing flow in compressor cascades. They are less significant for analysis of the accelerating flow in turbine cascades, but designers still must recognize the approximations and limitations involved.

### **1.5.3. Full 3D design**

The quasi-3D analyses have limited conditions and accuracy. Therefore, 3D analysis is required for more precise aerodynamics and structural analyses. 3-D analysis must involve CFD

technique. Apart from coding to conduct CFD calculation, there are several commercial software such as FLUENT and CFX available.

### 1.6. Scope, goals and organization of the thesis

The goals of the thesis mainly are two aspects: Design and analysis of inward-flow radial gas turbine and inward-flow radial hydraulic turbine.

The design of the gas turbine is based on the project of solar-biogas hybrid energy system, and the scheme of which is shown as Figure 1.14.

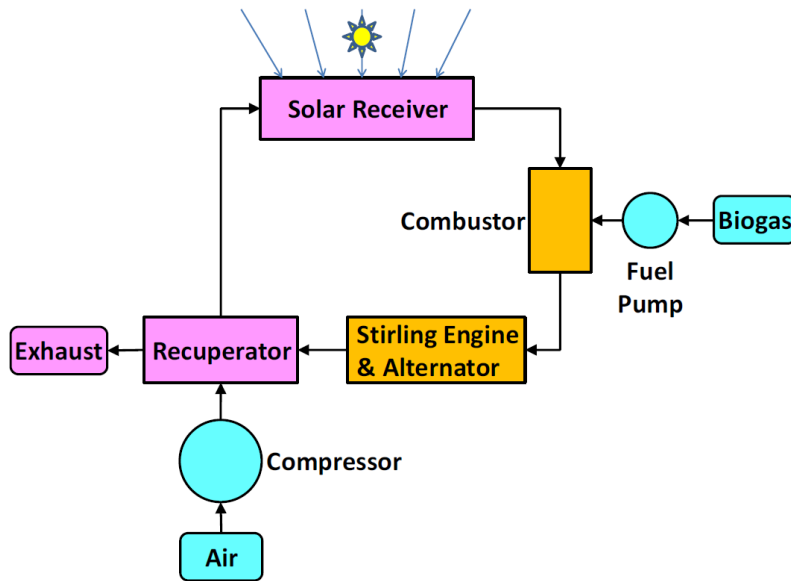


Figure 1.14 The schematic of the solar-biogas hybrid energy system

The working fluid air first comes into the compressor. The compressed air gets initially warmed in the recuperator by the exhaust from the exit of the engine. Then, the air is heated second time in the solar receiver. At last, the gas is finally heated in the combustion with biogas. After three steps of heating, the air becomes hot and pressurized gas and flows into an inward-flow radial turbine. Hence, the turbine is able to produce work. Finally before the gas exhausts

to the ambient, it preheats the air coming into the recuperator. The main goal of the thesis is to design an inward-flow radial turbine that fits in the system.

The narrow scope focuses on the design of the turbine, while it expands to wide scope when the whole system is being studied. However, the organization of the thesis comes from wide to narrow scope.

The first step of the thesis analyzes the thermodynamics of the system. With the application purpose and components that have been bought previously, the specifications for the turbine can be obtained. With the specifications, the turbine can be designed.

Then the thesis will analyze the performance of the turbine. Not only does the turbine is analyzed alone, it is also analyzed with its application in the system, both theoretically and experimentally.

Finally, the thesis is to design a turbine that fits in the solar-biogas hybrid energy system, so as to verify the concept of the system and validate its practical use.

The second goal of the thesis is to study the radial hydraulic turbine, based on previous experiment data of Prof. Engeda. Specifically, the thesis will study the centrifugal pump running as turbine. A more accurate approach to predict the performance of pump running in turbine mode from the known characteristics in the pump mode is expected to be obtained by analyzing the testing data.

## CHAPTER 2. COMPONENT OF RADIAL TURBINE

As shown in Figure 1.9, the inward-flow radial turbine mainly consists of the volute, nozzle, rotor and the diffuser. In addition, from volute to nozzle and from nozzle to rotor, there are two blocks of annular vaneless space lying between them. In this chapter, some more details of each component are introduced.

### 2.1. The Volute

Figure 2.1 illustrates the geometry of a typical inlet volute. The passage area and mean radius are specified at station 1, where the flow is inside the volute, but has not yet started to exit the volute. These parameters are also specified at station 2, where half of the flow has exited from the volute passage. Station 3 is the annular passage at the volute exit, where the radius and the hub-to-shroud passage width,  $b_3$ , are specified. The exit area is given by <sup>[4, 18]</sup>:

$$A_3 = 2\pi r_3 b_3 \quad (1-1)$$

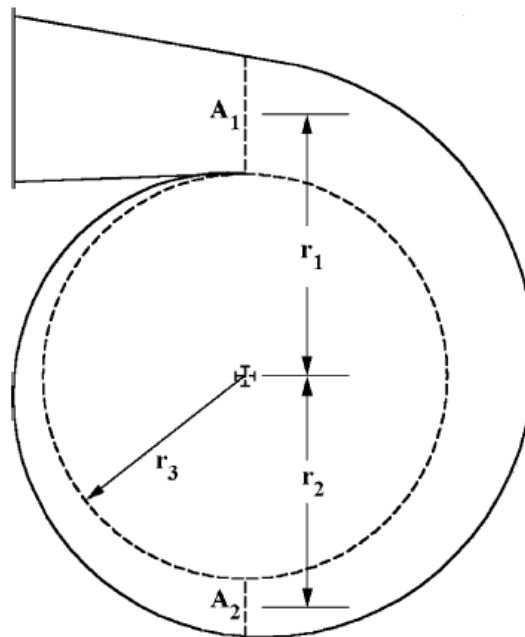


Figure 2.1 The sketch of the volute geometry

This is the first component in the stage, so the inlet total thermodynamic conditions are also specified, or known from a preceding stage analysis. All flow conditions at station 1 are computed by performing a mass balance using the stage inlet mass flow. The same process, assuming no losses and using half of the inlet mass flow, supplies the flow conditions at station 2. The effective, one-dimensional angular momentum at the volute exit is estimated from conservation of angular momentum based on the flow data at station 2 <sup>[4, 19]</sup>.

$$C_{\theta 3} = r_2 C_2 / r_3 \quad (2-2)$$

A mass balance using the inlet mass flow and tangential velocity component obtained from Equation 2-2 yields the other flow conditions at station 3. However, the losses and the corresponding total thermodynamic conditions at station 3 must also be determined, so an iterative process is required. The total pressure losses considered include the profile loss and a circumferential distortion loss. The profile loss is calculated with the simple boundary layer analysis. The circumferential distortion loss coefficient accounts for mixing losses associated with circumferentially non-uniform angular momentum imposed at the volute exit <sup>[4, 20]</sup>. It is given by:

$$Y_{\theta} = \left[ \left( \frac{r_1 C_1}{r_3} - C_{\theta 3} \right) / C_3 \right]^2 \quad (2-3)$$

If the volute is designed to maintain uniform angular moment in the circumferential direction, this loss will be identically equal to zero. By contrast, a constant area plenum will yield a value of  $C_2$  approximately equal to half of  $C_1$ . From Equation 2-2 and 2-3 it is easily seen that the circumferential distortion loss will be significant for that case. The volute exit total pressure is given by

$$Y = Y_p + Y_{\theta} = (P_{t1} - P_{t3}) / (P_{t3} - P_3) \quad (2-4)$$

$$P_{t3} = (P_{t1} + Y P_3)/(1 + Y) \quad (2-5)$$

$Y_p$  is the profile loss due to the two boundary layers on the opposite walls of the effective flow passage.

For this stationary component, the total enthalpy is constant throughout the volute. Hence,

$$H_3 = H_1 \quad (2-6).$$

Assuming the flow is inviscid, the mass flow is:

$$\dot{m} = A_3 \rho_3 C_{m3} \quad (2-7)$$

However, if the end-wall boundary layer blockage is considered, Equation 2-7 should be adjusted as:

$$\dot{m} = (1 - \Delta) A_3 \rho_3 C_{m3} \quad (2-8)$$

$\Delta$  is the normalized defect boundary layer:

$$\Delta = \sum \delta^* / b \quad (2-9),$$

where  $\delta^*$  is the boundary layer, and  $b$  is the passage width. Then, the discharge exit static enthalpy should be <sup>[4, 21]</sup>:

$$h_3 = H_3 - \frac{1}{2} (C_{m3}^2 + C_{\theta 3}^2) \quad (2-10)$$

## 2.2. Inlet Nozzle

The nozzle row in radial-inflow turbines is usually a simple radial passage of constant width. But that is not a necessary restriction, so a more general specification of the nozzle geometry is used. The geometry is specified at the inlet, mid-passage and exit stations, which are designated by subscripts 1 through 3, respectively. At each of these stations, the axial coordinate,  $z$ , radius,  $r$ , passage width,  $b$ , blade camberline angle,  $\theta$ , and blade thickness,  $t_b$ , are

specified. In addition, the number of blades,  $n$ , the throat blade-to-blade width,  $o$ , and passage width at the throat,  $b_{th}$ , are supplied. Figure 2.2 illustrates some of the key geometrical parameters supplied<sup>[4, 20]</sup>.

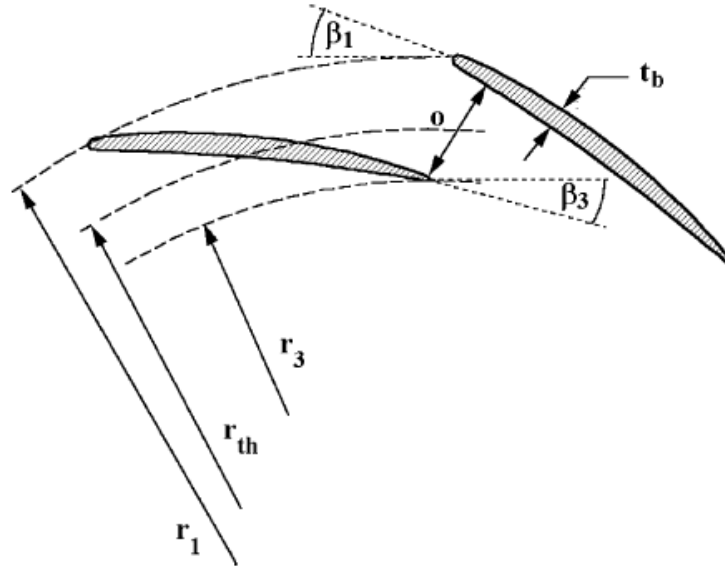


Figure 2.2 Sketch of nozzle geometry

The nozzle exit flow may be either subsonic or supersonic, depending on the stage discharge pressure. For a conventional inward-flow radial turbine, the flow should be subsonic. When  $M_3 = 1$ , the nozzle is choked. Hence, a subsonic solution is always required and will be considered first. The subsonic discharge flow angle is estimated by

$$\sin\alpha_{os} = b_{th}o/(s_3b_3) \quad (2-11),$$

where  $s = 2\pi r/n$ .

The discharge flow angle is estimated by:

$$\tan\alpha_3 = (r_3/r_{th})\tan\alpha_{os} \quad (2-12)$$

Similar to the volute, the nozzle exit total pressure could be obtained by:

$$Y = Y_p + Y_{inc} = (P_{t1} - P_{t3})/(P_{t3} - P_3) \quad (2-13)$$

$$P_{t3} = (P_{t1} + Y P_3)/(1 + Y) \quad (2-14)$$

Considering the boundary layer blockage, the mass flow is:

$$\dot{m} = (1 - \Delta) 2\pi r_3 b_3 \rho_3 C_3 \sin \alpha_3 \quad (2-15)$$

The enthalpy at the outlet of the nozzle is:

$$h_3 = h_{03} - \frac{1}{2} C_3^2 \quad (2-16)$$

In the design of the nozzle, the choked condition must be checked. The subscript is assigned to the parameters.

$$\dot{m}_* = N b_{th} o (1 - \Delta) \rho_* C_* \quad (2-17)$$

Then, the exit velocity  $C_3$  and angle are:

$$C_3 = \sqrt{2(H_3 - h_3)} \quad (2-18)$$

$$\sin \alpha_3 = \dot{m} / [(1 - \Delta) 2\pi r_3 b_3 \rho_3 C_3] \quad (2-19)$$

The largest possible  $C_{m3}$  is the one under choked condition, at the same time the  $P_3$  is the minimum static exit pressure.

$$C_{m3} = \dot{m} / [(1 - \Delta) 2\pi r_3 b_3 \rho_3] = a_3$$

### 2.3. The Turbine Rotor

The geometry of rotor is the most complicated one than all the other components in the inward-flow radial turbine. Typically, the flow is turned by  $90^\circ$  from radial to axial in the impeller.

Figure 2.3 and 2.4 show frontal and side views of the rotor to illustrate the geometry required <sup>[21, 40]</sup>. Similar to other components, the passage geometry is defined at the inlet, midpassage and exit stations numbered 1 through 3, respectively. These data are specifically referenced to a mean surface midway between the hub and shroud surfaces. Like the nozzle



row, the axial coordinate,  $z$ , radius,  $r$ , passage width,  $b$ , blade camberline angle,  $\beta$ , and blade thickness,  $tb$ , are specified at these stations. To properly address the passage curvature, the angle,  $\phi$ , formed by a tangent to the mean surface and the axial direction is also specified. This angle is illustrated for station 2 in Figure 2.4. This angle is measured in the flow direction. Hence in the case illustrated in Figure 2.4,  $\phi$  varies from  $-90^\circ$  at the inlet to  $0^\circ$  at the exit. In addition, the number of full blades,  $N$ , the throat blade-to-blade width,  $o$ , on the mean surface, the passage width at the throat,  $b_{th}$ , and the clearances,  $\delta c$  and  $\delta d$ , are supplied. One or more sets of splitter blades can also be specified, along with the fraction of the mean path length from the inlet occupied by the splitter blades. The analysis assumes splitter blades are identical to the full blades except for length and are equally spaced between the full blades.

There are several sources of internal losses in the impeller, including the passage curvature, blade clearance, incidence, blade loading and profile losses. It is also necessary to account for the energy consumed by the rotating disk in the housing. This disk friction loss is commonly referred to as a parasitic loss. It represents wasted energy rather than an aerodynamic loss in total pressure. In the case of condensing working fluids, the potential for moisture losses similar to those described for axial-flow turbines may also impact the rotor performance. Often partial-length splitter blades are used to provide additional work capability without reducing the choke capacity of the impeller.

The flow velocity  $C$ , and the relative velocity  $W$  are connected by:

$$\vec{C} = \vec{U} + \vec{W} \quad (2-20)$$

$U=Nr$  is the annular velocity of the rotor at a specific radius.

From the velocity triangle diagram, the following equations can be readily obtained:

$$W_m = C_m = \sqrt{C_z^2 + C_r^2} \quad (2-21)$$

$$W_\theta = C_\theta - \omega r \quad (2-22)$$

$$C = \sqrt{C_m^2 + C_\theta^2} \quad (2-23)$$

$$W = \sqrt{C_m^2 + W_\theta^2} \quad (2-24)$$

$$\tan\alpha = C_m/C_\theta \quad (2-25)$$

$$\tan\beta = C_m/W_\theta \quad (2-26)$$

Applying angular momentum equations gives the torque, the power and the specific work as:

$$\tau = \dot{m}(r_3 C_{\theta 3} - r_1 C_{\theta 1}) \quad (2-27)$$

$$\dot{w} = \omega\tau = \omega\dot{m}(r_3 C_{\theta 3} - r_1 C_{\theta 1}) \quad (2-28)$$

$$h_3 - h_1 = \omega(r_2 C_{\theta 2} - r_1 C_{\theta 1}) \quad (2-29)$$

As introduced in the previous chapter, the relative total enthalpy at station 3 can be gained by rothalpy  $I_3$  and  $U_3$ .

$$h_{0rel3} = I_3 + \frac{1}{2}U_3^2 \quad (2-30)$$

Consequently, there is the relative total pressure  $P_{0rel3}$  corresponding to  $h_{0rel3}$ .

The relation between actual relative total pressure  $P_{0rel3}$  and ideal relative velocity is shown in Equation 2-31.

$$P_{0rel3} = (P_{0rel3,id} + YP_3)/(1 + Y) \quad (2-31)$$

$Y$  is the loss coefficient:

$$Y = Y_p + Y_{inc} + Y_{BL} + Y_{HS} + Y_{CL} + Y_Q \quad (2-32)$$

It includes several kinds of losses such as profile losses ( $Y_p$ ), incidence loss ( $Y_{inc}$ ), blade loading loss ( $Y_{BL}$ ), hub-to-shroud loading effect ( $Y_{HS}$ ), clearance loss ( $Y_{CL}$ ) and total pressure loss ( $Y_Q$ ).

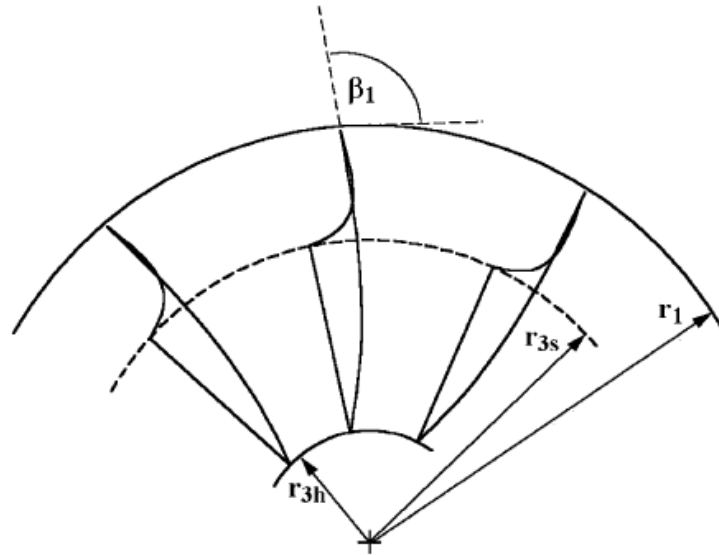


Figure 2.3 Front view of the rotor

Like the analysis for the nozzle, the mass flow rate considering the boundary layer blockage is calculated by:

$$\dot{m} = (1 - \Delta)2\pi r_3 b_3 \rho_3 W_3 \sin\beta_3 \quad (2-33)$$

For the choked condition:

$$\dot{m}_* = N b_{th} o (1 - \Delta) \rho_* W_* \quad (2-34)$$

$$C_3 = \sqrt{2(H_3 - h_3)} \quad (2-35)$$

The exit relative velocity and angle, when the flow is choked, are calculated as:

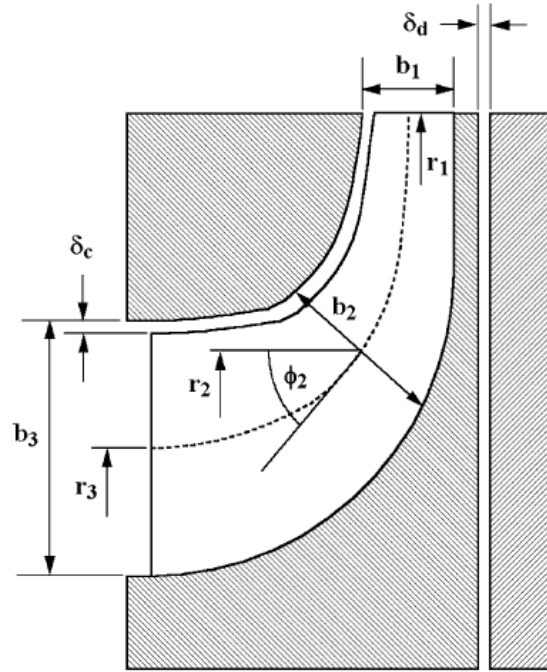


Figure 2.4 Side view of the rotor

The mass flow in terms of conditions at exit is:

$$\sin\beta_3 = \dot{m}/[(1 - \Delta)2\pi r_3 b_3 \rho_3 W_3] \quad (2-36)$$

Similar to the choked exit of nozzle, the choked meridional velocity is:

$$C_{m3} = \dot{m}/[(1 - \Delta)2\pi r_3 b_3 \rho_3] = a_3 \quad (2-37)$$

#### 2.4. Vaneless Space

Figure 2.5 illustrates a typical vaneless annular passage between two major components.

The swirl velocity of the inviscid core flow at any station can be obtained by conservation of angular momentum from the upstream parameters (subscript u) <sup>[4]</sup>:

$$C_\theta = C_{\theta u} r_u / r \quad (2-38)$$

The loss in the vaneless space includes profile loss of the boundary layer and entrance loss:

$$Y = Y_p + Y_{in} = (P_{tu} - P_{t3}) / (P_{t3} - P_3) \quad (2-39)$$

$$P_{t3} = (P_{tu} + YP_3)/(1 + Y) \quad (2-40)$$

In addition, the vaneless passage must require  $C_m \leq a$ . In the choke condition, the velocity is:

$$C_m = \frac{\dot{m}}{[2\pi r b \rho]} = a \quad (2-41)$$

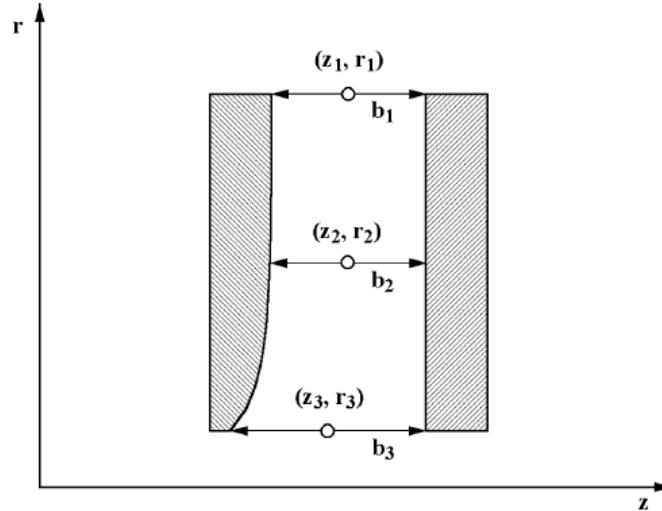


Figure 2.5 Sketch of the vaneless annular passage

## 2.5. The diffuser

The exhaust diffuser geometry is demonstrated in Figure 2.6.

The exhaust diffuser geometry is specified at inlet and exit, designated by subscripts 1 and 2. The geometric data specified at these stations are  $z$ ,  $r$  and  $\phi$ , as illustrated in Figure 2.6.

The linear distance between the two stations is

$$d = \sqrt{(z_2 - z_1)^2 + (r_2 - r_1)^2} \quad (2-42)$$

The curvature of the mean stream surface is proportional to the change in the slope angles,

$$\Delta\phi = |\phi_2 - \phi_1| \quad (2-43)$$

If  $\Delta\phi > 0$  the flow path is assumed to be a circular-arc segment, then

$$L = d\Delta\phi/[2\sin(\Delta\phi/2)] \quad (2-43)$$

Otherwise,  $L=d$ .

Through the diffuser, the velocity decreases, and assuming the process is isentropic gives:

$$h_{02} = h_{01}, h_2 - h_1 = \frac{1}{2}(C_1^2 - C_2^2) \quad (2-44)$$

The meridional velocity is,

$$C_{m2} = \dot{m}/(\rho_2 A_2) \quad (2-45)$$

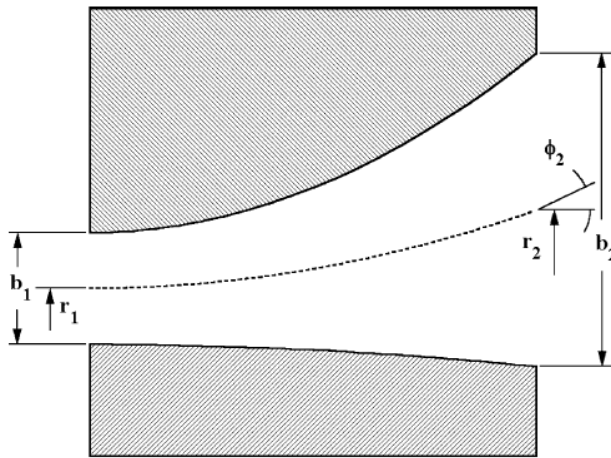


Figure 2.6 Sketch of the diffuser geometry

## CHAPTER 3. PERFORMANCE PREDICTION OF CENTRIFUGAL PUMPS WHEN RUNNING AS HYDRAULIC TURBINES

### 3.1. Introduction

Nowadays energy consumption is still increasing rapidly, and guaranteed, will increase even faster. Conventional fossil energy resources such as coal and oil create problems due to its rising price and fast depletion. Researchers have found various renewable energy like solar energy, wind energy, and hydraulic energy. Among all renewable resources, small hydropower (SHP) is one of the most promising sources of energy generation and it is catching much attention from developing countries, for example, India and Iran <sup>[24-29]</sup>. The small hydropower can be exploited from natural falls, irrigation systems, sewage systems, etc. The advantage of small hydropower plants over large hydropower plants is their environment-friendly nature, for they have no problems of large tremendous storage and rehabilitation of population. In addition, small hydropower projects can provide a solution for the energy problem in rural, remote and hilly areas, where the extension of the grid is techno-economically not feasible.

Although SHP seems very promising, it has a significant obstacle in its application. The main limitation in the installation of SHP plants is its higher cost of hydro turbines, as well as the turbine manufacturers usually do not manufacture the turbines in such small capacities. Also, it is very difficult, time-consuming and costly to develop site specific turbines correspond to local ecology in low capacity range.

Many investigators have attempted different kinds of turbines in small hydro range, such as crossflow turbines, single and multi-jet Pelton turbines and Francis turbines, but the results are not satisfying. It is reported that in small hydro range, a cross flow turbine requires a

large turbine running at slower speed, resulting in the need of a belt drive to power a standard generator. A Pelton turbine for such applications would require three or four jets, resulting in a complicated arrangement for the casing and nozzles. A small Francis turbine could also be used in this range, but it would be even more expensive than across flow turbine <sup>[25]</sup>.

In any water system which has excessive available energy e.g. natural falls, water supply, irrigation, sewage or rain systems, the application of a pump instead of a turbine seems to be an alternative solution in terms of easy implementation and reduced cost of equipment <sup>[30]</sup>. The pumps in turbine mode (pump as turbine PAT) have various advantages over conventional hydro turbines: low cost, less complexity, mass production, availability for a wide range of heads and flows, short delivery time, availability in a large number of standard sizes, ease of availability of spare parts, easy installation, etc. <sup>[31]</sup>. For low and very low capacity power plants (up to 500kW), the PAT deserves thoughtfulness due to a considerable reduction in the capital cost of the plant in spite of having slightly reduced efficiency. In this range, the investment cost for conventional hydro turbines is relatively high. The payback period of such hydro turbine can be as high as 15 years which can be reduced to 2 years using PAT for similar capacity <sup>[32]</sup>.

Numerous experimental, theoretical and numerical investigators <sup>[52-57]</sup> have shown that certain centrifugal and vertical pumps could be operated very satisfactorily as turbines over a limited range, but all investigators stress the need for knowledge, given the available turbine data how to select the appropriate pump.

Many investigators <sup>[58-63]</sup> confirm that a good designed centrifugal operating, with a high efficiency, may display good performance as a turbine, with a plus or minus 2% of the pump mode maximum efficiency. Two characteristics that are often displayed by investigators are the



pump and turbine mode of operations at a constant speed and the other, the turbine mode of operations at variable speed. Just as the pump mode possesses a head & efficiency Vs flowrate ( $H_p$  &  $\eta_p$  Vs  $Q_p$ ) performance curve for a constant speed, the turbine mode also possess a similar ( $H_T$  &  $\eta_T$  Vs  $Q_T$ ) characteristics.

In pump mode, the pump possesses a flat head vs. flow curve and fewer tendencies for pulsations. A comparative example of the characteristics of normal pump operation with the characteristics of the same unit in turbine mode, at the same speed, is shown in Figure 3.1, using test data from a pump with a specific speed of  $n_s = 1.20$ . The curves are normalized by the values of the head, flow, efficiency, and power of the pump at BEP. Figure 3.1, representing comparative characteristics of the same unit in pump and turbine mode, is an example of a single pump data ( $n_s=1.20$ ) which serves as the basis for such turbine performance prediction.

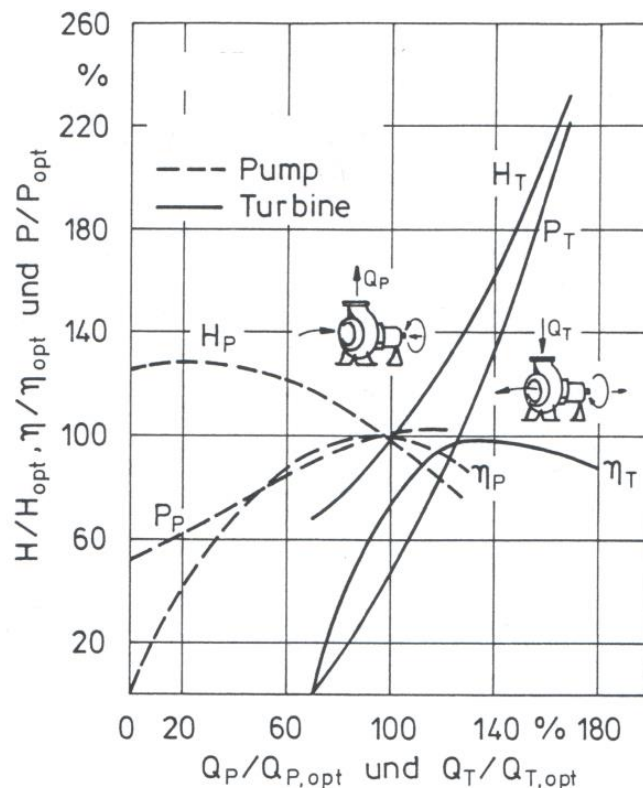


Figure 3.1 Pump and Turbine mode operation for a pump with  $n_s=1.20$  at constant rpm

Figure 3.2 shows on the basis of two different specific speeds ( $n_s = 0.58$  &  $1.20$ ) that the turbine mode of operation does not only function well with head and flow ( $H$  &  $Q$ ) variation but also can be run smoothly at variable speed. But both such plots (Figure 3.1, 3.2a & 3.2b) could only give part of the required data even for the very tested pump, let alone other pumps. Figure 1, 2a & 2b do not include turbine cavitation performance data. In conventional turbine design and selection practices, the knowledge of suction head and runner outlet condition is a priority. It is very surprising that the various literatures on PAT make very little mention of cavitation properties.

Numerous investigators have proposed charts and equations for selecting PATs. To select a PAT there are generally four known practices:

- 1) Based on similarity between best efficiency points (BEP) in both modes at the same speed, relationships are given between head, flow and efficiency ( $H_p \rightarrow H_T$ ,  $Q_p \rightarrow Q_T$  &  $\eta_p \rightarrow \eta_T$ ),
- 2) Statistical curve fits of large experimental data giving an empirical relationship,
- 3) Based on specific speed, and
- 4) Plots of charts with PATs together and conventional turbines.

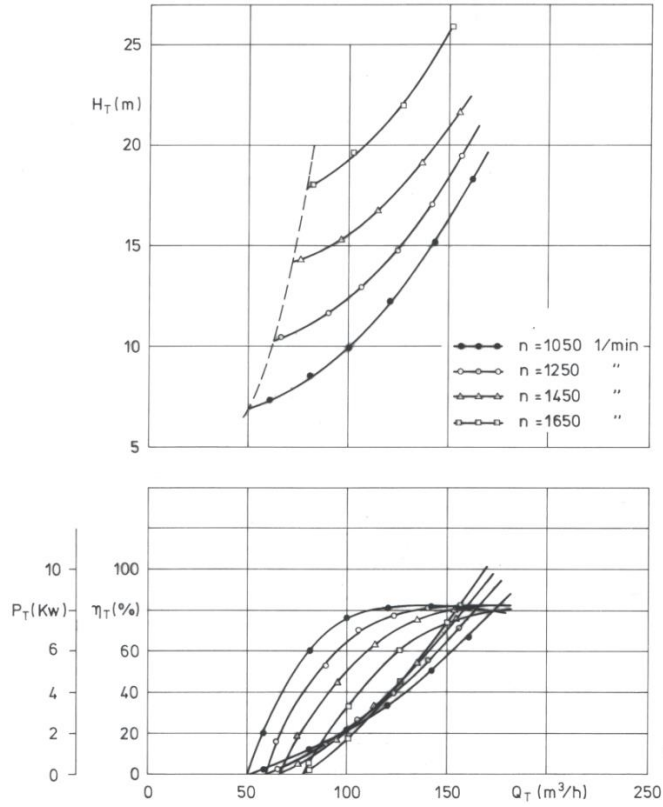


Figure 3.2a Turbine mode operation for a pump with  $n_s = 0.58$  at variable rpm

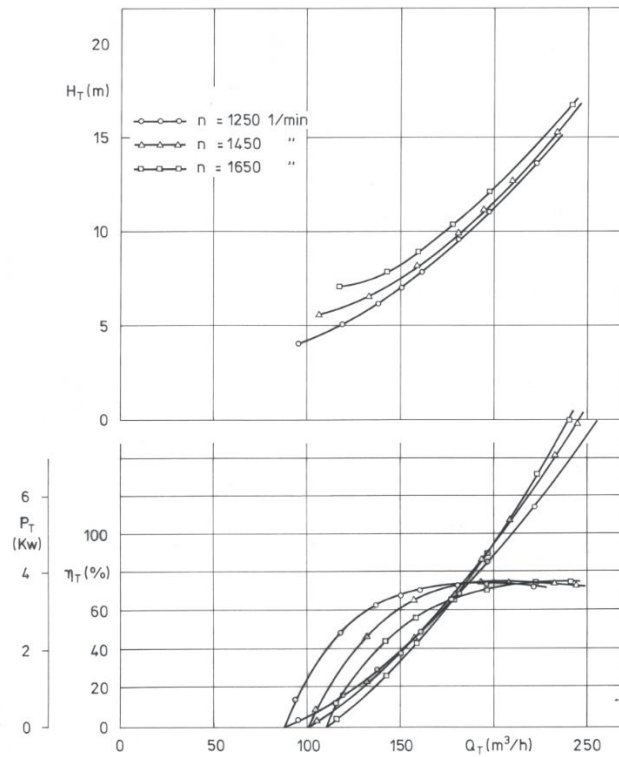


Figure 3.2b Turbine mode operation for a pump with  $n_s = 1.20$  at variable rpm

A typical combined all turbines chart proposed by Engeda et al. <sup>[64]</sup> (range: 1–1000kW) based on head and discharge is shown in Figure 3.3. Engeda et al. <sup>[64]</sup> showed in Figure 3.3 the possible applications of PAT relative to other conventional turbines. It is clear to see that indeed PATs have significant application niche area.

Despite the numerous literatures on Pumps PATs, only very few well-established and documented applications using this knowledge have been reported, therefore the lack of feedback of problems and experiences has not given sufficient incentive to the deeper examination of the fluid dynamics of the turbine mode flow.

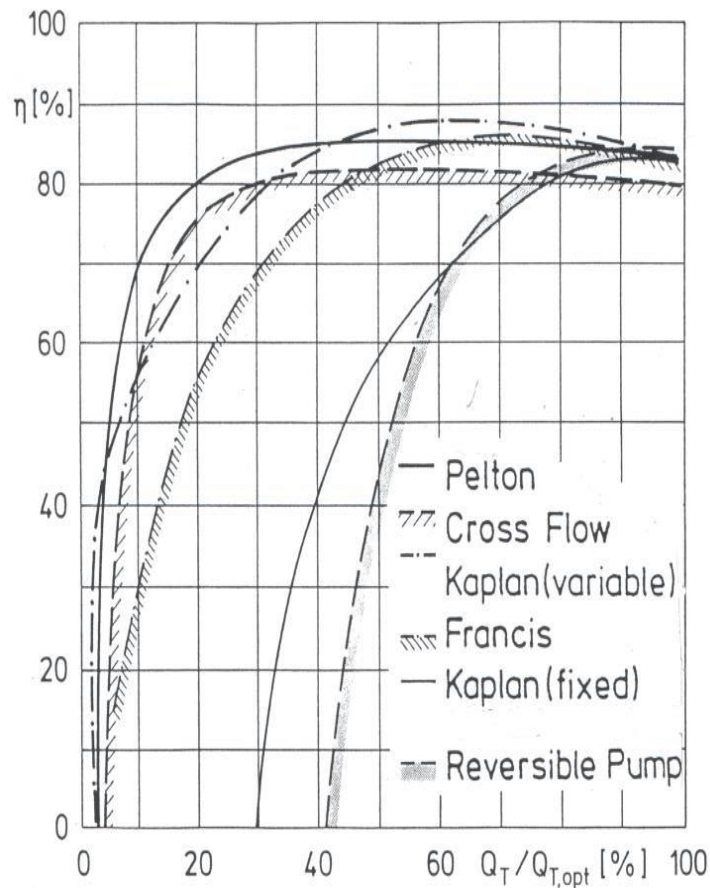


Figure 3.3 Application areas of conventional hydraulic turbines and PATs

Each pump possesses specific design configuration aimed for a particular duty. The biggest setback in the proper choice of turbines out of the vast pump series is the unavailability of information regarding geometrical and structural configurations, specific speed range and the design process and approached used. It is essential to have this lacking knowledge, in addition to the data and relationships supplied by many investigators, to able to select the best PAT.

### **3.1.1. Significance of pump type to select the appropriate pat**






Unlike conventional hydro turbines that come with variable geometry, PATs are with fixed geometric conditions as the flow enters the impeller from casing, resulting in poor part-load performance. This is one of the most serious problems for a hydropower system based on a PAT. In order to minimize this problem, the choice of an appropriate pump as turbine is essential.

A pump operating as a turbine is very sensitive towards changing boundary parameters, namely head and discharge. Hence a wrong pump selection will result a shift of the operating point, delivering the non-desired output and ultimately may even cause the failure of the project. Centrifugal pumps are commonly classified as single or multistage. If single stage, they are configured as: overhung and end suction, split case, vertical or submersible, etc. Furthermore, they are based on standards such as ASME, ISO, etc. Most published PAT data are without these important configurations, which all affect especially the part load of the PAT.



Figure 3.4 Configurations of the tested pumps - overhung end-suction with volute

Table 3.1 Pumps tested – geometry details

$n_s$	0.33	0.58	0.83	1.20	1.52
$d_1/d_{2(n_s=0.83)}$	0.64	0.66	0.65	0.65	0.82
$d_2/d_{2(n_s=0.83)}$	1.84	1.23	1.00	0.84	1.02
$b_2/d_{2(n_s=0.83)}$	0.08	0.12	0.15	0.16	0.27
$\beta_1$	$22^\circ$	$18^\circ$	$15^\circ$	$20^\circ$	$20^\circ$
$\beta_2$	$26^\circ$	$24^\circ$	$26^\circ$	$28^\circ$	$25^\circ$
Z	6	6	6	6	6
Geometry					

To make the data presented in this research meaningful and useful, five pumps were selected that have, identical configurations (overhung end-suction with volute), were based on similar design approaches and cover areas from very low specific speed to high values. Figure 3.4 shows the type of pump configuration used for the five pumps. Table 3.1 presents the pumps used in this research.

### 3.1.2. Performance and operation at BEP and off design areas

Dynamic turbomachines are reversible and have four different operating modes, and therefore a pump can run as a turbine. The inverse working mode of pumps as turbines was first investigated before by Kittredg<sup>[65]</sup>, Knap<sup>[66]</sup>, and Stepanof<sup>[62]</sup>. Knapp showed<sup>[66]</sup> that it is

possible to represent the four quadrant characteristics on a speed versus flow. These four quadrants correspond to four different operating modes.

As discussed above the BEP points of the pump in the two modes (Pump & turbine) are relatively easy to compare and correlate. However, the turbine performances of the pump at higher and partial flows are difficult to compare with that of the machine as a pump because the flows are different and the resulting losses also different. Certain reverse running pumps are known to suffer from flow separation in the runner due to excessive diffusion of blade surface velocities and distorted velocity profiles at runner exit, affecting the turbine performance of the machine, but these effects are not so adverse on the pump performance. The machine as a pump has been optimized on the basis of specific speed. But if the same specific speed is used to judge the machine's qualities in terms of runner diameter, speed and flow conditions, then it is seen that the machine is an over-designed turbine. For the same specific speed, a smaller turbine is more efficient. Therefore each pump as a turbine possesses a higher specific speed and it is doubtful whether most pumps possess optimum properties at these higher specific speeds as turbines.

The H-Q plot for the turbine performance for various speeds is bounded by two limiting curves, both passing through the origin. These boundaries are the runaway curve corresponding to H-Q values of zero torque and H-Q curve corresponding to zero speed. The turbine characteristic for each speed begins from the runaway curve and runs tangential to the locked-shaft curve, as shown in Figure 3.5. Each flow rate point on the runaway curve corresponds to a certain speed at which the machine begins to act as a turbine. This characteristic is true for most PATs, but experience shows that there are pumps, especially of

higher specific speed, whose H-Q curve cross the zero-speed line, hinting at some form of mismatching of hydraulic parts in turbine operation.

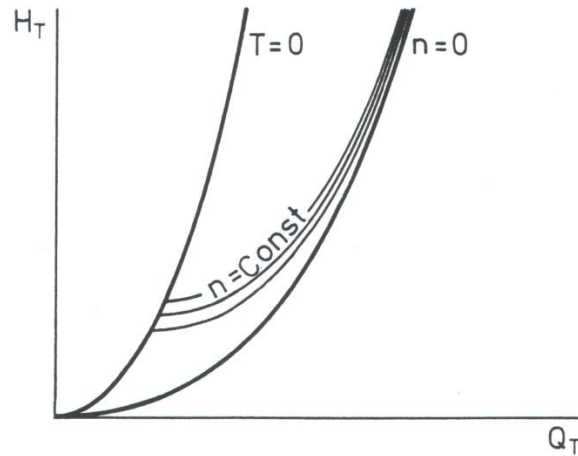


Figure 3.5 Limiting boundaries of PAT

Considering geometrical and structural configurations, specific speed range, cavitation characteristics and the design process and approached used, choice, selection, correlation and prediction of PATs can be performed with reasonable accuracy. This statement is confirmed by Figure 3.6 and Table 3.2, where the performances of carefully selected pumps are compared showing consistent characteristics that can be the basis for performance prediction and correlation.

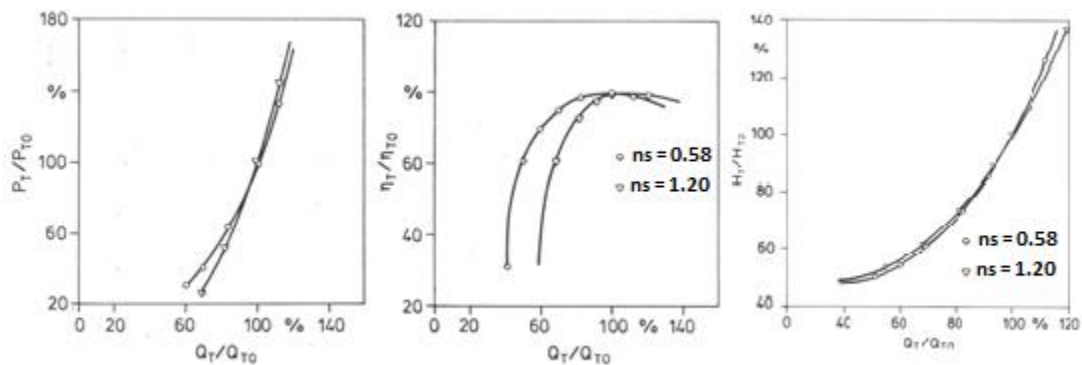







Figure 3.6 Turbine mode performance comparison for a pump with  $n_s = 0.58$  &  $1.20$



Table 3.2 Comparison of five pumps  $n_s = 0.33, 0.58, 0.83, 1.20$  and  $1.52$  carefully selected

$n_s$	0.33	0.58	0.83	1.20	1.52
N	1050 rpm	1450 rpm	1450 rpm	1450 rpm	1050 rpm
$\eta_P/\eta_{P(n_s=0.83)}$	0.87	0.98	1.00	0.96	1.01
$\eta_T/\eta_{P(n_s=0.83)}$	0.78	0.97	1.01	0.88	0.93
Geometry					

### 3.1.3. Challenges

One of the major disadvantages of a PAT is that it is a fixed geometry machine resulting in poor part load and narrow range performance in comparison with conventional turbines of the same size. This could only be improved through modifications to include some form of adjustable guide vanes, which highly raises the cost of the unit. In this regard, more studies are required for the proper understanding of the turbine operation of pumps, in order to lay down some criteria for identifying the suitable pumps for specific turbine operation.

One of the reasons of the narrow range performance can be explained by Figure 3.7 and Figure 3.8. The rotation direction of turbine mode is opposite to pump mode. At the best efficiency point in turbine mode, the flow should have the minimum incidence loss. However, at part-load and over-load conditions, the incidence loss will be massive due to the sharp blade and small tangential inlet blade angle.

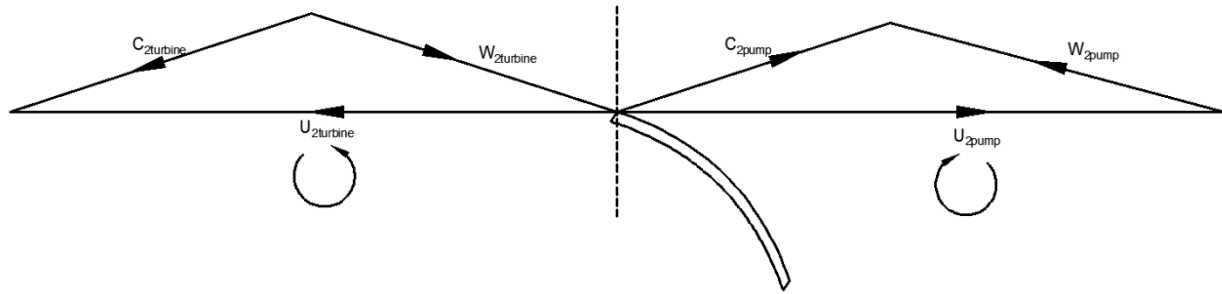


Figure 3.7 Velocity triangles at the outlet of the pump and inlet of the turbine

In addition to this current research, two other contributions have attempted to describe the turbine performance as a function of specific speed. According to Buse<sup>[19]</sup>, the shape of the turbine head-capacity (H-Q) curve is highly dependent on the specific speed of the unit as a pump. Hergt et al,<sup>[20]</sup> suggested a classification of the turbine optimal characteristics as a function the turbine specific speed of the unit.

As this research shows, effective and accurate correlations through specific speed require:

- 1) Used pumps must cover a good representative specific speed range.
- 2) Pumps must belong to a family of pumps designed under similar criterion.
- 3) Pumps must be well designed using similar state of the art technology
- 4) Pumps must have similar geometrical configurations in terms of inlet-impeller-diffuser-volute.

But to the present researcher's knowledge the best suited and reliable classification of the PAT characteristics with specific speed, using any pump data of any configuration, is that of the flow at zero power. The flow corresponding to the head at zero turbine power output as a ratio of the turbine flow at the BEP point strongly depends on the pump specific speed of the unit for any configuration pump. As shown in Figure 3.9.

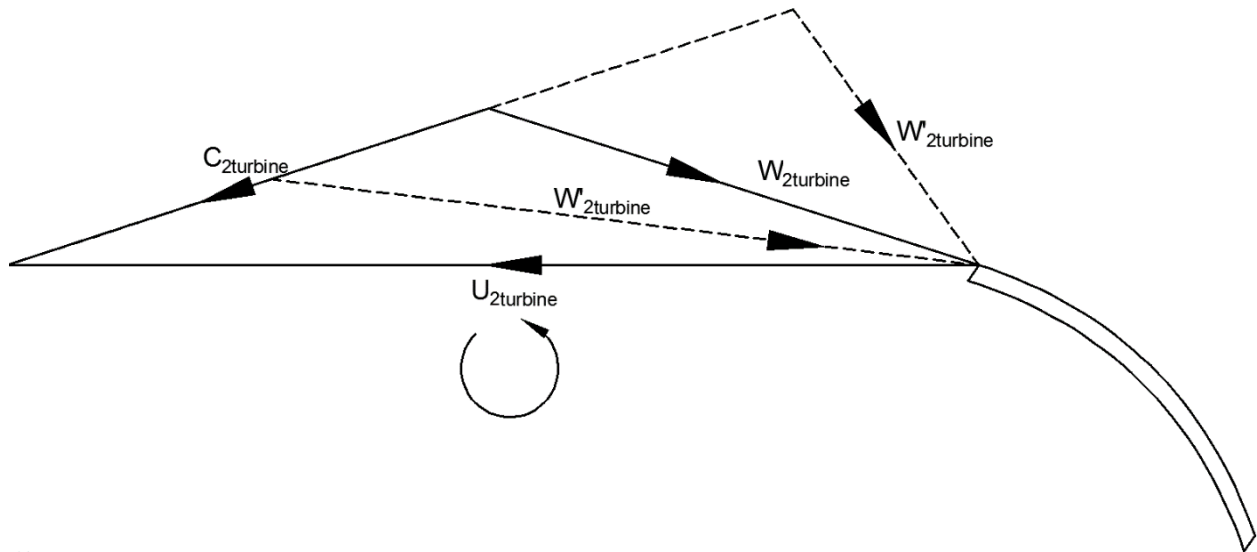


Figure 3.8 Velocity triangles in turbine mode at part-load and over-load conditions

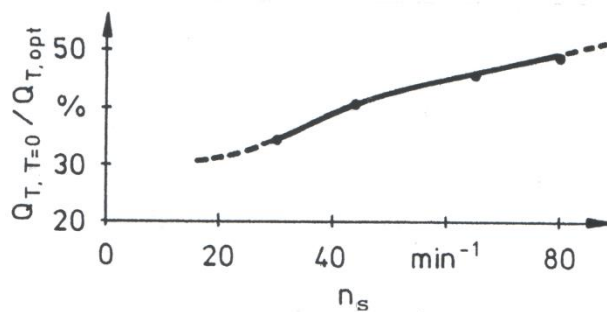


Figure 3.9 PAT flow corresponding to the head at zero turbine power output

#### 3.1.4. Performance prediction of pump as turbine

The performance of the pump running as turbine is different from the performance in pump mode. However, the pump manufacturers do not provide the characteristics running in turbine mode. Therefore, performance prediction of PAT is very important, because it determines whether the selected pump is able to work in optimum performance. One of the main objectives of all PAT researchers all over the world has been to build a method that would make accurate predictions of the turbine operation of pumps.

A large number of experimental and theoretical studies have been made by lots of researchers. The first objective of these researchers was to find the relations of best efficiency point (BEP) parameters between the pump mode and turbine mode of the same machine. An accurate guess in BEP will give the investor a proper preliminary selection of the pump. Simple relations in terms of head and discharge correlations have been developed, which are defined as:

$$h = \frac{H_t}{H_p} \quad (3-1)$$

$$q = \frac{Q_t}{Q_p} \quad (3-2)$$

In addition, the performance differences based on various specific speeds are of significant importance as well.

Stepanoff, Childs, Hancock, McClaskey and Lundquist, Sharma, Luneburg and Nelson, Schmiedl and Alatorre-Frenk developed relations based on efficiency in pump mode; whereas, Kittredge, Diederich, Grover, Lewinski&Keslitz, Hergt, and Buse derived the relations based on the specific speed of the pump <sup>[24, 25]</sup>. These researchers proposed many methods to predict the performance, but the deviations between the prediction and reality have been found to be around 20% or even more. In addition, very few of the researchers produced the method that could predict no-load, part load and full load performances.

Few other researchers like Knapp, Wong, Cohrs and Amelio and Barbarelli have also given the PAT prediction methods based on the pump design, its geometry and assumptions of some complex hydraulic phenomena like losses and slip effects to come up with a more accurate method. These methods are quite comprehensive but they are difficult to put in

practice and outside the reach of planners since these methods necessitate very detailed information, which is sometimes patented or available only with the manufacturers.

In recent years, many researchers have used different theoretical and experimental techniques to predict the PAT performance from pump characteristics.

Sharma <sup>[33]</sup> discussed the suitability of different pumps which can be used as turbines. The analysis of performance curves in the pump and turbine mode plotted by Grant and Bain <sup>[36]</sup> revealed that the location of turbine BEP is at a higher flow and head than the pump BEP. However, it was pointed out that the proposed equations were only approximate and the actual values of  $Q_t$  and  $H_t$  might vary by 20% of the predicted value for the BEP. Hence, after initial selection, it was recommended to test the pump under turbine condition to find out power at the available head.

Williams <sup>[37]</sup> compared eight different PAT performance prediction methods based on turbine tests on 35 pumps in the specific speed range of 12.7–183.3 and studied the effects of poor turbine prediction on the operation of a PAT. None of the eight methods had given an accurate prediction for all the pumps but Sharma's method was found to be better than the other methods; hence, it was recommended as a first estimate for prediction of the turbine performance. However, it is also suggested that before the installation, the selected pump is necessary to be tested in turbine mode on the site.

Joshi et al. <sup>[38]</sup> established the relationship between pump and turbine specific speeds ( $N_{sp}$  and  $N_{st}$ ), for selection of PAT particularly for low head sites. To select the pump which can be used as a turbine, the value of specific speed in turbine mode can be read from their  $N_{sp}$  and  $N_{st}$  plot. The approach had the advantage of simplicity yet of no generality because it was based

on the data of only three pumps. Hence, the method is recommended for approximate analysis only.

Punit Singh and Franz Nestmann proposed optimized prediction method. The approach was based on experimental results of 9 models of PAT (Nsp: 20–80 rpm) and the fundamentals of applied turbomachinery like the specific speed–specific diameter plot (called the Cordier/Balje plot) <sup>[33, 34]</sup>. The method was experimentally evaluated for three pumps with specific speeds of 18.2rpm, 19.7rpm, and 44.7rpm, and the error in turbine performance prediction was found to be within 4% in the full load operating range. However, the deviations in part load and no-load operation were quite large. It was reported that the application of the proposed model was quite simple and could be incorporated in any computer program which could be made accessible to small manufacturers and system planners particularly for energy recovery or micro hydro projects.

Yang et al. <sup>[39]</sup> developed a theoretical method to predict the performance of PAT. The method was tested both numerically (with ANSYS-CFX) and experimentally and compared to the methods proposed by Stepanoff and Sharma. However, considerable errors (5%-10%) still existed, which might be caused by leakage loss through balancing holes, mechanical loss caused by the mechanical seal and bearings and the surface roughness value set on the machine's surface.

Derakhshan and Nourbakhsh <sup>[28, 29]</sup> derived some relations to predict BEP of PATs based on the experimental work carried out on four centrifugal pumps with different specific speeds of 14.6, 23, 37.6 and 55.6. A new method was proposed to predict BEP of PAT based on hydraulic specifications of the pump, particularly the specific speed, which represents the

runner type and consequently its hydraulic behavior. Also, the more efficient pump operates as turbine at larger values of  $h$  and  $q$ . The predicted  $h$  and  $q$  by this method were found in good agreement with the experimental results. A procedure to choose a proper centrifugal PAT for a small hydro-site with  $N_s$  to 150 based on  $h$  and  $q$  was presented as mentioned below.

$$h_{new} = h(0.25/D)^{1/4} \quad (3-3)$$

$$q_{new} = q(0.25/D)^{1/6} \quad (3-4)$$

Nautiyal, et al. <sup>[26]</sup> developed relations using experimental data of the tested pump ( $N_s=18(m, m^3/s)$ ) and pumps of some previous researchers to predict turbine mode performance from pump mode characteristics. The experimental results were presented in the form of non-dimensional parameters, head coefficient, discharge coefficient and power coefficient. As compared to other methods, the deviation between experimental results and results obtained by proposed relations was less which made the performance prediction of PAT simpler and closer to accuracy. However, some uncertainties were still found in prediction of turbine mode characteristics using pump operation data. The relation ( $\chi$ ) between best efficiency and specific speed of pump was developed by regression analysis and equations of  $h$  and  $q$  were developed which are expressed below:

$$\chi = \frac{\eta_p - 0.212}{\ln(N_s)} \quad (3-5)$$

$$q = 30.303\chi - 3.424 \quad (3-6)$$

$$h = 41.667\chi - 5.042 \quad (3-7)$$

In general, conversion factors for PAT can be obtained on the basis of theoretical and numerical studies but the performance of PAT cannot be anticipated perfectly. Further investigations to develop a common model for deriving the conversion factors are needed.

Additionally, it is necessary to gather more reliable and actual data for validation of prediction methods.

### **3.1.5. Performance improvement in PAT**

Conventional hydro turbines usually show higher efficiency than the pumps which are designed for the similar operating conditions. Many investigators have attempted different techniques to improve the performance of PAT. It is reported that the optimum efficiency of PAT can be generally achieved when the shock losses at the pump impeller tips become nearly zero. Therefore, the modification must be made to the impeller tips of the pump.

Singh et al. <sup>[34]</sup> studied various possibility of modifying the inlet casing: by rounding of inlet edges of the blade, by modifying the inlet casing rings, by enlarging the suction eye, by removing the casing eye rib. It was revealed that, among the different modifications proposed, the impeller blade rounding was the most beneficial.

Other researchers such as Suarda, Derakhshan and Yang <sup>[40]</sup>, also verified that rounding the rotor tip can improve the efficiency. It was found that the reduction in impeller diameter results in a slight shift in optimal discharge towards the left along with a slight drop in hydraulic efficiency.

Sheng et al. applied splitter blade technique to improve the PAT performance which is one of the methods used in flow field optimization and performance enhancement of rotating machinery. It was observed that with the increase of splitter blades head was dropped but efficiency was increased over the entire operating range.

Among the various techniques attempted by different researchers for performance improvement of PAT, the impeller blade rounding is found to be the most promising technique.



However, it is more advantageous with large capacity PATs in view of their higher efficiency compared to small PATs. It is also required to standardize the impeller blade rounding effects over the wide range of PATs.

In summary, PATs are promising for small hydraulic power resource. However, it is still required to propose more accurate predictions of performance in turbine mode from the characteristics in pump mode. In addition, modifications on the pump to increase the efficiency are important, yet standardized methods of improving the PATs have not been established.

### 3.2. Previous Prediction Method

Before installing a PAT, a precise prediction of the turbine mode performance is essential to the efficient utilization of hydraulic power. Therefore, easy and accurate prediction methods are required. Over decades, numerous studies have been theoretically, experimentally and numerically conducted to obtain an effective prediction technique.

#### 3.2.1. Theoretical

The earliest published theoretical study was in 1962 by Childs <sup>[37]</sup>. The equations are yielded based on rough assumptions: The best efficiencies in pump mode and turbine mode are equal. In addition, the output power of turbine and input power of pump should be same. Same assumptions were used by later researchers such as McClaskey and Lundquist, Lueneburg and Nelson and Hancock <sup>[37]</sup>.

With a similar method, Stepanoff <sup>[37]</sup> proposed two equations to calculate discharge and head in turbine mode relating the best efficiency in pump mode.

$$\frac{Q_{bt}}{Q_{bp}} = \frac{1}{\sqrt{\eta_{bp}}}, \frac{H_{bt}}{H_{bp}} = \frac{1}{\eta_{bp}} \quad (3-8)$$

Sharma <sup>[37]</sup> also developed a method based on Childs' assumptions:

$$\frac{Q_{bt}}{Q_{bp}} = \frac{1}{\eta_{bp}^{0.8'}} \frac{H_{bt}}{H_{bp}} = \frac{1}{\eta_{bp}^{1.2}} \quad (3-9)$$

Later, detailed hydraulic studies were done on the geometry and performance. Alatorre-Frenk <sup>[41]</sup> did analysis in his dissertation, but no prediction technique was actually proposed.

Gulich <sup>[42]</sup> predicted the performance by analyzing the hydraulic losses in pumps and turbines mode. In his book, he proposed a very detail prediction procedure counting all the losses. However, this procedure requires very detailed geometry and testing data. For an actual project, this method is not practical because the manufacturer will not provide detailed geometry and testing data, although the method was claimed to be very accurate.

Shahram Derakhshan <sup>[28, 29]</sup> also did some hydraulic analysis regarding the geometry and losses in one of his papers. However, he did not present an applicable prediction method based on his analysis. In another paper of his together with Yang <sup>[39]</sup>, Yang and Shahram presented a method in a similar style of Sharma's method.

$$\frac{H_{bt}}{H_{bp}} = \frac{1.2}{\eta_{bp}^{1.1'}} \frac{Q_{bt}}{Q_{bp}} = \frac{1.2}{\eta_{bp}^{0.55}} \quad (3-10)$$

G Ventrone <sup>[43]</sup> theoretically proposed a prediction method in terms of very detailed geometrical data. The prediction resulted in very low error (within 4%). However, same with Gulich, the requirement of detailed geometry made Ventrone's method not very practical.

$$\phi_T = \frac{\Delta\psi + \left[ \left(1 - \frac{\Delta U_o}{U_i}\right) + \left(1 + \frac{\Delta U_o}{U_i}\right) \frac{D_o^2}{D_i^2} \right]}{\eta_v \left( \frac{\cot\alpha_{iT}}{\xi_i} + \frac{B_i \cot\beta_{ob}}{B_o \xi_o} \right) + \frac{1}{\eta_v} \frac{\cot\beta_{ib}}{\xi_i}} \quad (3-11)$$

### 3.2.2. Experimental

Other than theoretical research, many experimental studies were practiced. Five prediction methods available in publications are listed below:

Alatorre-Frenk's method <sup>[37]</sup>:

$$\frac{H_{bt}}{H_{bp}} = \frac{1}{0.85\eta_p^5 + 0.385}, \frac{Q_{bt}}{Q_{bp}} = \frac{0.85\eta_p^5 + 0.385}{2\eta_p^5 + 0.205} \quad (3-12)$$

Schmiedl's method <sup>[37]</sup>:

$$\frac{Q_{bt}}{Q_{bp}} = -1.4 + \frac{2.5}{\eta_{hp}}, \frac{H_{bt}}{H_{bp}} = -1.5 + \frac{2.4}{\eta_{hp}^2} \quad (3-13)$$

Grover's method <sup>[37]</sup>:

$$\frac{H_{bt}}{H_{bp}} = 2.693 + 0.0229N_{st}, \frac{Q_{bt}}{Q_{bp}} = 2.379 + 0.0264N_{st}, 10 < N_{st} < 50 \quad (3-14)$$

Hergt's method <sup>[37]</sup>:

$$\frac{H_{bt}}{H_{bp}} = 1.3 - \frac{6}{N_{st} - 3}, \frac{Q_{bt}}{Q_{bp}} = 1.3 - \frac{1.6}{N_{st} - 5} \quad (3-15)$$

Shahram Derakhshan <sup>[28]</sup>

$$\left(\frac{H_{bt}}{H_{bp}}\right)^{-0.5} = 0.0233N_{sp} + 0.6464, N_{st} = 0.9413N_{sp} - 0.6045,$$

$$N_{pst} = 0.849N_{p_{sp}} - 1.2376 \quad (3-16)$$

Nautiyal <sup>[26]</sup>:

$$\chi = \frac{\eta_p^{-0.212}}{\ln(N_s)}, \frac{Q_{bt}}{Q_{bp}} = 30.303\chi - 3.424, \frac{H_{bt}}{H_{bp}} = 41.667\chi - 5.042 \quad (3-5-3-7)$$

Sanjay V. Jain <sup>[44]</sup>:

$$\eta_{BEP} = B_0(D/D_r)^{n_1}(N/N_r)^{m_1}\exp(n_2[\ln(D/D_r)]^2) \times \exp(m_2[\ln(N/N_r)]^2) \quad (3-17)$$

All the correlations derived from experiments are fitting equations based on a limited number of PAT data. Therefore, the correlations are not universal and are usually restricted in certain ranges of specific speed.

Besides creating correlations, Singh proposed a consolidated model and a routine integrating the previous methods to minimize the error <sup>[33, 34]</sup>.

### 3.2.3. Numerical studies

Recently published studies have been using CFD techniques to predict the performance. The results in these papers were satisfying. However, numerical solutions are not practical because they need exactly designed geometry of the pump, which is not available from the manufacturer usually. <sup>[28, 39, 45]</sup>

Apart from being classified as experimental and theoretical methods, prediction correlations can also be sorted by type of data based on, such as best efficiency point (BEP) based, specific speed based. Some researchers propose their prediction technique according to the pumps' geometry. Table 3.3 presents the classifications of previous prediction methods mentioned above for a clear view.

Table 3.3 Classifications of previous prediction methods

	Experimental	Theoretical	BEP Based	Geometry based	Specific Speed based
Stepanoff's		✓	✓		
Sharma's		✓	✓		
Gulich	✓	✓		✓	
Ventrone		✓		✓	
Yang's		✓	✓		
Alatorre-Frenk's	✓		✓		
Schmiedl's	✓		✓		
Grover's	✓				✓
Hergt's	✓				✓
Shahram's	✓				✓
Nautiyal's	✓				✓
Jain's	✓			✓	

Figures 3.10-3.15 display the variations of efficiencies, heads and power against flow rates. In these figures, flow coefficient,  $\phi$ , head coefficient,  $\psi$ , and power coefficient,  $\mu$ , are calculated by:

$$\phi = \frac{Q}{\omega D_o^3} \quad \psi = \frac{gH}{(\omega D_o)^2}, \quad \mu = \frac{P}{\rho \omega^3 D_o^5} \quad (3-18)$$

In the equation H (m), Q (m<sup>3</sup>/s) and P (W) are head, flowrate and power respectively.  $\omega$  (rad/s) is rotational speed and D<sub>o</sub> (m) is impeller diameter.

Figure 3.10 and Figure 3.11 are the relations between efficiencies and flow coefficient in pump mode and turbine mode. All the data points are poly-curved and the best efficiency points (BEPs) are found by seeking the peak points of the fitting curves.

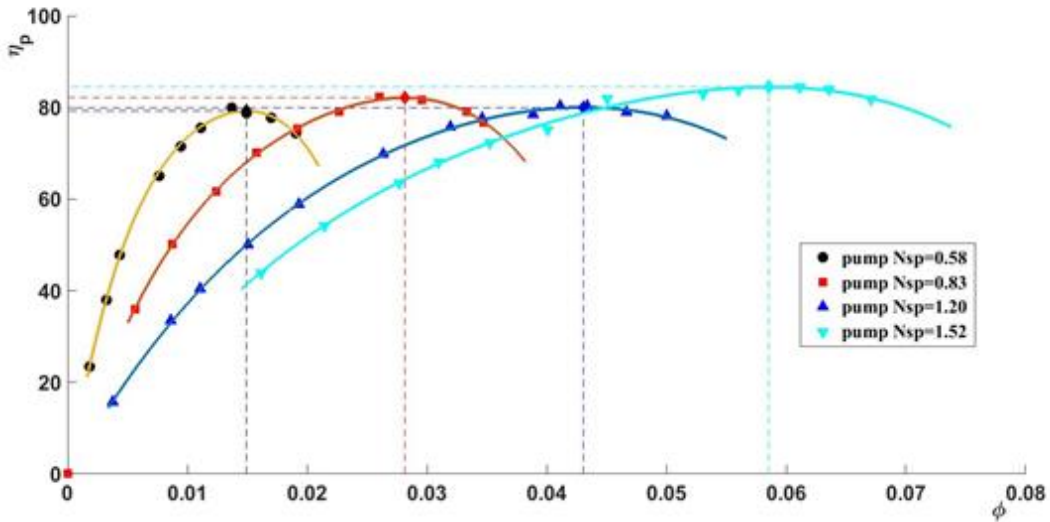


Figure 3.10 Efficiency in Pump Mode vs Flow-Coefficient

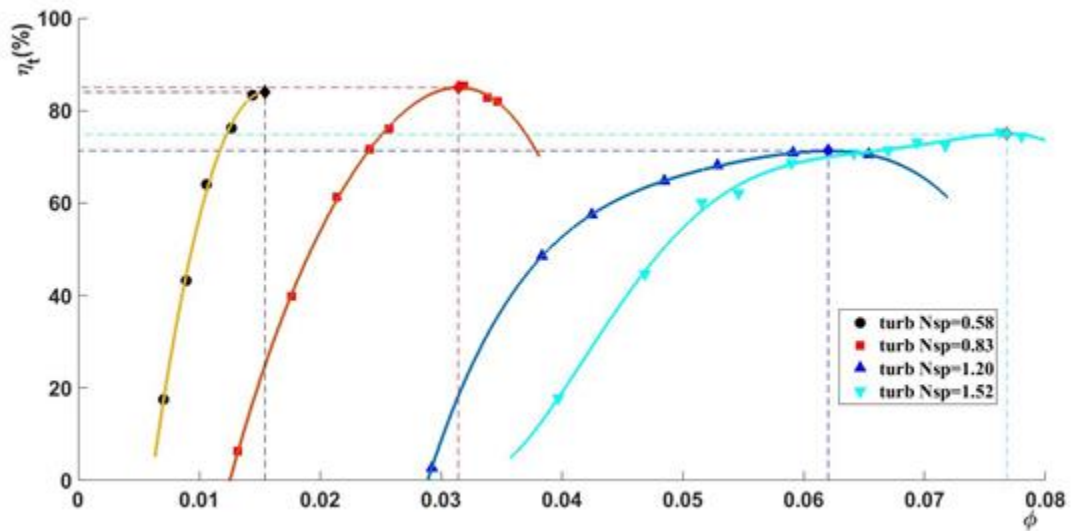


Figure 3.11 Efficiency in Turbine Mode vs Flow-Coefficient

Fig. 3.12 and Fig. 3.13 display the head coefficients changing with flow. Fig. 3.14 and Fig. 3.15 show the variations of power coefficients with flow. Inserting the best efficiency flow rate yields the head and power at the BEPs.

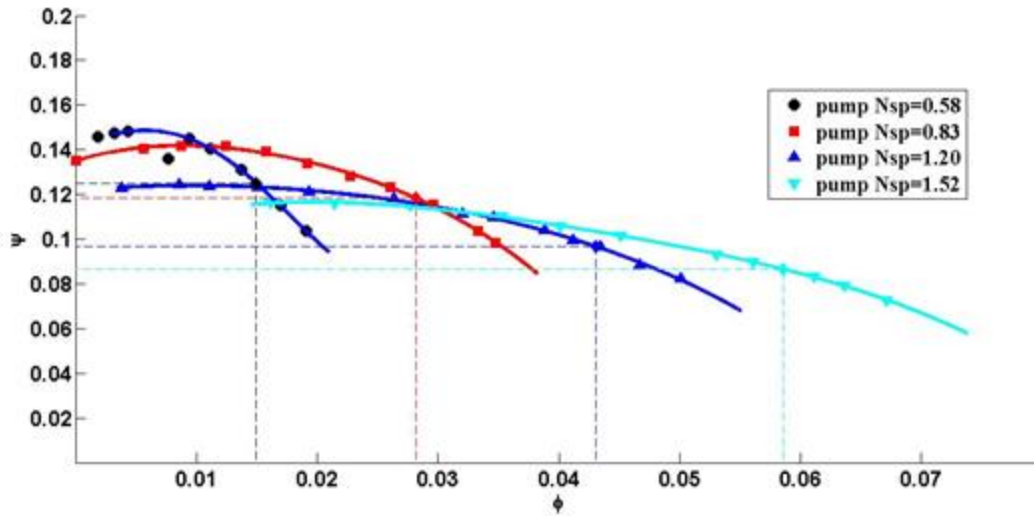


Figure 3.12 Head-Coefficient vs Flow-Coefficient in Pump Mode

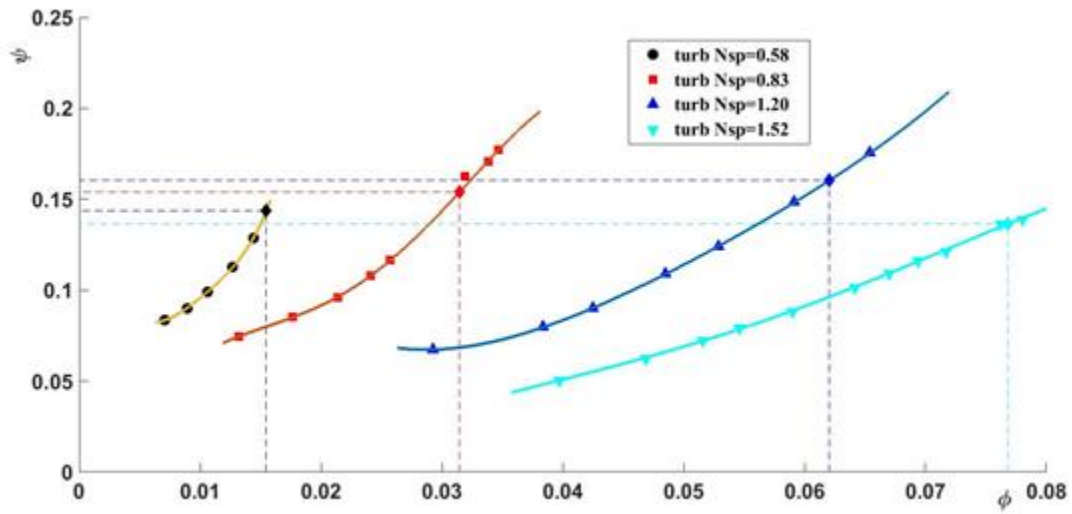


Figure 3.13 Head-Coefficient vs Flow-Coefficient in Turbine Mode

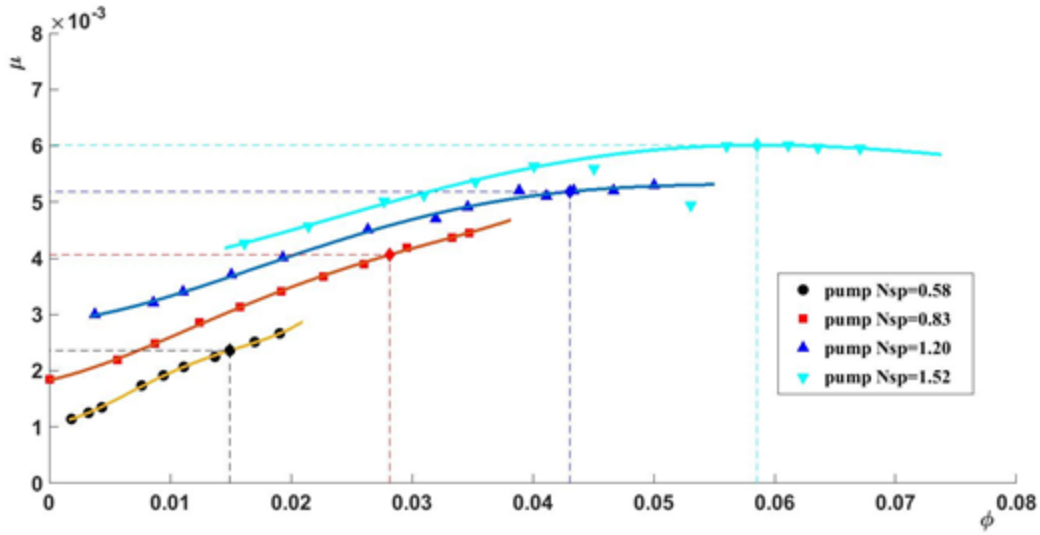


Figure 3.14 Power-Coefficient vs Flow-Coefficient in Pump Mode

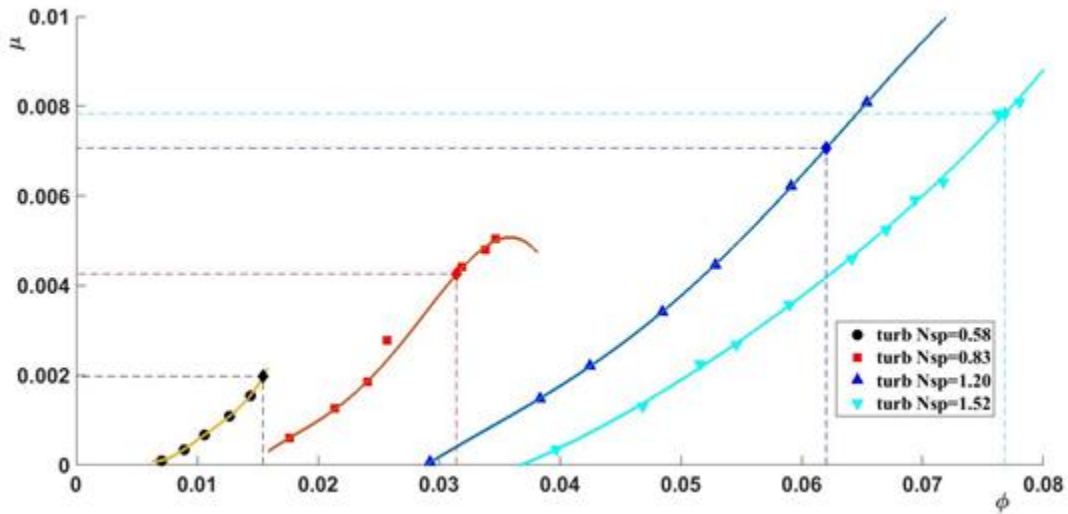


Figure 3.15 Power-Coefficient vs Flow-Coefficient in Turbine Mode

After collecting all of the BEP data, the specific speed, power specific speed and specific diameter relations between pumps mode and turbine mode can be drawn, see as Figure 3.16 Figure 3.17 and Figure 3.18. Specific speed, specific diameter and power specific speed are calculated as:

$$N_s = \frac{\omega Q_b^{0.5}}{(gH_b)^{0.75}} \quad D_s = \frac{D_o H_b^{0.25}}{Q_b^{0.5}} \quad N_{ps} = \frac{\omega(P/\rho)^{0.5}}{(gH_b)^{1.25}} \quad (3-19)$$



In the equation  $Q_b$  ( $m^3/s$ ),  $P$  (w) and  $H_b$  (m) are the flow rate power and head at BEP.

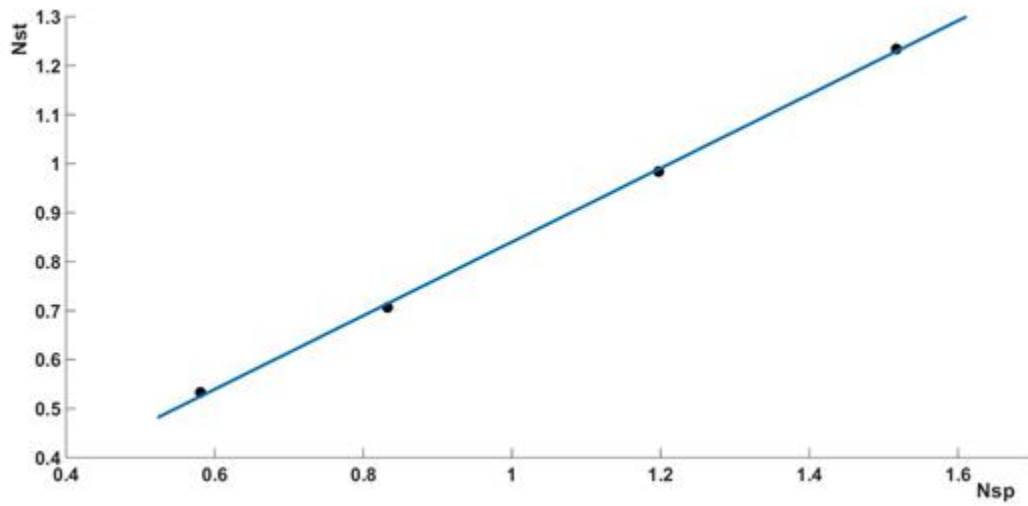


Figure 3.16 Specific Speeds between Pump Mode and Turbine Mode

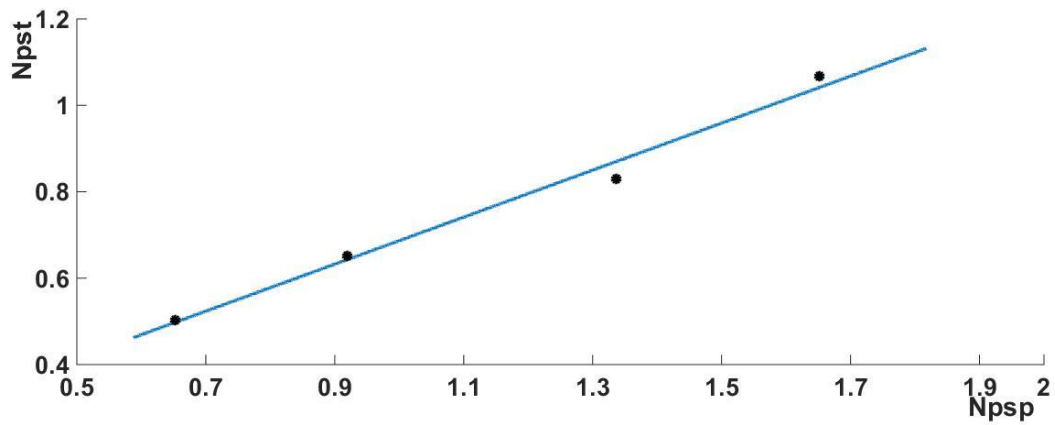


Figure 3.17 Power Specific Speeds between Pump Mode and Turbine Mode

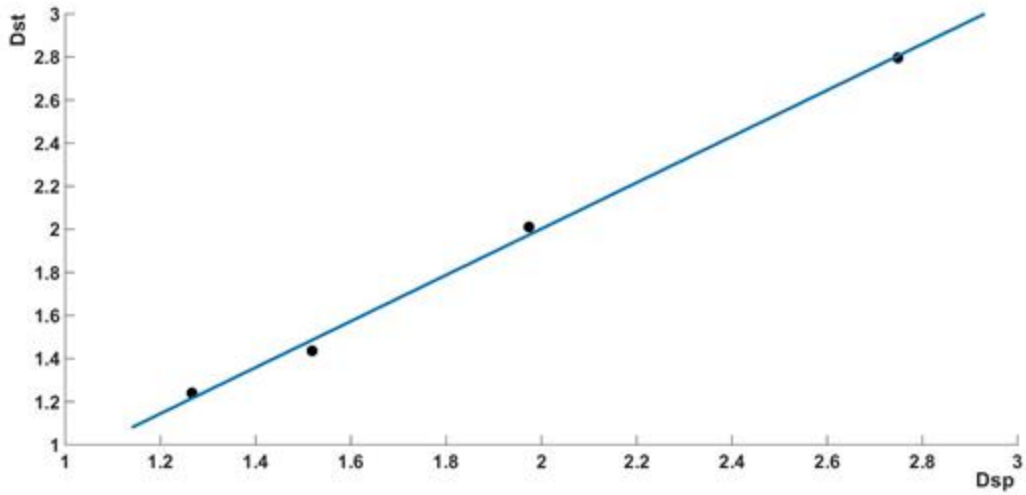


Figure 3.18 Specific Diameters between Pump Mode and Turbine Mode

In addition, each pump's efficiency ratio is defined as:

$$\eta_r = \frac{\eta_{bp}}{\eta_{bt}} \quad (3-20)$$

$\eta_{bp}$  and  $\eta_{bt}$  are the best efficiency running in pump mode and turbine mode. Figure 3.19 displays the relation between specific speed in pump mode and efficiency ratio.

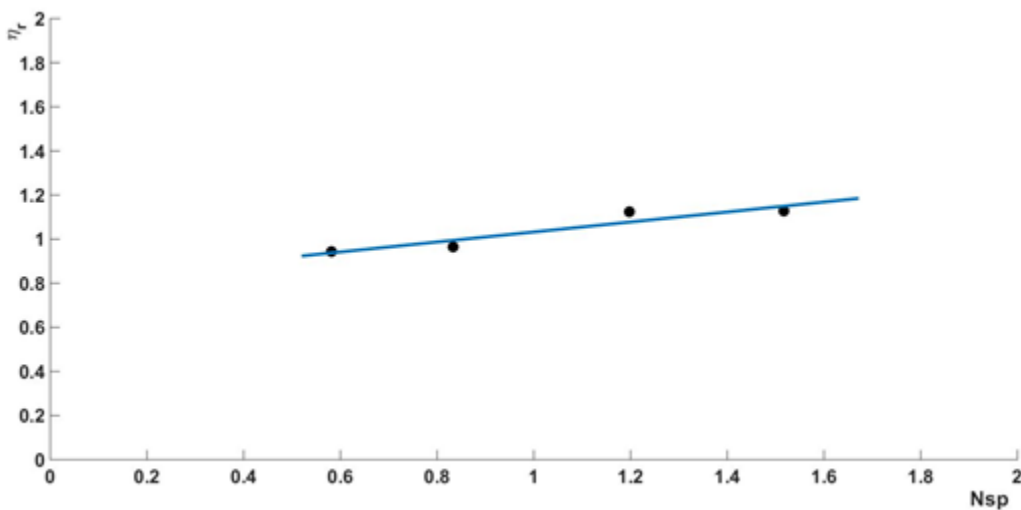


Figure 3.19 Efficiency Ratio vs Specific Speed in Pump Mode

### 3.3. Performance prediction

#### 3.3.1. Prediction method

In Figure 3.17 and 3.18, correlations of specific speed and specific diameter between both operation modes are found to be approximately linear. Furthermore, the efficiency ratio varies with pump specific speed linearly as seen in Figure 3.19. The linear curve fit is found to be:

$$N_{st} = 0.7520N_{sp} + 0.0883 \quad (3-21)$$

$$D_{st} = 1.072D_{sp} - 0.1419 \quad (3-22)$$

$$\frac{\eta_{bp}}{\eta_{bt}} = 0.2267N_{sp} + 0.8057 \quad (3-23)$$

$$N_{pst} = N_{st} * \sqrt{\eta_{bt}} \quad (3-24)$$

According to the relation between specific speed based in terms of head (m) and power specific speed in terms of power (W), power specific speed can be obtained from Equation 3-24.

Therefore with the above equations, head, flow and power in turbine mode can be calculated from the estimated specific speed and specific diameter in turbine mode.

$$H_{bt} = \left( \frac{\omega D_o}{N_{st} D_{st} g^{3/4}} \right)^2 \quad (3-25)$$

$$Q_{bt} = \frac{D_o^3 \omega}{g^{3/4} D_{st}^3 N_{st}} \quad (3-26)$$

$$P_{bt} = \eta_{bt} Q_{bt} \rho g H_{bt} \quad (3-27)$$

Power specific speed is also a dimensionless group including power and head. However, if to obtain the flow from power specific speed, an estimated efficiency has to be involved, therefore the uncertainty and errors will be significantly larger than the ones in Equation 3-26. Therefore, it should be more accurate to calculate head and flow using specific speed in terms of head (m) and specific diameter as shown in Equation 3-25 and Equation 3-26.

### 3.3.2. Prediction results

Table 3.4 Predicted performances compared with tested data

		$N_{st}$	$N_{pst}$	$D_{st}$	$H_{bt}$ (m)	$Q_{bt}$ (m <sup>3</sup> /s)	$\eta_{bt}$	$P_{bt}$ (kw)
Pump1	Tested data	0.5332	0.5037	2.7964	24.438	0.0457	84.1%	9.7854
	Predicted results	0.5320	0.4896	2.8001	24.480	0.0457	84.5%	9.2662
	Error	<b>-0.22%</b>	<b>-2.81%</b>	<b>0.13%</b>	<b>0.17%</b>	<b>-0.18%</b>	<b>0.56%</b>	<b>-5.31%</b>
Pump2	Tested data	0.7216	0.6764	1.9953	17.369	0.0502	85.0%	7.5136
	Predicted results	0.7194	0.6527	1.9709	17.913	0.0523	82.6%	7.5807
	Error	<b>-0.31%</b>	<b>-3.51%</b>	<b>-1.22%</b>	<b>3.14%</b>	<b>4.09%</b>	<b>-2.86%</b>	<b>0.89%</b>
Pump3	Tested data	0.9833	0.8287	1.4355	12.895	0.0596	71.3%	5.3562
	Predicted results	0.9916	0.8554	1.4824	11.892	0.0537	74.3%	4.6524
	Error	<b>0.84%</b>	<b>3.23%</b>	<b>3.27%</b>	<b>-7.78%</b>	<b>-9.95%</b>	<b>4.23%</b>	<b>-13.1%</b>
Pump4	Tested data	1.2347	1.0672	1.2391	8.4400	0.0949	75.0%	5.8707
	Predicted results	1.2298	1.0541	1.2129	8.8777	0.1016	73.5%	6.5026
	Error	<b>-0.39%</b>	<b>-1.23%</b>	<b>-2.11%</b>	<b>5.19%</b>	<b>7.04%</b>	<b>-1.95%</b>	<b>10.8%</b>

Table 3.4 shows the predicted performances compared with tested data. The results of head and flow predictions for pump 1 are the most accurate, followed by pump 2 and then pump 3. The errors of prediction for pump 1 are within 1%, and the errors for pump 2 are within 5%. For pump 4, the predicted flow rate is 7% larger than tested and the predicted head is 5.19% larger. If errors a little larger than 5% are considered acceptable, the prediction for

pump 4 is still relatively accurate. Unfortunately, for pump 3 the flow rate is 10% less than expected and the estimated head is 7.8% lower than the tested value. The results for pump 3 are a little disappointing due to the excessive error (much greater than 5%).

The reason why prediction errors for pump 3 are high is pump 3's inaccurately anticipated specific diameter, although it is only 3% larger than the real one. 3% error is substantially amplified due to the predicted specific diameter being squared in Equation 3-25 and cubed in Equation 3-26. A 2% error in specific diameter could yield a 5% error in flow rate. The cause of the large error in specific diameter of pump 3 is that pump 3 is of different design from the other three pumps. These four pumps were deliberately selected with the following requirements:

1. Used pumps must cover a good representative specific speed range.
2. Pumps must belong to a family of pumps designed under similar criterion.
3. Pumps must be well designed using similar state of the art technology
4. Pumps must have similar geometrical configurations in terms of inlet-impeller-diffuser-volute.

However, pump 3 was modified to optimize its off-design performances. Pump 3, therefore, no longer satisfies the above requirements.

By analyzing the results, it is concluded that the prediction method involving specific diameter would be very precise for the pumps that meet the requirements proposed above. This also indicates that the proposed method may exclude pumps of different designs hence any series of designed pumps should have their own fitting curve for higher accuracy.

### 3.3.3. Comparison with previous methods

The proposed prediction method is also compared with the previous methods. The methods of Gulich, Ventrone and Jain, however, are not compared, because these methods require detailed geometries that are not available. Figure 3.20 (a), (b), (c) and (d) show the error distribution of the prediction for the four pumps. The figures only display the predictions that have errors less than 80%. The x-axis is the error in head and y-axis is the error in flow rate. There are four circles in each figure representing 5%, 10%, 20% and 40% integrated error, which is defined as:

$$\Delta = \sqrt{\Delta H^2 + \Delta Q^2} \leq 5\%, 10\%, 20\%, 40\%, \quad (3-28)$$

where  $\Delta H$  and  $\Delta Q$  are errors of head and flow rate (%), respectively.

In Figure 3.20 (a), the head and flow are precisely predicted while all other methods have errors above 10%. The error of Stepanoff's method is outside of 10% circle and Sharma's method has an error around 20%. The methods of Yang, Frenk and Shahram have more than 40% errors. Other methods of Schmiedl, Grover, Hergt and Nautiyal are of more than 80% error, so they are not displayed in the figure.

In Figure 3.20 (b), the proposed method has error within 5%. In addition, Sharma's and Stepanoff's methods are reasonably near 5% error. This indicates that the two methods are valid near pump 2's specific speed (0.83 rad/s or 8 rpm). Yang's method yields an error near 20%. Methods of Frenk, Shahram and Schmiedl produce errors more than 40%. The results from Grover, Hergt and Nautiyal are still not present in the 80% error diagram.

In Figure 3.20 (c), the new method yields a 10% error as so Yang's method. The predictions from Stepanoff's and Sharma's are out of 20% error circle. The errors from Nautiyal

and Schmiedl are on the 40% circle. The methods from Grover, Frenk, Shahram and Hergt result in errors more than 60%.

In Figure 3.20 (d), both the new method and Yang's method provide predictions within 10% error. Therefore, Yang's method could be applicable around pump3's and pump4's specific speed (1.20 rad/s and 1.51 rad/s or 11.4 rpm and 14.5 rpm), if 10% error is considered acceptable. The predictions from methods of Schmiedl, Nautiyal, Sharma and Stepanoff all give errors larger than 20%. As to Frenk, Shahram, and hergt, their methods all yield errors more than 40%.

From all above four figures, it is found that all the previous experimental correlations are inaccurate. Since the relations according to test data are based on a limited number of pumps and pump designs, experimental correlations are usually valid only within a certain range of specific speeds for a certain pump design. As for theoretical correlations, they are not universally accurate either.

In summary, it is impossible to obtain a universally effective prediction method without detailed geometry. Therefore, more tests are required for every range of specific speed and design.

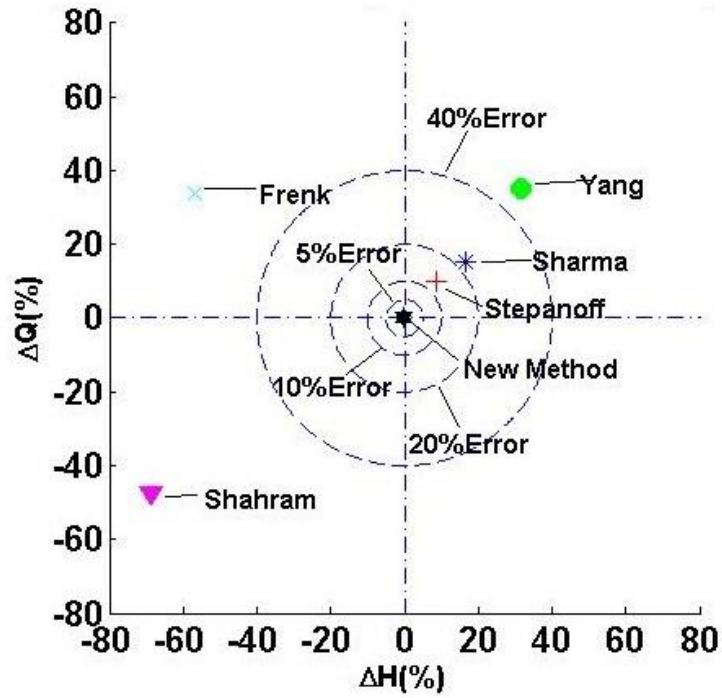


Figure 3.20a Comparison of Different Prediction Methods (pump 1)

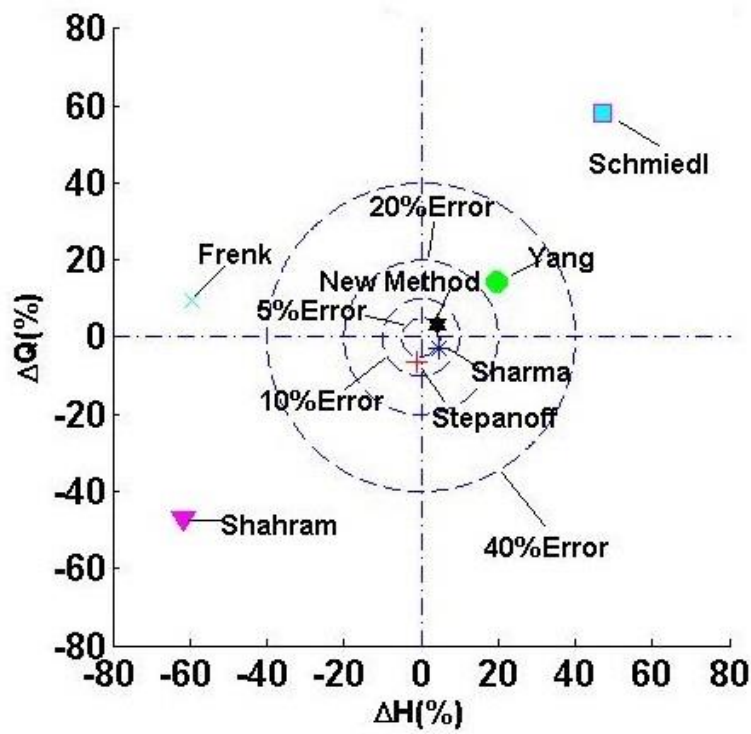


Figure 3.20b Comparison of Different Prediction Methods (pump 2)



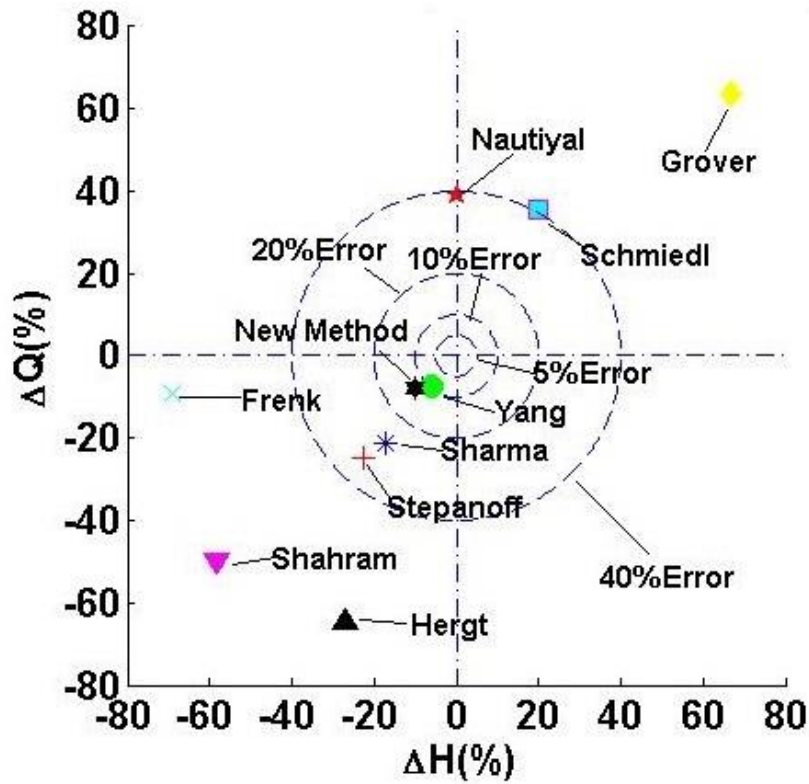


Figure 3.20c Comparison of Different Prediction Methods (pump 3)

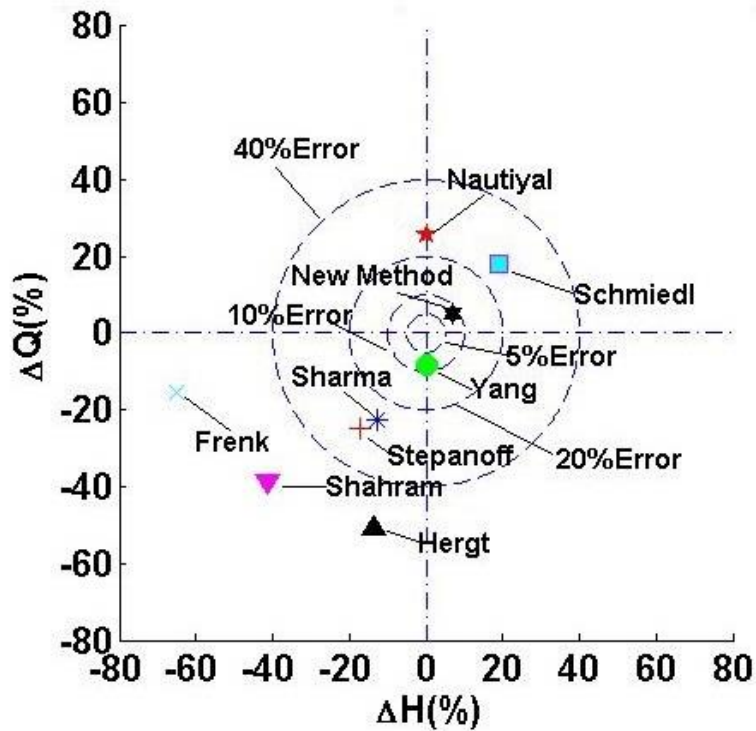


Figure 3.20d Comparison of Different Prediction Methods (pump 4)

### 3.3.4. Comparison with published experiment results

The newly proposed prediction method is also tested with other published experimental data. In Figure 3.21 and Figure 3.22, 4 more data points of specific speed and specific diameter in the two operation modes are attached. The data are acquired from the figures in Shahram Derakhshan's paper [29].

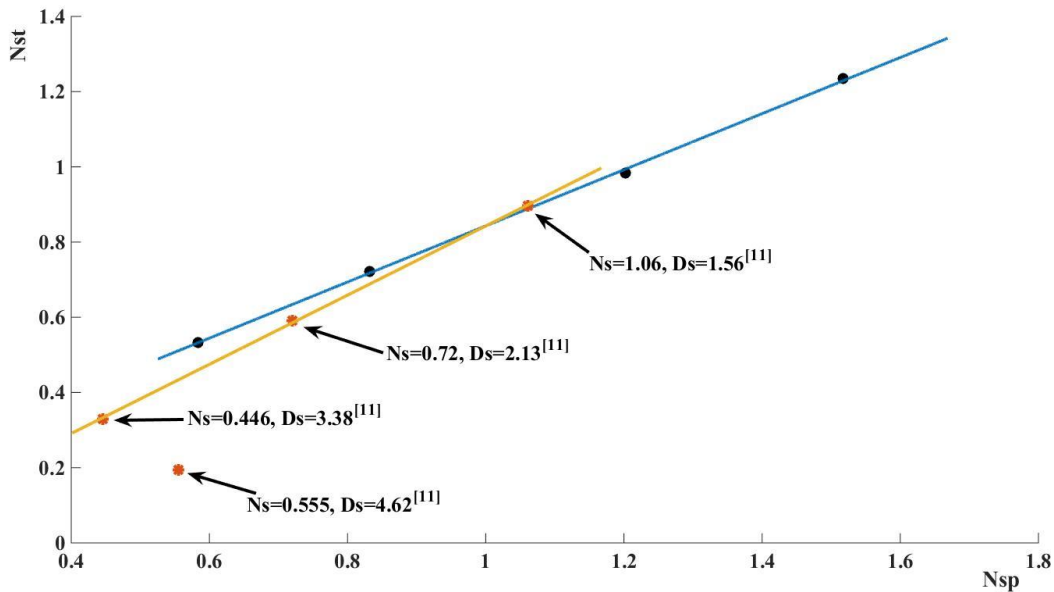


Figure 3.21 Specific Speeds between Pump Mode and Turbine Mode with extra published data

Seen from the figures, the data points of the pump with  $N_s=1.06$  and  $D_s=1.56$  are closely on the fitting line. Another pump with  $N_s=0.72$  and  $D_s=2.13$  is still near the predicting curve obtained from the testing data in this thesis. The pump with  $N_s=0.446$  and  $D_s=3.38$  and the pump with  $N_s=0.555$  and  $D_s=4.62$  are out of the range of specific speed and specific diameter in this research, and the data points of these two pumps further deviate from the fitting line as they are further out of the specific speed and specific diameter range. In addition, for the pumps with  $N_s=1.07$ ,  $N_s=0.72$  and  $N_s=0.446$ , their specific speeds and specific diameter in the

two running modes can also approximated generate a straight fitting curve. These phenomena at the same time verify the idea of the prediction method involving the specific speed and specific diameter together. However, this prediction method obtain from testing data should be completed with more tests on every range of specific speed and design.

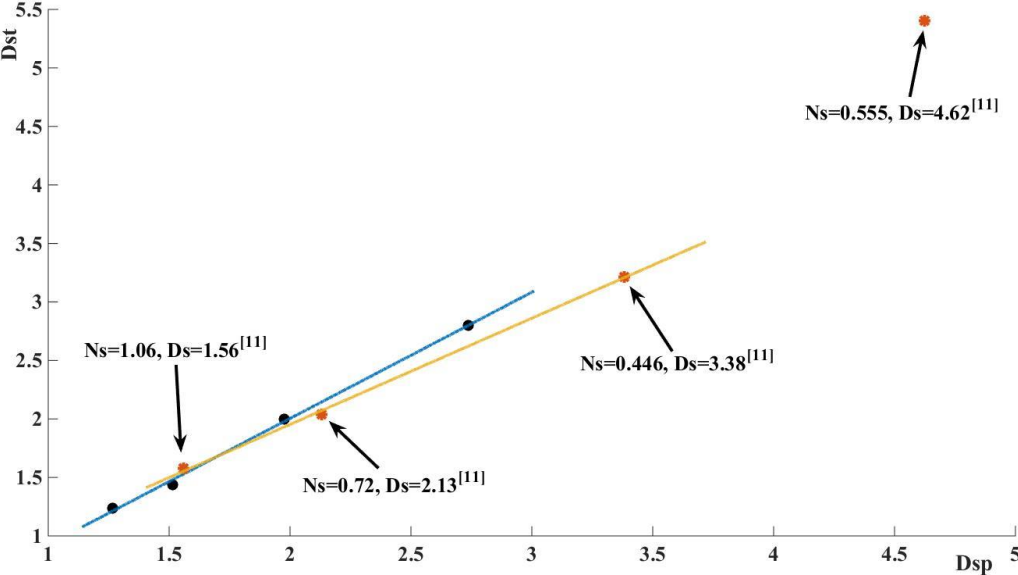


Figure 3.22 Specific Diameters between Pump Mode and Turbine Mode with extra published data

Table 3.5 presents the predicted performances using the curve proposed in this thesis and the comparisons with the published data.

As shown in Table 3.5, the errors of prediction for the first pump are about 8%. However, the errors rapidly increase for the pumps with larger specific speed. This is not surprising because their specific speed and specific diameter are scattered away from the fitting curve proposed in this thesis.

Table 3.5 Prediction results based on published data

		$N_{st}$	$D_{st}$	$H_{bt}$ (m)	$Q_{bt}$ (m <sup>3</sup> /s)	$\eta_{bt}$
$N_{sp}=1.06, D_{sp}=1.56$ <sup>[29]</sup>	Tested data	0.8967	1.5757	25.1799	0.1263	0.7841
	Predicted results	0.8864	1.5317	27.2428	0.1366	0.8322
	Error	<b>-1.14%</b>	<b>-2.8%</b>	<b>8.19%</b>	<b>8.15%</b>	<b>6.13%</b>
$N_{sp}=0.72, D_{sp}=2.13$ <sup>[29]</sup>	Tested data	0.5907	2.0412	34.5758	0.0882	0.7477
	Predicted results	0.6295	2.1439	27.5693	0.0805	0.8910
	Error	<b>6.57%</b>	<b>5.03%</b>	<b>-20.26%</b>	<b>-8.69%</b>	<b>19.17%</b>
$N_{sp}=0.446, D_{sp}=3.38$ <sup>[29]</sup>	Tested data	0.3301	3.2164	44.5820	0.0403	0.7226
	Predicted results	0.4238	3.4831	23.0488	0.0382	0.8370
	Error	<b>28.36%</b>	<b>8.29%</b>	<b>-48.30%</b>	<b>-5.28%</b>	<b>15.82%</b>
$N_{sp}=0.555, D_{sp}=4.62$ <sup>[29]</sup>	Tested data	0.1946	5.4003	45.5181	0.0145	0.6401
	Predicted results	0.5056	4.8139	8.4778	0.2005	0.7003
	Error	<b>159.8%</b>	<b>-10.86%</b>	<b>-81.37%</b>	<b>1286.6%</b>	<b>9.40%</b>

### 3.4. Summary

Four pumps are tested in their pump operation mode and turbine mode. Their best efficiency performances, specific speed and specific diameter are obtained from the testing data. This research innovatively proposed a prediction method that is based on specific speed and specific diameter. The new method is obtained by curve fitting the specific speeds, specific diameters and efficiency ratios in the pump mode and turbine mode. The fitting curves are then able to predict performances of other pumps in their turbine modes.

As a result, the relation between the specific speeds in pump mode and turbine mode are approximately linear. For specific diameters in two modes, the correlation tends to be linear. However, pump 3's specific diameter deviates a little bit (3.27%) from the straight fitting curve, because its design is different from the other three pumps. Nevertheless, a small error in specific diameter can result in a much larger error in head and flow prediction. The best way to minimize the error for the method proposed in this thesis is creating specific speed and specific

diameter correlations for each family of pumps that meet the requirements proposed in the previous sections. This will require a lot of future tests and experiments.

The ratio between the efficiencies of two running modes increases with the pump's specific speed in a roughly linear trend. The errors of efficiency prediction are smaller than 5%.

With predicted specific speed and diameter, the head and flow in turbine mode can be estimated. The errors of prediction results for pump 1 are smaller than 1%. The pump 2's prediction errors of head and flow are 3% and 4%, and pump 4's errors are near acceptable 5% limits. However, pump 3's errors are nearly 10% because it is geometrically modified, thus it does not meet the requirements in Section 3.3.2. Therefore, the new method based on specific speed and specific diameter may be exclusive, which means it could be inaccurate for a different pump design. Hence, future tests for different types of pumps are required.

This chapter also compares the new method with 9 previously published prediction methods. Most previous methods are not accurate for the four tested pumps (at least 20% error). All of the previous experimental correlations are invalid. However, Stepanoff's and Sharma's methods are valid near specific speed of 0.83 rad/s (near 5% error). Yang's method is acceptable around a specific speed range between 1.20 rad/s and 1.51 rad/s. The results clearly reveal that all the prediction methods (without detailed geometry) are only valid conditionally. Special prediction equations should be obtained for each range of specific speed and each type of pump design from testing data.

In addition to comparison with previous prediction methods, the new method is also tested with published experimental data. Data from the four pumps are applied on the prediction methods. The errors for the pump with  $N_{sp}=1.06$  and  $D_{sp}=1.56$  are about 8% because

the specific speed and specific diameter are very close to the prediction curve proposed in this thesis. The prediction results for the other three pumps have enormous errors. This is not surprising because their specific speed and specific diameter are scattered away from the fitting curve proposed in this thesis. The inaccuracy at the same time verifies the necessity of more tests on other families of pumps with different ranges of specific speed and specific diameters.

## CHAPTER 4. BIO-SOLAR HYBRID SYSTEM

### 4.1. Concept of the Bio-solar Hybrid System

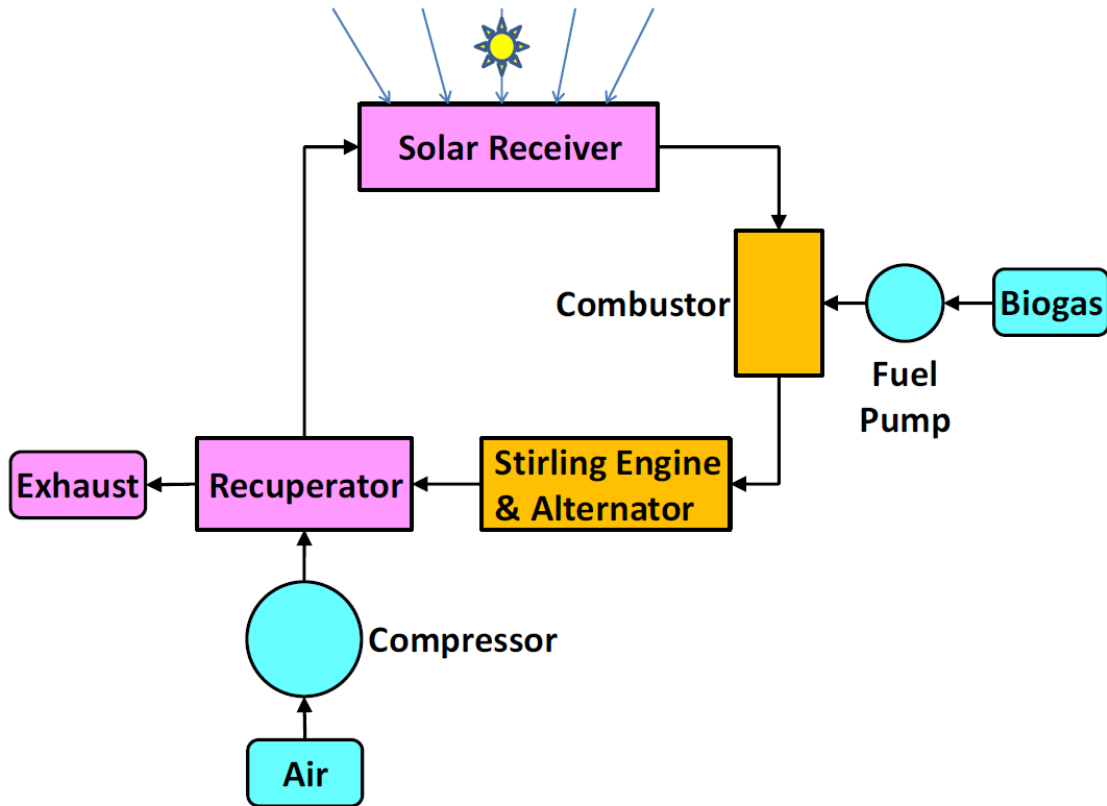


Figure 4.1 Concept of the System

There is great interest to develop power for electricity, desalination plants, irrigation and general pumping using a hybrid Solar-Biogas energy source. But prior to that, an appropriate energy cycle has to be developed and investigated. The schematic of the system is shown in Figure 4.1. Thermodynamically the system is based on recuperative Brayton Cycle. The air, as the working fluid, is compressed in the compressor at the beginning. Then, the air is heated twice by the exhaust in the recuperator and solar energy in the solar receiver. In next

step, the air is combusted with biogas in the combustor. At last the hot and compressed mixture of gases enters the engine producing work and the exhaust in return heats the cold air.

To verify one possible concept for such hybrid Solar-biogas energy source, a model gas cycle will be developed and tested. Shown as in Figure 4.2, an electric gas heater is used to substitute the solar receiver. An Inflow radial turbine, as the engine, is designed and tested.

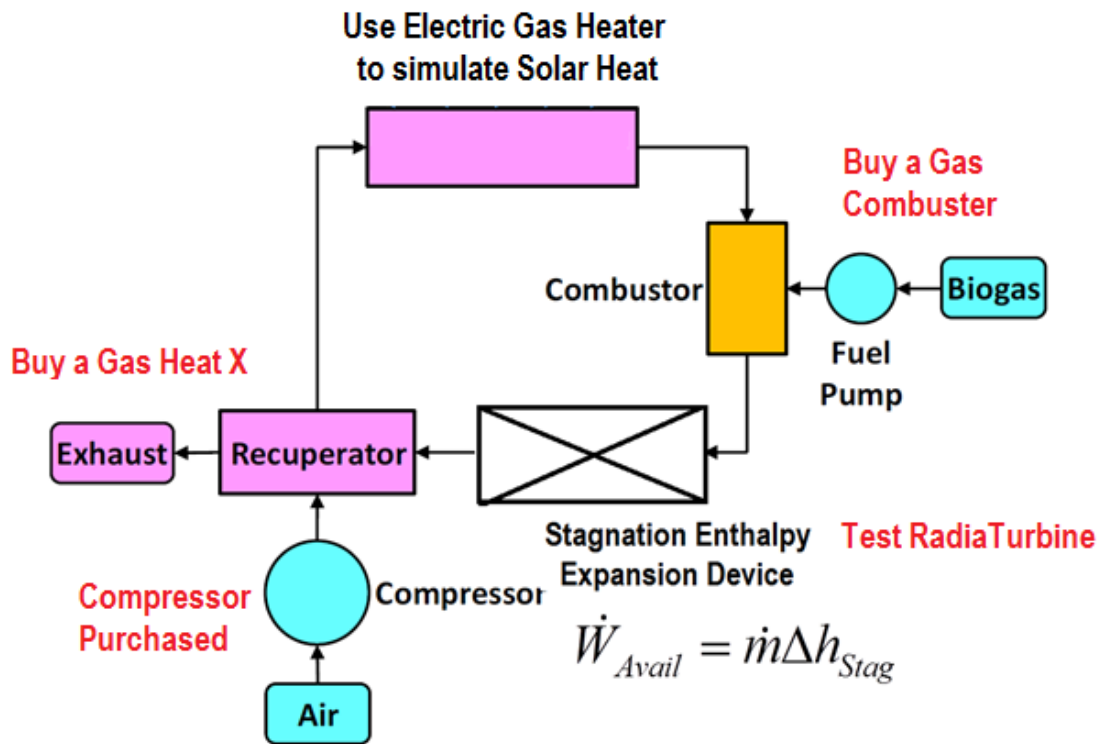


Figure 4.2 Model of the System

## 4.2. Design and Construction of the system

### 4.2.1. Design of the system

The thermal fluid cycle is designed in the environment of commercial chemical process analysis software Aspen Plus. In Aspen Plus, the scheme of the system is presented as Figure

4.3.



In Figure 4.3, Block 1 (B1) is the compressor, B2 is the combustor, B3 is the turbine, B4 is the recuperator, and B5 is the solar receiver.

The design of the system is based on the characteristics of the compressor that purchased at first. Figure 4.4 is the performance chart of the compressor.

Considering the efficiency and pressure ratio of the compressor, the working point is chosen at flow rate 100lb/min (0.756kg/s) and pressure ratio 1.575. The efficiency at this point is 78%.

After finding the running point of the compressor, the second step is setting the combustion temperature, and 900°C is expected. The fuel in the combustor is methane.

In the analysis, the isentropic efficiency of the turbine is presumed to be 80% besides 99% mechanical efficiency.

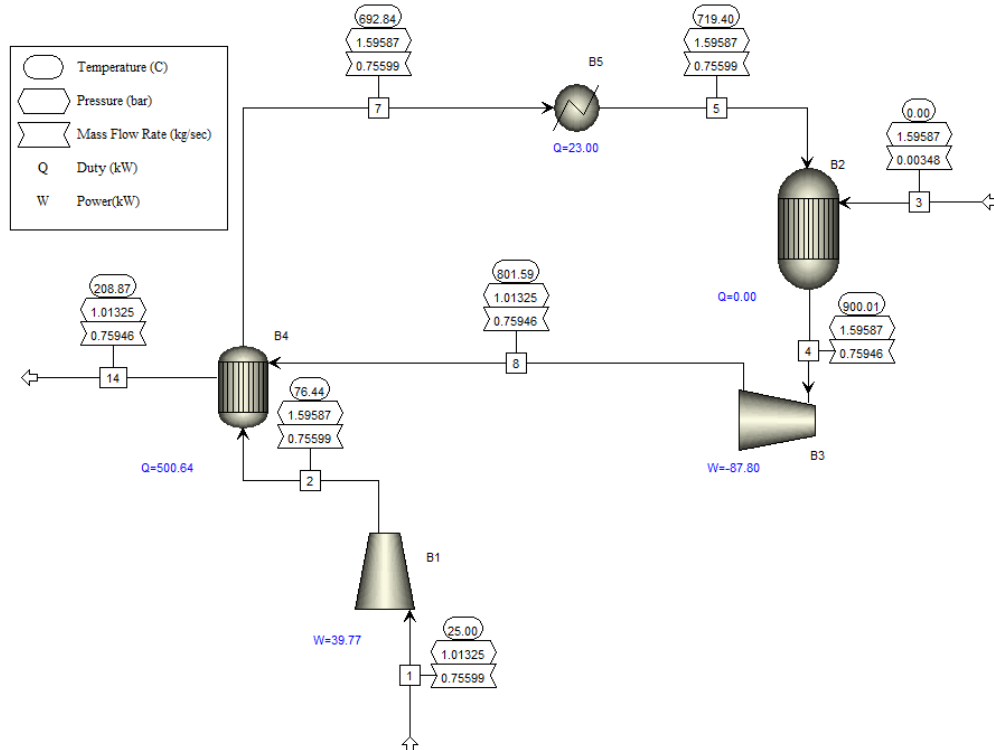


Figure 4.3 The scheme and calculation results of the system

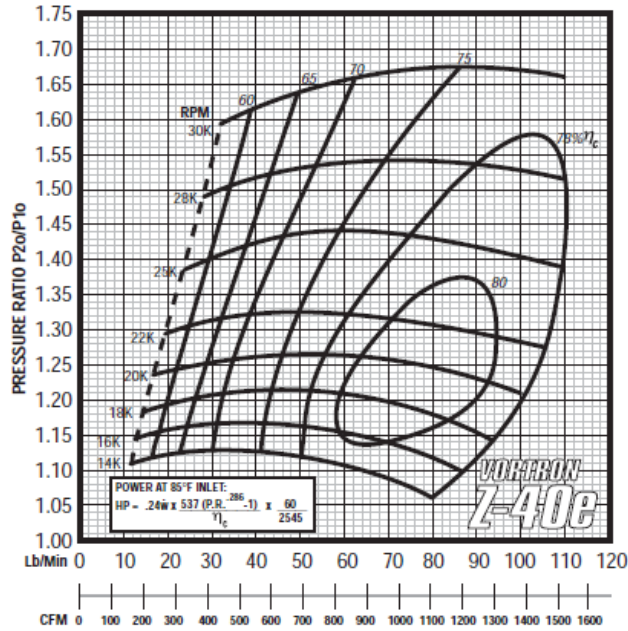


Figure 4.4 Characteristics map of the compressor

The heater is assumed ideally 0 pressure drop, and the heat duty is set 23kw considering the heater available on market.

At last, the heat recover rate of the recuperator is:

$$\eta_r = \frac{T_7 - T_2}{T_8 - T_2} = 0.85 \quad (4-1)$$

With all the above settings, the calculation results of all the streams and blocks are shown in Figure 4.3.

The heat inputs are the ones into the heater and into the combustor. Then, the thermal efficiency of the system is:

$$\eta_{thermal} = \frac{(h_4 - h_8) - (h_2 - h_1)}{(h_5 - h_7) + (h_4 - h_5)} \times 100\% = 20.1\% \quad (4-2)$$

However, if the consumed fuel is solely considered energy cost, while the heat received in the heater is “free” from sun, the efficiency of the system is:

$$\eta_f = \frac{(h_4 - h_8) - (h_2 - h_1)}{h_4 - h_5} \times 100\% = 23\% \quad (4-3)$$

As the energy is treated as free, it is not difficult to conclude that the more solar energy is received into the system, the higher will the efficiency be.

The theoretical results indicate the solar-biogas energy system could be practical. However, further experimental studies are essential to validate its feasibility.

#### **4.2.2. The setup of the system**

Figure 4.5 is the 3D model of the system as the blueprint of the structure of the system. Components including the compressor, the gas heater and the burner have been bought and set up, as shown in Figure 4.6.

Part 1 is the compressor bought from VOTRON<sup>®</sup>, its characteristics have been introduced in the former section. Part two is an electrical gas heater that simulates as a solar receiver in the solar-biogas hybrid system. Choosing from the catalog of WATLOW<sup>®</sup>, a gas heater capable of producing 23 kW heat with a 100lb/min (0.756kg/s) mass flow rate of air is chosen.

Part three is the burner bought from ECLIPSE<sup>®</sup>, which is able to reheat the hot air to 900 °C at 1.575atm.

Space has been reserved for the recuperator to be installed in the future and the turbine to be designed and tested.

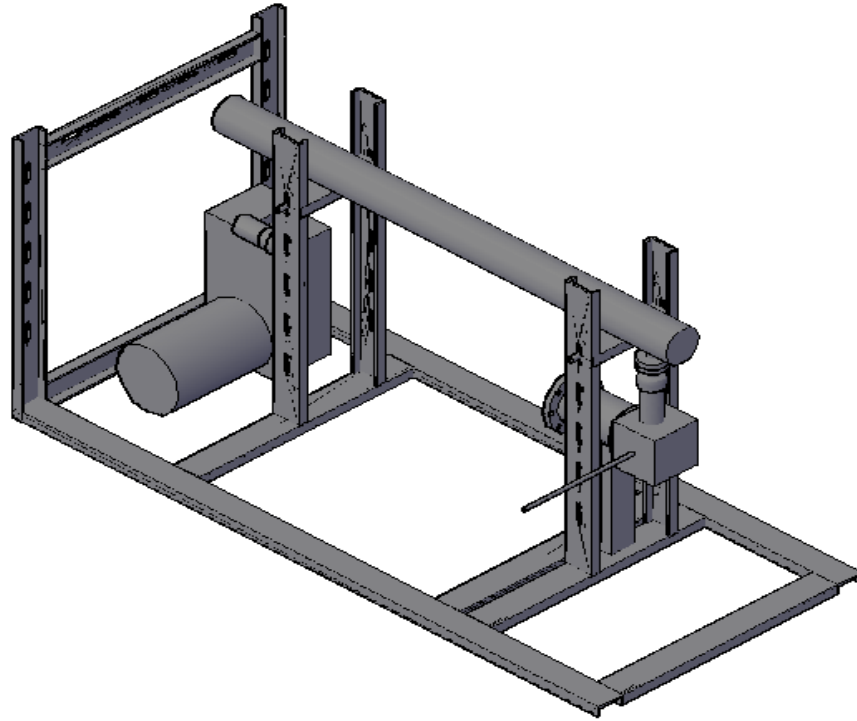


Figure 4.5 3D model of the system

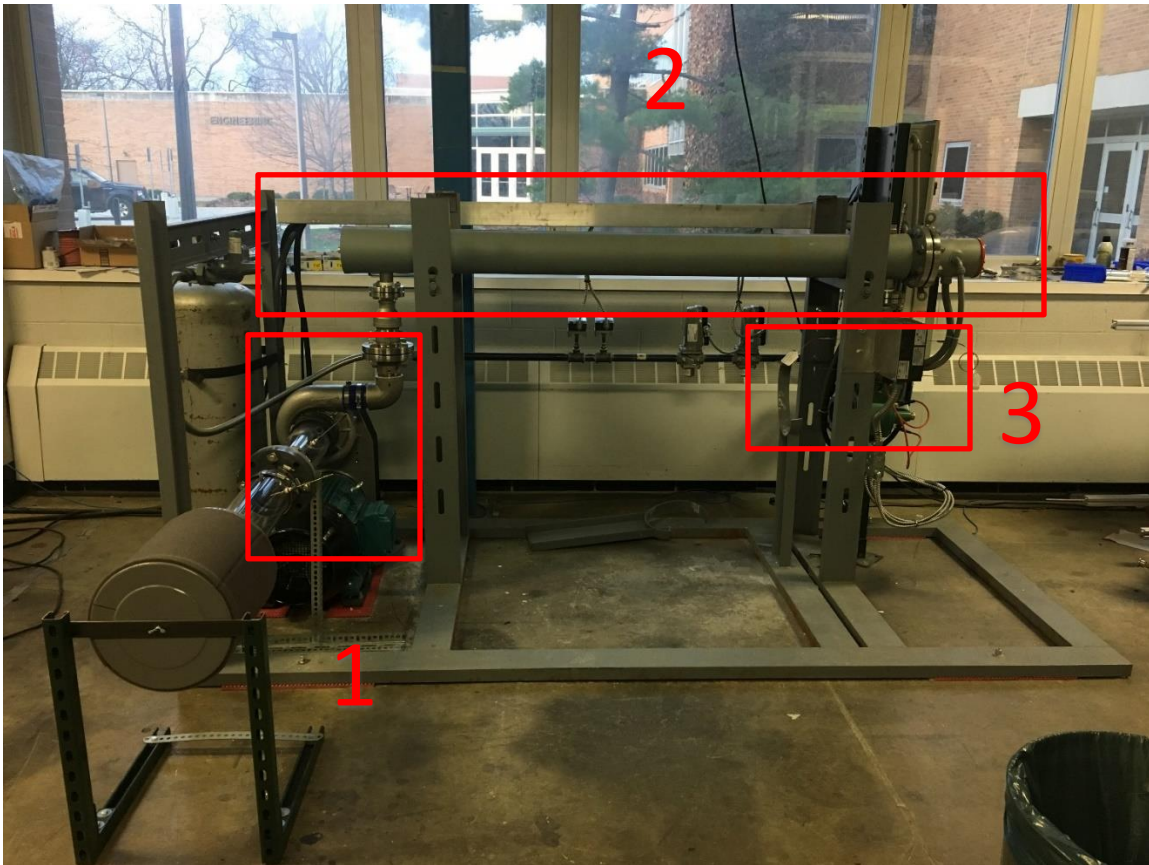


Figure 4.6 The actual setup of the system

### 4.2.3. System without recuperator

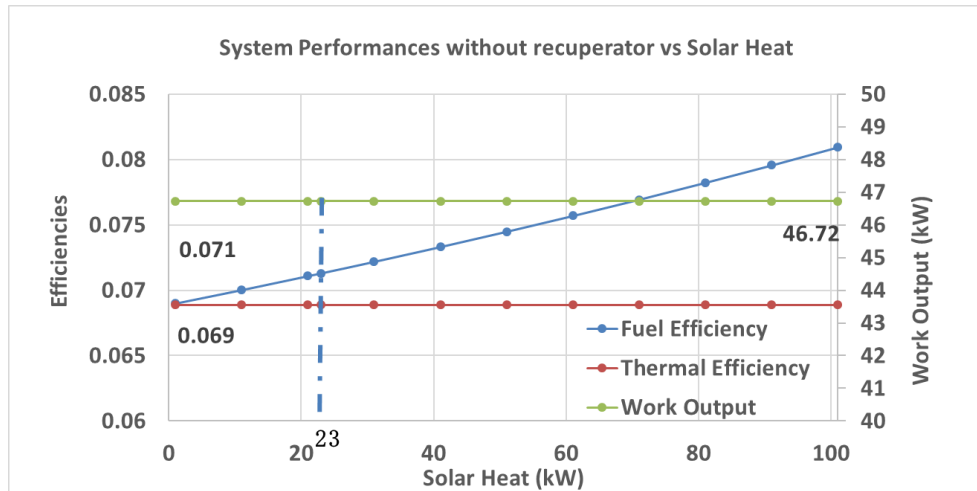


Figure 4.7 System Performances vs Solar Heat without Recuperator

As shown in Figure 4.7, it can be expected the heat from the Solar Receiver does not influence the thermal efficiency. The more heat the solar receiver contributes to the system, the less fuel is needed, so that the fuel efficiency increases.

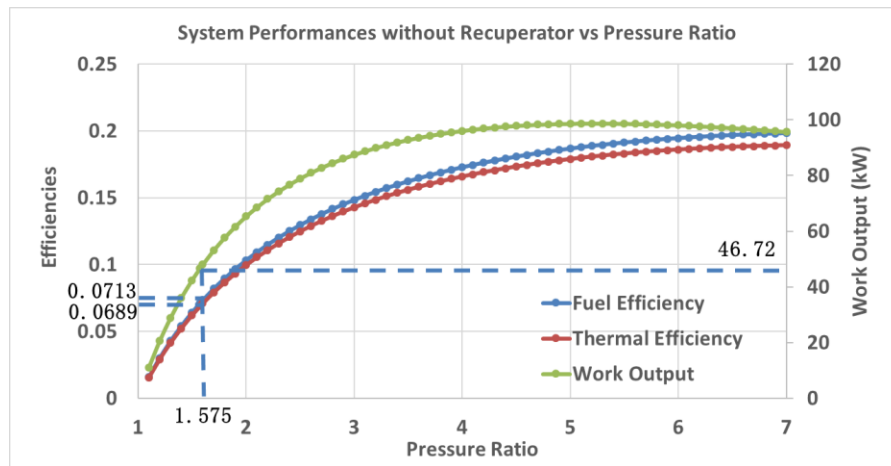


Figure 4.8 System Performances vs Pressure Ratio without Recuperator

As the pressure ratio increases in Figure 4.8, the fuel efficiency and thermal efficiency go up as well. The work output reaches its peak when pressure ratio is around 5. However, the

pressure ratio of the system is initially set to be 1.575, and the fuel efficiency and thermal efficiency are as low as 0.0713 and 0.0689 respectively.

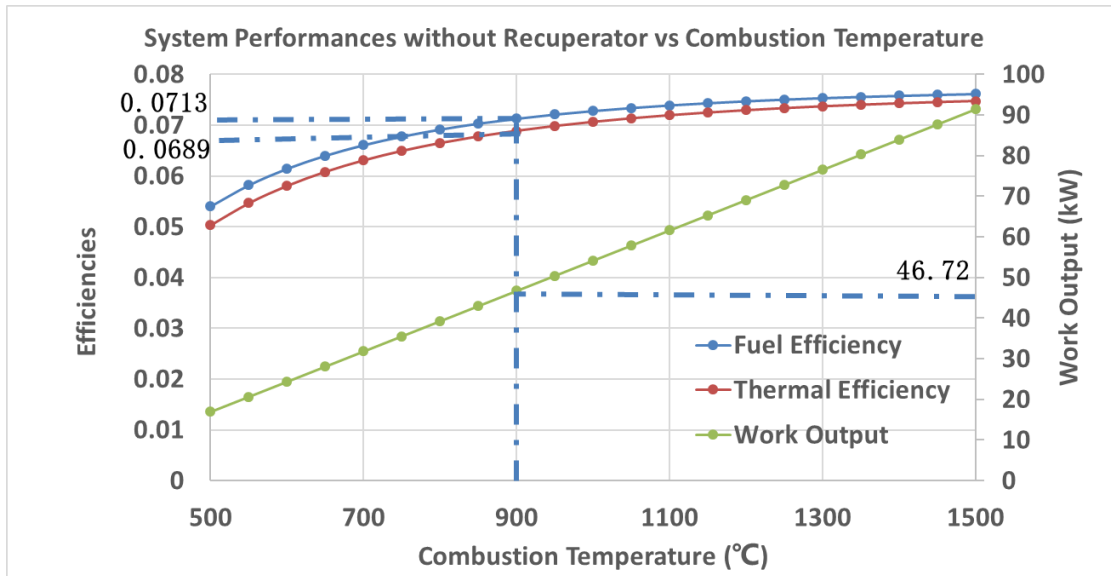


Figure 4.9 System Performances vs Combustion Temperature without Recuperator

The work output, the fuel efficiency and the thermal efficiency all increases as the combustion temperature in the burner rises. The combustion temperature is expected to be 900°C for the system.

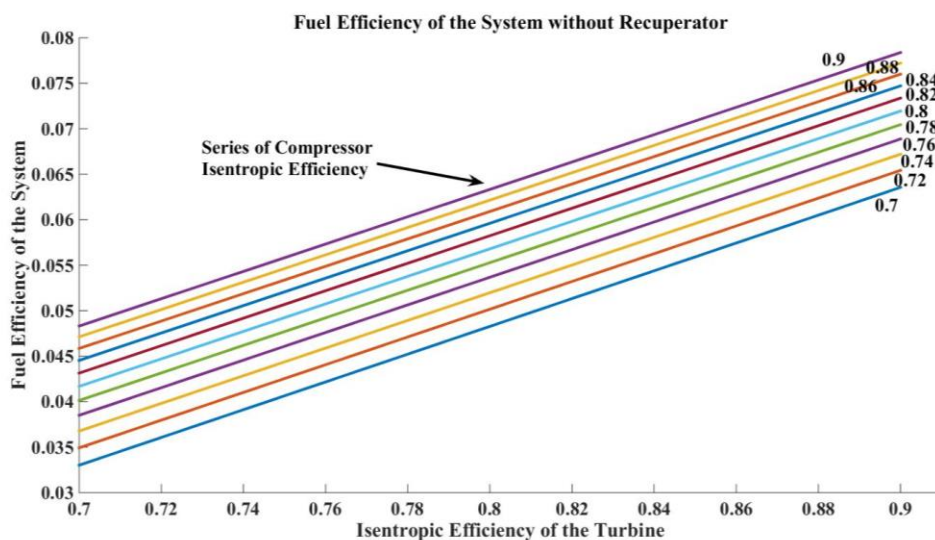


Figure 4.10 Fuel Efficiency Changes with Isentropic Efficiencies of the Turbine and Compressor without Recuperator

Figure 4.10 shows the fuel efficiency of the system with different turbine and compressor isentropic efficiencies ranging from 0.7 to 0.9. The fuel efficiency apparently increasing with higher compressor or/and turbine efficiency. However, the fuel efficiency only improves a few percentages as the isentropic efficiencies of the turbine and compressor rise from 0.7 to 0.9.

In general, The open cycle system runs with 1.575 pressure ratio, 23kW gas heater, and 900°C combustion temperature. The Fuel efficiency is 0.0713 and thermal efficiency is 0.0689. The work output is 46.72 kW.

Table 4.1 is the fuel consumptions for system without recuperator.

Table 4.1 Consumptions of different kinds of fuels of the system without recuperator

	Methane	Ethane	Propane
Fuel Consumption, kg/s	0.01419	0.01486	0.01521

The table can indicate the economy of the system if the prices of the fuels are known.

#### 4.2.4. System with Recuperator

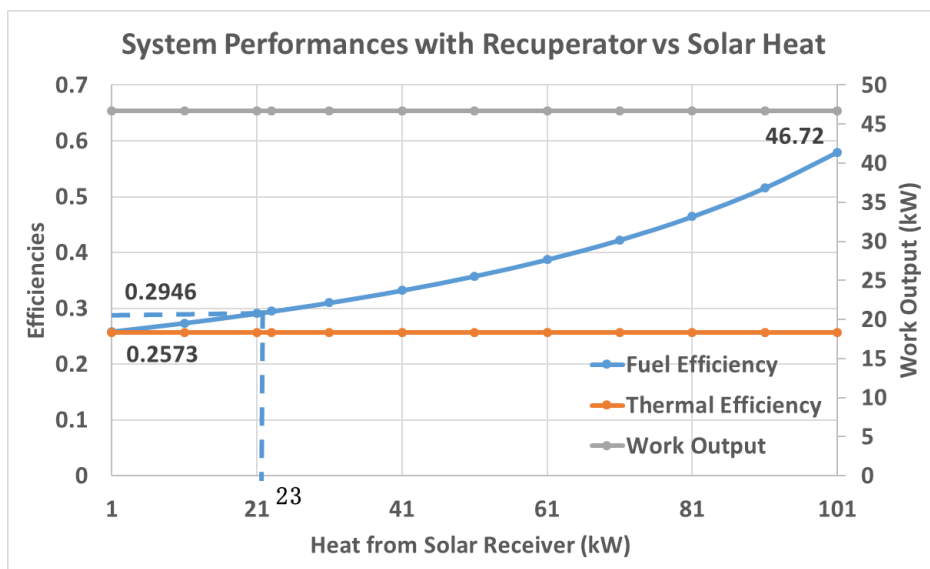


Figure 4.11 System Performances vs Solar Heat with Recuperator

Seen from Figure 4.11, the heat from Solar Receiver does not influence the thermal efficiency. The more heat the solar receiver contributes to the system, the less fuel is needed, so that the fuel efficiency increases.

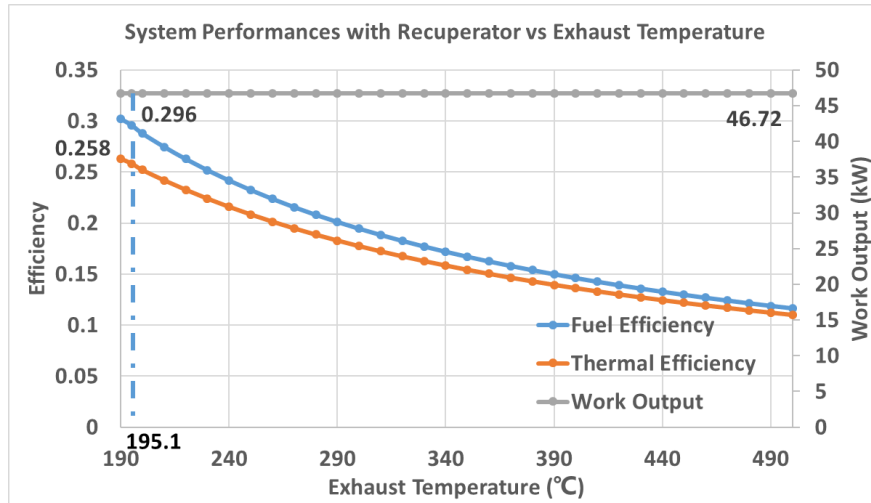


Figure 4.12 System Performances vs exhaust temperature with recuperator

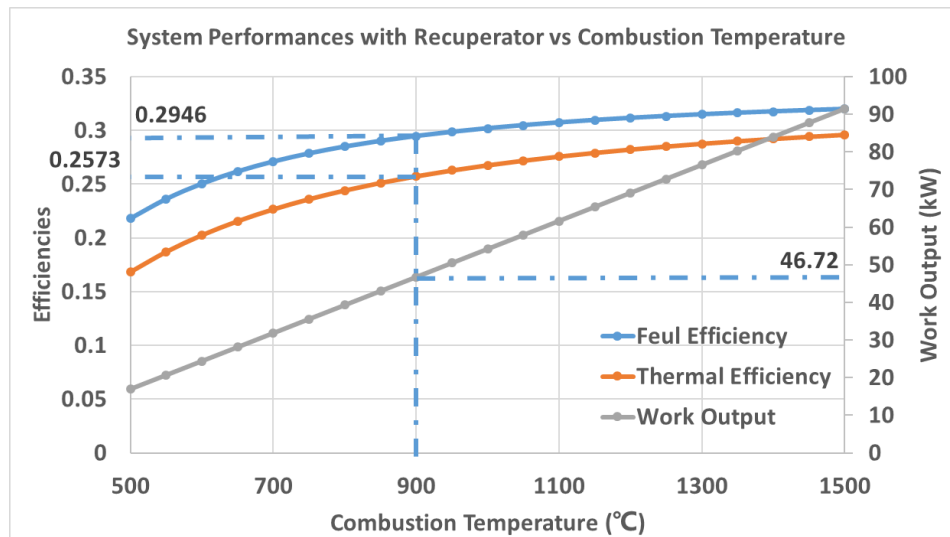


Figure 4.13 System performances vs Combustion Temperature with recuperator

A higher exhaust temperature means less heat is recovered by the recuperator, so the fuel efficiency and the thermal efficiency decrease. However, the work output stays same as



exhaust temperature rises, because the inlet temperature of either the compressor or turbine does not change.

Fuel efficiency, thermal efficiency and work output all increase as combustion temperature goes up. The combustion temperature in this system is initially set at 900°C.

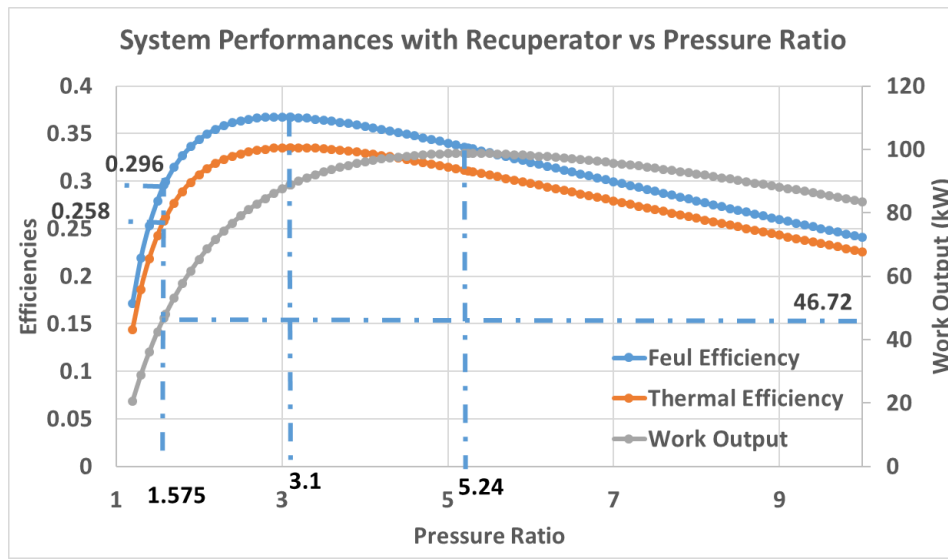


Figure 4.14 System Performances vs Pressure Ratio with recuperator

In Figure 4.14, the system will reach its maximum fuel efficiency and thermal efficiency at the pressure ratio of 3.1, and the maximum work output is obtained at the pressure ratio of 5.24. However, the system approximately runs with a pressure ratio of 1.575.

Figure 4.15 shows the fuel efficiency of the system without different turbine and compressor isentropic efficiencies ranging from 0.7 to 0.9. Rising from 0.7 to 0.9, the improvement of compressor and turbine can increase the fuel efficiency from 0.21 to 0.41 for the system with recuperator. Comparison to the system without recuperator, the recuperator is very advantageous. The recuperator not only significantly improves the efficiencies of the system, but it also amplifies the benefits from increasing the isentropic efficiencies of the compressor and the turbine.

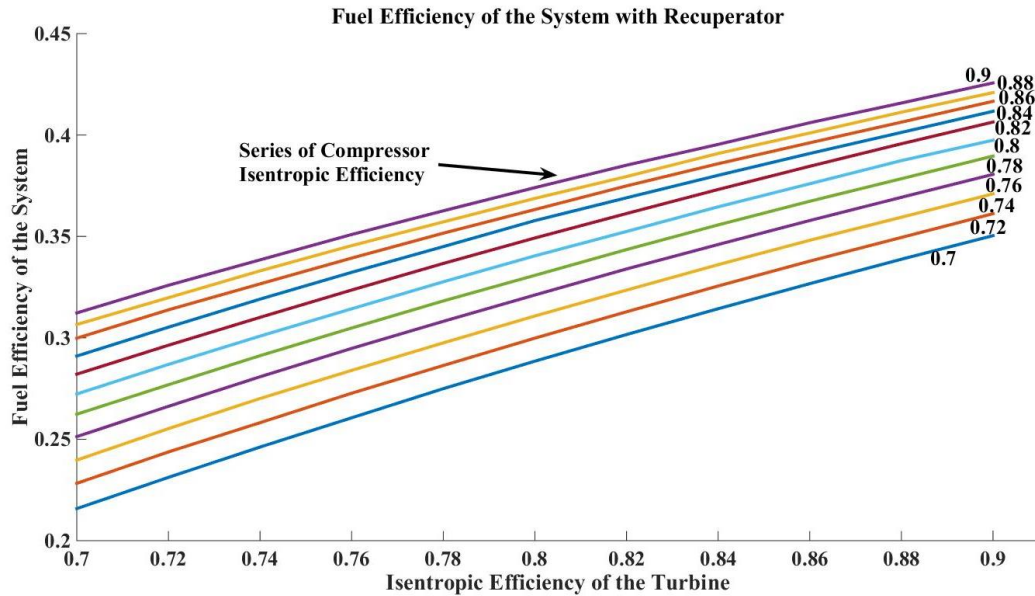


Figure 4.15 Fuel efficiency changes with isentropic efficiency of the turbine and compressor with recuperator

In summary, the system operates with 1.575 pressure ratio, 900 °C combustion temperature, 23 kW gas heater and 195.1°C exhaust temperature after recuperator. Then, the fuel efficiency is 0.296, the thermal efficiency is 0.258 and work output is 46.72 kW.

Table 4.2 is the fuel consumptions of different kinds of fuels.

Table 4.2 Consumptions of different kinds of fuels of the system with recuperator

	Methane	Ethane	Propane
Fuel Consumption, kg/s	0.002551	0.002784	0.002744

Because the efficiency of the system is much higher with recuperator, the fuel consumptions are much less than the system without recuperator.

### 4.3. Summary

The theoretical analyses of the systems with and without recuperator conclude that higher efficiencies of the compressor and turbine will improve efficiencies of the system. The

recuperator significantly increases the performances of the system and amplifies the benefits from the improvements of the compressor and the turbine. At last, the design point for the turbine is estimated as shown in Table 4.3.

Table 4.3 Design Specification of the Turbine

Mass Flow	Inlet Temperature	Inlet Pressure
100lb/min, 0.756kg/s	900 °C	1.57atm

## CHAPTER 5. DESIGN AND ANALYSIS OF IFR TURBINE

The objective of this chapter is to design a radial gas turbine rotor. 1-D and 3-D geometry is generated based on Aungier's method. 1-D loss model analysis and 3-D CFD simulations are performed to examine the performances of the rotor.

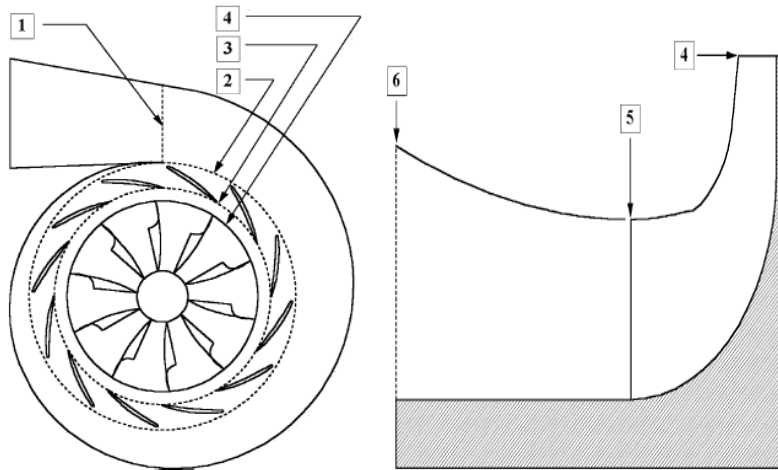


Figure 5.1 Position numbers designated to radial turbine components

The stations that are used in the design process as presented in Fig. 1.10 in the first chapter.

As shown in Figure 5.1, the components of a radial inflow turbine typically consist of volute (1-2), inlet nozzle (2-3), rotor (4-5) and diffuser (5-6). The outlet of nozzle and inlet of rotor are two different stations because the vaneless gap between the two parts is large enough for the flow to change its velocity and angle. This chapter focuses on design and analysis for the rotor (4-5).

Table 5.1 Specifications for the turbine

$\dot{m}_{air}$ (kg/s)	$T_{it}$ (K)	$P_{it}$ (atm)	$P_{et}$ (atm)
0.756	1173.15	1.575	1.02

The outlet pressure is 1.02atm, because the outlet is going to be connected to a recuperator.

The design process generally involves 1D design, 1D performance analysis, Quasi-3D design and 3D analysis. The scheme of the process is shown in Figure 5.1.

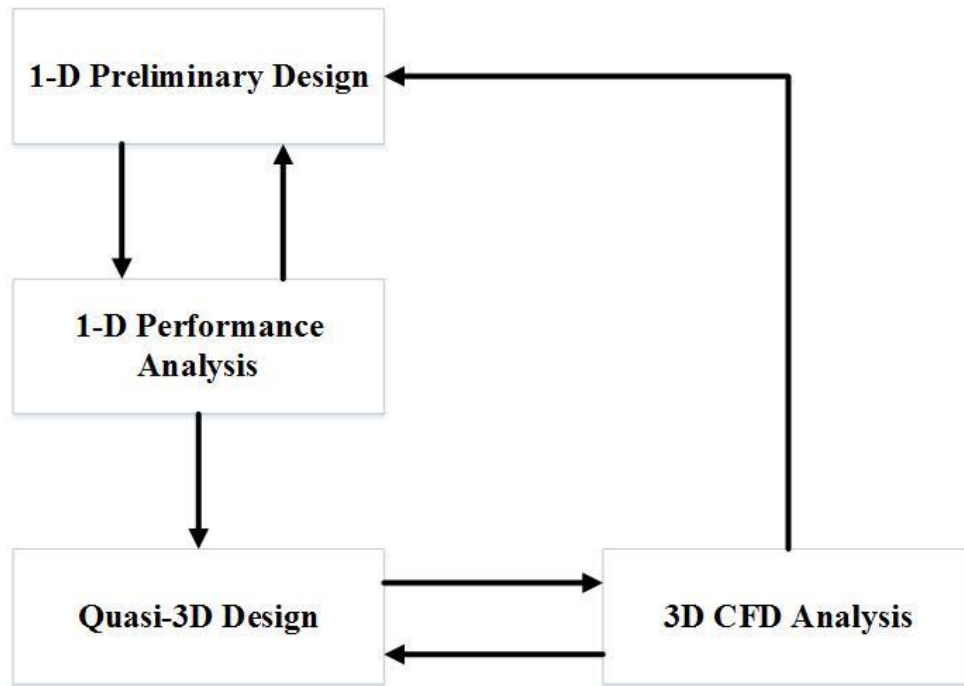


Figure 5.2 Scheme of the design process

Once 1D preliminary design is initially finished, it can be evaluated by 1D performance analysis. 1D design then will be adjusted and refined to better meet the expected specifications, and 1D design can be optimized for the best performance based on the given design constraints.

With 1D optimization, the design comes to the stage of Quasi-3D design. Quasi-3D design specifies the blade shape, imposes structural restrictions, and specifies channel shape. Then, 3D model can be established. 3D analysis now can be performed on the 3D model to study its aerodynamic performances and structural reliability. The results of 3D analysis will

help optimize Quasi-3D design. If necessary, 1D design may have to be changed to achieve better performances in 3D analysis.

The 1D and quasi-3D design procedures are based on the methods proposed by Aungier and Rolick<sup>[4]</sup>. The 3D analysis will be performed by ANSYS CFX.

## 5.1. 1D Preliminary Design

### 5.1.1. Thermodynamics properties of the working fluid

The actual mass flow that enters the turbine consists of the air and production of combustion of the fuel and the air. Ideally the components of mass flow are O<sub>2</sub>, N<sub>2</sub>, CO<sub>2</sub>, and H<sub>2</sub>O. All the gases are considered as ideal gases, and only the thermodynamics properties of the mixture are needed in the 1D design processes. The molecular weight can be calculated as:

$$M_{mix} = \sum \text{Mole Fraction} \times \text{Molecular Weight (Component)} \quad (5-1)$$

Therefore,

$$R = \frac{\bar{R}(8.314 \frac{kJ}{kmol.K})}{M_{mix}} \quad (5-2)$$

The specific heat (C<sub>p</sub>) of the mixture is based on the text book by Michael Moran 4<sup>th</sup> edition<sup>[1]</sup>.

$$\frac{\bar{c}_p}{\bar{R}}(CO_2) = 2.401 + 8.735e^{-3}T - 6.607e^{-6}T^2 + 2.002e^{-9}T^3 \quad (5-3)$$

$$\frac{\bar{c}_p}{\bar{R}}(O_2) = 3.626 - 1.878e^{-3}T + 7.055e^{-6}T^2 - 6.764e^{-9}T^3 + 2.156e^{-12}T^4 \quad (5-4)$$

$$\frac{\bar{c}_p}{\bar{R}}(N_2) = 3.675 - 1.208e^{-3}T + 2.324e^{-6}T^2 - 0.632e^{-9}T^3 - 0.226e^{-12}T^4 \quad (5-5)$$

$$\frac{\bar{c}_p}{\bar{R}}(H_2O) = 4.070 - 1.108e^{-3}T + 4.152e^{-6}T^2 - 2.964e^{-9}T^3 + 0.807e^{-12}T^4 \quad (5-6)$$

So,

$$C_p(\text{Mixture}) = \left[ \sum \frac{\bar{C}_p}{\bar{R}} (\text{Component}) \times \text{Mole Fraction} \right] \times \bar{R} / M_{\text{mix}} \quad (5-7)$$

$$k(\text{Mixture}) = C_p(\text{Mixture}) / (C_p(\text{Mixture}) - R) \quad (5-8)$$

Table 5.2 is the results of applying the above equations to the different mixtures of gases.

Table 5.2 Gas components for different fuels and different systems

	O <sub>2</sub> (%)	N <sub>2</sub> (%)	CO <sub>2</sub> (%)	H <sub>2</sub> O (%)	M <sub>mix</sub> (kg/kmol)	R <sub>mix</sub> (kJ/kg·K)
Propane without recuperator	14.0483	76.9735	3.8478	5.1304	28.6734	0.289955
Ethane without recuperator	14.0029	76.8266	3.6682	5.5023	28.6057	0.290642
Methane without recuperator	13.7818	76.4197	3.2662	6.5323	28.4296	0.292442
Propane with recuperator	19.7188	78.6265	0.7092	0.9456	28.8158	0.288523
Ethane with recuperator	19.7108	78.5996	0.6759	1.0138	28.8033	0.288648
Methane with recuperator	19.6664	78.5233	0.6034	1.2069	28.7706	0.288975

For the system without recuperator, more fuels are needed to heat the air to the same temperature. Therefore, more oxygen is consumed producing more carbon-dioxide and steam. In the system with recuperator, less fuel is burned so that oxygen has higher percentage compared to the gas in the system without recuperator. For the same system but different fuels, burning propane will result in a little bit higher oxygen and carbon-dioxide. The exhaust of combustion of methane has higher percentage of steam, because lighter hydrocarbons have more hydrogen component which will produce more H<sub>2</sub>O but less CO<sub>2</sub>.

Table 5.3 presents the specific heat capacities at constant pressure and specific heat ratios of the mixture gases of different components at 900°C. According to the results, the thermodynamics properties of different mixtures of gases are very close to each other. Therefore, the mixture from the combustions between air and propane without recuperator is chosen as the working fluid.

Table 5.3 Specific heat capacities and specific heat ratios for different gases at inlet, 900°C

	C <sub>pi</sub> (kJ/kg·K)	ki
Propane without recuperator	1.2230	1.3108
Ethane without recuperator	1.2257	1.3108
Methane without recuperator	1.2335	1.3108
Propane with recuperator	1.1817	1.3230
Ethane with recuperator	1.1822	1.3230
Methane with recuperator	1.1836	1.3230

### 5.1.2. 1D preliminary design

Specific speed is most important characteristic to start the design process. Because no geometry limitation but the optimum efficiency is required for this turbine,  $N_s=0.55$  is chosen based on the correlation (1-23):

$$\eta_s = 0.87 - 1.07(N_s - 0.55)^2 - 0.5(N_s - 0.55)^3 = 0.87 \quad (1-23)$$

The definition of specific speed is already introduced in Equation 1-21:

$$N_s = \frac{\omega\sqrt{Q_5}}{(\Delta h_{ideal})^{0.75}} \quad (1-21),$$

where  $Q_5$  is flow at the rotor outlet, and  $\Delta h_{ideal}$  is estimated by:

$$\Delta h_{ideal} = C_{pi}T_{it} \left( \pi_0^{\frac{k_i}{k_i-1}} - 1 \right) \quad (5-9)$$

The isentropic exit total temperature can be obtained from



$$T_{etideal} = T_{it} \left( \frac{P_{et}}{P_{it}} \right)^{\frac{k_i-1}{k_i}} \quad (5-10).$$

The exit total temperature is then initially decided by:

$$T_{et} = T_{it} - \eta_s(T_{it} - T_{etideal}) \quad (5-11)$$

The density and flow rate of the ideal gas at the outlet then are estimated with:

$$\rho_{et} = P_{et}/(RT_{etideal}) \quad (5-12)$$

$$Q_5 = \dot{m}/\rho_{et} \quad (5-13)$$

Angular velocity is:

$$\omega = N_s(\Delta h_{ideal})^{0.75}/\sqrt{Q_5} \quad (5-14)$$

Now enough properties have been obtained to initialize the design.

$$v_s = c_{vs}N_s^{0.2} \quad (5-15),$$

In Equation 5-15 the coefficient  $c_{vs}$  starts with 0.737.  $v_s$  decides the value of tip velocity  $U_4$  in Equation 5-17 for a given discharge spouting velocity.

The discharge spouting velocity and the rotor tip blade are calculated with:

$$C_{0s} = \sqrt{2\Delta h_{ideal}} \quad (5-16)$$

$$U_4 = v_s C_{0s} \quad (5-17)$$

From specific efficiency and assume that the specific heat is constant,

$$T_{t5} = T_{it} - \eta_s(T_{t5} - T_{etideal}) \quad (5-18)$$

The exit velocity is impossible to know at this stage, therefore exit temperature  $T_{s5}$  is estimated with  $T_{t5}$  in Equation 5-18. Iterations can be performed later to obtain  $T_{s5}$ .

The rotor tip radius now is yielded from Equation 5-19.

$$r_4 = U_4/\omega \quad (5-19)$$

In nozzle stage a portion of pressure is lost which will influence the sizing of the rotor. Rotor inlet total pressure is estimated by equation 5-20<sup>[4]</sup>.

$$P_{t4} = P_{it} - \rho_{t1} \Delta h_{ideal} (1 - \eta_s) / 4 \quad (5-20)$$

Inlet tangential velocity is calculated by

$$C_{\theta 4} = U_4 \eta_s / (2v_s^2) \quad (5-21)$$

Inlet absolute flow angle is decided from empirical correlation 5-22<sup>[4]</sup>.

$$\alpha_4 = 10.8 + 14.2N_s^2 \quad (5-22)$$

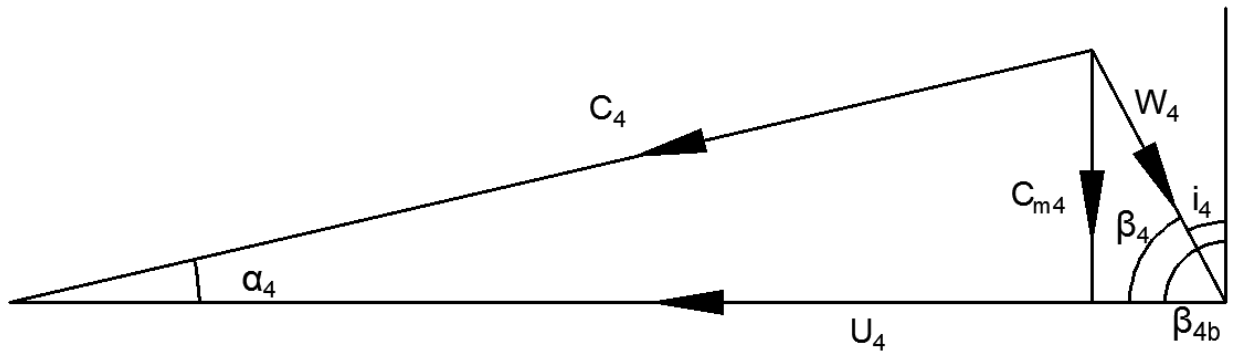


Figure 5.3 Inlet velocity triangle of rotor

With rotor tip velocity, absolute flow angle, and tangential velocity component, all the other velocities and angles can be calculated.

$$C_{m4} = C_{\theta 4} \tan \alpha_4 \quad (5-23)$$

Recommended by Aungier<sup>[4]</sup>, inlet relative flow angle  $\beta_4$  should be around  $70^\circ$ . If the inlet relative velocity is too large, increase  $c_{vs}$  to obtain a good inlet flow angle.

$$b_4 = \dot{m} / (\rho_4 2\pi r_4 C_{m4}) \quad (5-24)$$

Then, inlet width of passage can be calculated from mass flow balance.

The blade thicknesses and hub radius are usually limited to specific applications. The default values are recommended by Aungier with Equation 5-25 to Equation 5-26.

$$t_{b4} = 0.04r_4 \quad (5-25)$$

$$t_{b5} = 0.02r_4 \quad (5-26)$$

$$r_{h5} = 0.185r_4 \quad (5-27)$$

Aungier also proposed an effective correlation to estimate exit meridional velocity.

Ideally, absolute tangential velocity component,  $C_{\theta 4}$ , is 0.

$$C_{m5}/C_{m4} = 1 + 5(b_4/r_4)^2 \quad (5-28)$$

Now outlet shroud radius  $r_{s5}$ , can be calculated with sufficient parameters. The axial length and the number of blades are empirical equations 5-29 and 5-30.

$$\Delta z_R = 1.5(r_{s5} - r_{h5}) \quad (5-29)$$

$$N_R = 12 + 0.03(33 - \alpha_4)^2 \quad (5-30)$$

Slip factor is a concept initially introduced as a pump parameter. However, slip factor still plays a role at the inlet of the radial inflow turbine as presented in Equation 5-31.

$$\sigma = 1 - \sqrt{\sin\beta_4}/N_R^{0.7} \quad (5-31)$$

In Equation 5-31, slip factor is only a function of inlet blade angle as the blade number has already been settled in Equation 5-30. Without considering the slip factor in the design process will yield inaccurate results. Therefore, slip factor must be taken into account in the preliminary design process. The basic idea, explained by Equations 5-32 to 5-35, is to obtain a blade angle that yields the same incidence angles considering or without considering the slip factor and blockage, i.e.  $i_4^* = i_4$ .

$$K_{B4} = 1 - N_R t_{b4} / (2\pi r_4 \sin\beta_4) \quad (5-32)$$

$$C_{\theta 4}^* = \sigma(U_4 - C_{m4} \cot\beta_4 / K_{B4}) \quad (5-33)$$

$$i_4^* = \beta_4 - 90^\circ + \tan^{-1}[(U_4 - C_{\theta 4}^*)K_{B4}/C_{m4}] \quad (5-34)$$

$$i_4 = \beta_4 - 90^\circ + \tan^{-1}[(U_4 - C_{\theta 4})K_{B4}/C_{m4}] \quad (5-35)$$

With velocities at the inlet and outlet, the static enthalpies at the two stations can be obtained from Equation 5-36 to Equation 5-39. The static and total enthalpies can be used to calculate the reaction as in Equation 5-40, which is an important parameter to evaluate the design.

$$h_4 = h_{t4} - \frac{1}{2}(C_{m4}^2 + C_{\theta 4}^2) \quad (5-36)$$

$$b_4 = \dot{m}/(2\pi r_4 \rho_4 C_{m4}) \quad (5-37)$$

$$C_{m5} = [1 + 5(b_4/r_4)^2]C_{m4} = \frac{\dot{m}}{[\pi(r_{s5}^2 - r_{h5}^2)\rho_5]} \quad (5-38)$$

$$h_5 = h_{t5} - \frac{1}{2}C_{m5}^2 \quad (5-39)$$

Figure 5.3 is outlet velocity triangle of the rotor.  $C_{m5}$  is perpendicular to the outlet surface and assumed to be uniform across the area, hence the tangential component of the outlet absolute velocity  $C_{\theta 5}$  is 0 then  $C_5 = C_{m5}$ .

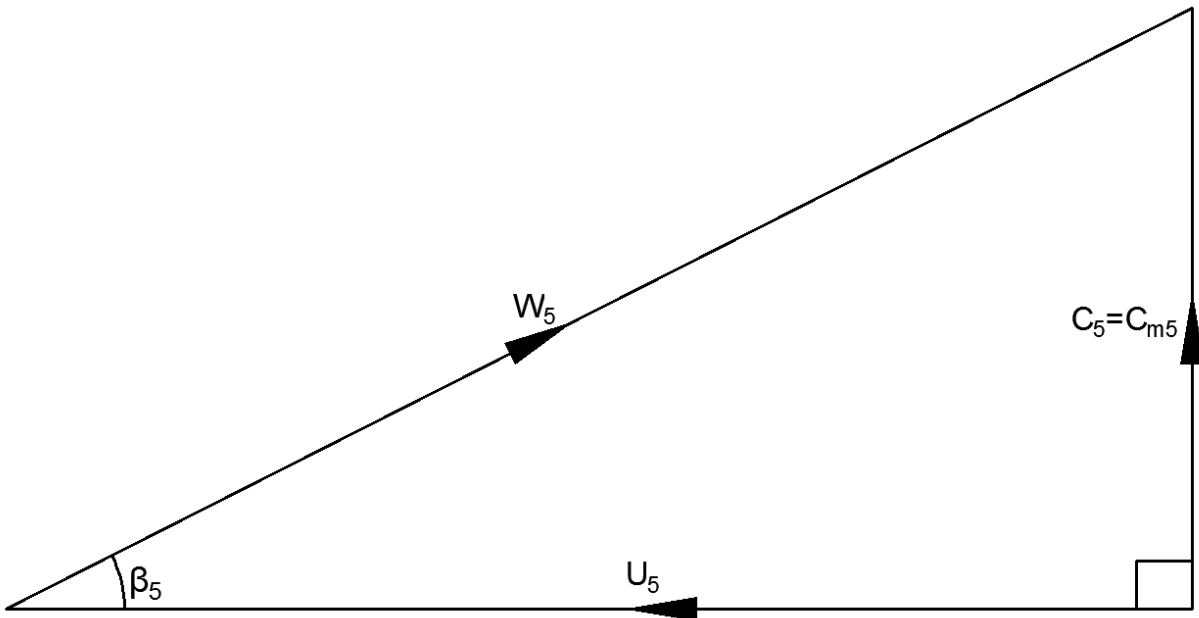


Figure 5.4 Outlet velocity triangle of the rotor

Figure 5.4 is the flow chart of the 1-D design. An initial rotational speed is calculated by Equations 5-9 to 5-14. With a  $\omega$ , all the velocities and basic dimensions at the inlet can be determined. A check whether the inlet relative velocity is about  $70^\circ$  is placed at this moment. If the angle is too large, increase the coefficient  $c_{vs}$  and restart this loop.

After deciding the inlet velocities, outlet parameters can be obtained since Equation 5-28. A new flow rate at the outlet is gained then yields a new rotational speed based on the definition of specific speed. If the new rotational speed is different, substitute the old one and iterate the loop until it converges to a steady result of rotation speed.

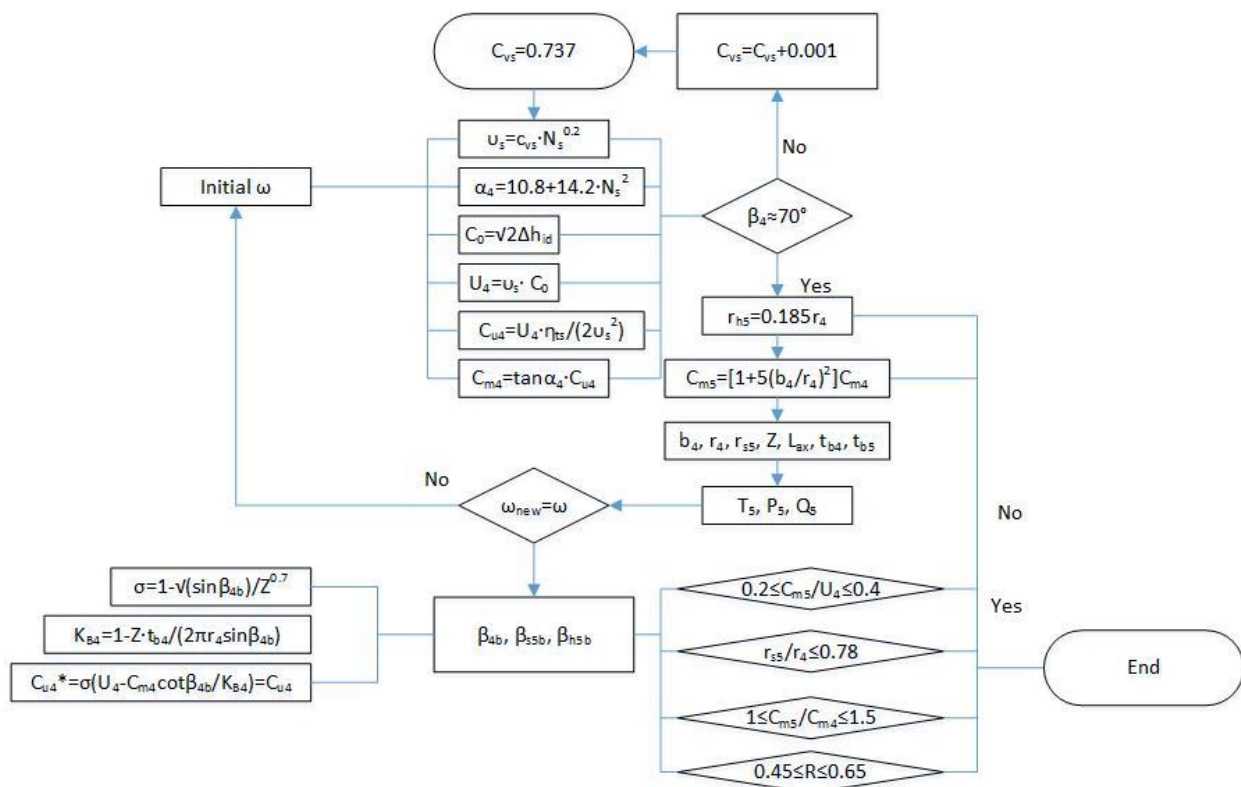


Figure 5.5 Flow chart of 1-D design

The last step is to decide the inlet blade angle described before as Equations 5-32 to 5-35. A bisection method is used to find the proper blade angle, for there has to be only one

result within 70° to 110°. After all the parameters are determined, it is necessary to evaluate the design with some recommended values proposed by successful researchers. The criteria are obtained from numerous validated good designs. If some of the limitations are not met, return and adjust the corresponding parameters. However, it is not strictly required to meet all the recommended parameter ranges.

Table 5.4 is the 1-D design results for different kinds of components. For each group, the radius of the rotor varies within 2mm. The shroud and hub radiuses at the outlet differ with each group only with 1mm. Therefore, as the designs are generally same with each other group, the design for the exhaust gas from combustion of propane without recuperator is selected. Then, all the other kinds of gases will be applied to the designed turbine to test the performance. The evaluation of the design for propane without recuperator is presented in Table 5.5. In this thesis, the meridional parameters are the averages of the shroud and hub. However, some researchers use the root mean square of the shroud and hub to represent meridional parameters. These parameters are subscripted with 'rms'. The design lies within all the recommended ranges except the one proposed by Whitfield & Baines<sup>[9, 10]</sup>. However, the design is still approved because only one range is not met and it is not necessary to lie in every recommended range. A sound 1-D design is the basis for 3-D detail design, which is in the next section.

Table 5.4 1-D design results for different kinds of components

		Propane without recuperat or	Propane with recuperat or	Ethane without recuperat or	Ethane with recuperat or	Methane without recuperat or	Methane with recuperat or
Rotor radius	$r_4$ (m)	0.1408	0.1392	0.1409	0.1394	0.1410	0.1394
Rotation Speed	rpm	24842.1	25319.7	24862.4	25022.2	24911.6	25033.1
Outlet hub radius	$r_{5h}$ (m)	0.0260	0.0257	0.0261	0.0258	0.0261	0.0258
Outlet shroud radius	$r_{5s}$ (m)	0.0894	0.0884	0.0894	0.0884	0.0895	0.0884
Inlet blade angle	$\beta_{4b}$ ( $^\circ$ )	93.1436	93.1436	93.1436	93.1436	93.1436	93.1436
Inlet flow angle	$\alpha_4$ ( $^\circ$ )	15.0955	15.0955	15.0955	15.0955	15.0955	15.0955
Inlet width	$b_4$ (m)	0.0241	0.0237	0.0241	0.0239	0.0241	0.0239
Rotor axial length	$\Delta z_R$ (m)	0.0950	0.0939	0.0950	0.0940	0.0951	0.0940
Number of blades	Z	22	22	22	22	22	22
Outlet shroud blade angle	$\beta_{5sb}$ ( $^\circ$ )	23.7933	23.7675	23.7934	23.8032	23.7933	23.8032
Outlet hub blade angle	$\beta_{5hb}$ ( $^\circ$ )	56.5274	56.5074	56.5274	56.5346	56.5273	56.5346
Inlet blade thickness	$t_{b4}$ (m)	0.0056	0.0056	0.0056	0.0056	0.0056	0.0056
Outlet blade thickness	$t_{b5}$ (m)	0.0028	0.0028	0.0028	0.0028	0.0028	0.0028

Table 5.5 Evaluation of the design

	Design results	Recommended range	Source
Inlet Blockage	14.03	$\leq 50\%$	Aungier <sup>[1]</sup>
Outlet Blockage	42.36	$\leq 50\%$	Aungier <sup>[1]</sup>
$\Delta z_R/b_4$	3.94	$\geq 1.5$	Aungier <sup>[1]</sup>
$C_{m5}/U_4$	0.278	0.2-0.4	Balje <sup>[5]</sup>
$d_{s5}/d_4$	0.6346	$\leq 0.78$	Balje <sup>[5]</sup>
$C_{m5}/C_{m4}$	1.1466	1-1.5	Wood <sup>[7]</sup>
$R=(h_4-h_5)/(h_{it}-h_{et})$	0.559	0.45-0.65	Aungier <sup>[1]</sup>
$\alpha_4$	15.096	$15^\circ-22^\circ$	Dixon, Rohlik <sup>[3, 8]</sup>
$\beta_{5,rms}$	30.91	$20^\circ-40^\circ$	Whitfield & Baines <sup>[9, 10]</sup>
$b_4/d_4$	0.0856	0.05-0.15	Whitfield & Baines, Dixon, Rohlik <sup>[3, 8-10]</sup>
$d_{5h}/d_{5s}$	0.2915	$< 0.4$	Dixon, Rohlik <sup>[3, 8]</sup>
$d_{5,rms}/d_4$	0.4674	0.53-0.66	Whitfield & Baines <sup>[9, 10]</sup>
$W_{5,rms}/W_4$	2.0603	2-2.5	Earl Logan <sup>[11]</sup>
$U_4/C_{0s}$	0.6956	0.55-0.8	Rohlik <sup>[8]</sup>
$C_{5,rms}/U_4$	0.278	0.15-0.5	Whitfield & Baines <sup>[9, 10]</sup>

## 5.2. Quasi 3-D blade design

In this section, the quasi 3-D design is primitive and will be adjusted after 3-D CFD simulations. A complete quasi 3-D design requires rotor end-wall contours to smoothly connect the inlet and outlet stations, straight-line element rotor blade camber lines along the contours and sometimes radial element rotor blade camber lines that eliminates the bending stresses in the blade due to the centrifugal forces at high rotation speed. The implement of radial element probable would sacrifice a little aerodynamic performance. However, this thesis focuses on seeking the optimum aerodynamic performances, so the radial element is not discussed this time.

### 5.2.1. Meridional Rotor End-Wall Contours

The preliminary design of the rotor end-wall contours connects the inlet and outlet stations with smooth contours. The hub contour is constructed to minimize passage curvature effects by using the largest possible  $90^\circ$  circular-arc that can fit in the geometry. Hence, the



radius of the circular-arc,  $R_c$ , would be the smaller of either  $(r_4-r_{h5})$  or  $\Delta z_R$ . When  $R_c = \Delta z_R$ , shown as Figure 5.5, a linear segment,  $L_4$ , is required to complete the contour at the inlet. When  $R_c = (r_4-r_{h5})$ , a linear segment,  $L_5$ , would be needed at the outlet. The shroud contour is constructed with a power-law relation:

$$r = r_{s5} + (r_4 - r_{s5})\xi^n \quad (5-40)$$

$$\xi = (z - z_5)/(\Delta z_R - b_4) \quad (5-41)$$

In Equation 5-40,  $n$  is an integer between 2 to 9. Connecting the mid points of hub and shroud end-wall contours can achieve a mean quasi-normal,  $A_m$  which should be closest to the average of the known inlet and exit areas  $A_4$  and  $A_5$ , as in Figure 5.6.

Figure 5.7 shows a series of shroud lines with different  $n$  from 2 to 9. At last, the  $A_m$  when  $n=5$  is closest to the average of  $A_4$  and  $A_5$ . Table 5.6 presents the  $A_m$  for each shroud design and their absolute differences to the average of  $A_4$  and  $A_5$ . In the flowing sections, the design with power of  $n=5$  for shroud meridional profile will be focused. However, to study the aerodynamics differences in accordance with various  $n$ , the shroud designs from  $n=3$  to  $n=9$  will be compared using CFD simulations.

Table 5.6 Difference between the  $A_m$  and average of  $A_4$  and  $A_5$

	$A_m$ (m <sup>2</sup> )	Absolute difference from the Average of $A_4$ and $A_5$ (m <sup>2</sup> )
n=3	0.025781	0.0036348
n=4	0.023431	0.0012854
n=5	0.021807	0.0003393
n=6	0.020616	0.0015296
n=7	0.019710	0.0024359
n=8	0.019001	0.0031449
n=9	0.018435	0.0037111
Average of $A_4$ and $A_5$	0.022146	0

In Figure 5.6, it can be seen that higher order power-law shroud profile has a steeper slope at the inlet and lower slope when approaching the exit. It can be expected that higher slope of the profile will give a higher acceleration in speed thus higher rate of pressure drop.

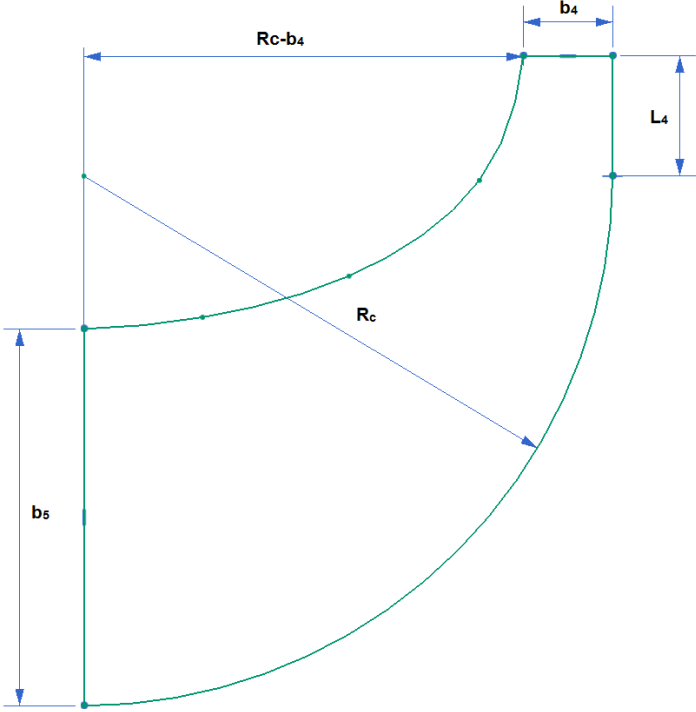


Figure 5.6 End-Wall Contours

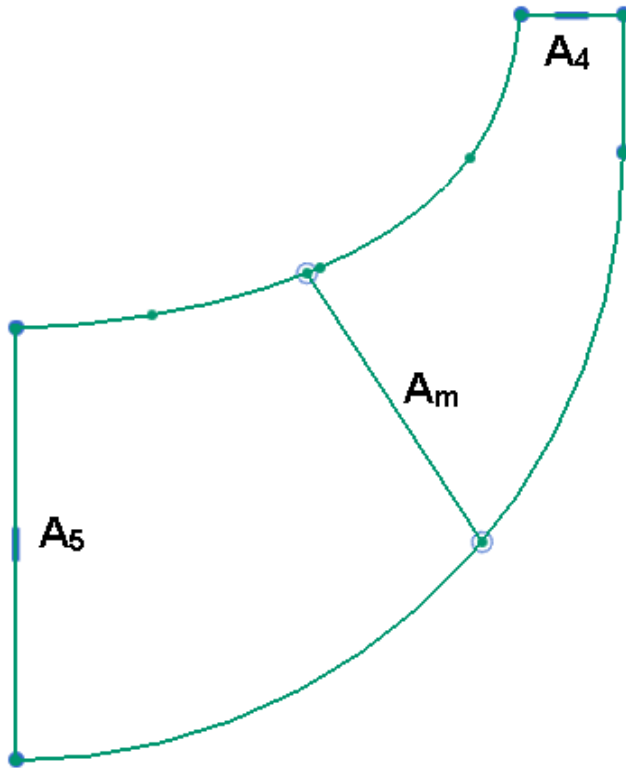


Figure 5.7 Power-Law Shroud Contour

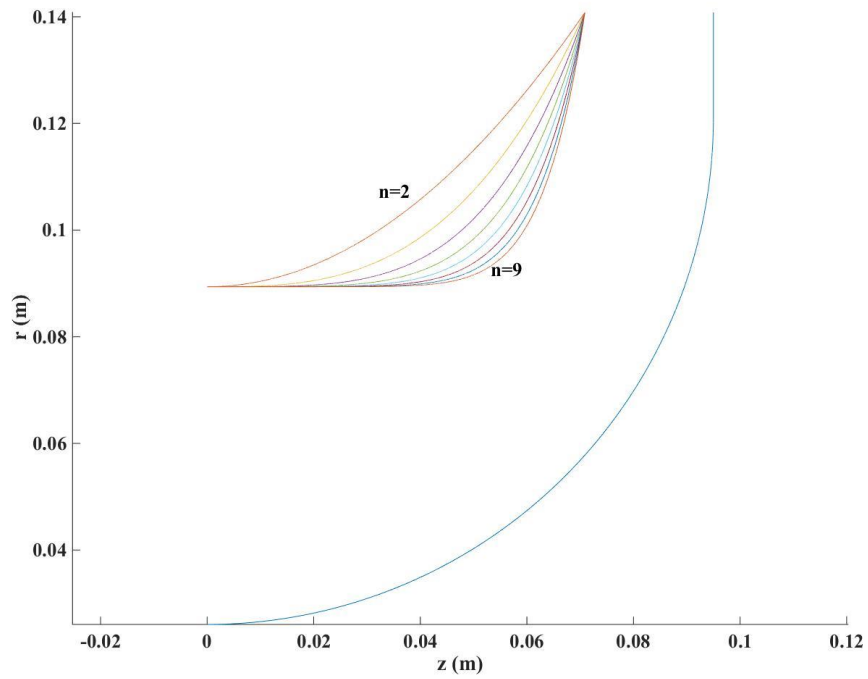


Figure 5.8 Power-Law shroud contours with  $n$  from 2 to 9

### 5.2.2. Design of Straight-Line Element Rotor Camber lines

Straight-line element blades are constructed along the shroud and hub contours. The blade camber line along the shroud contour is defined by <sup>[4]</sup>:

$$\theta(m) = Am + Bm^3 + Cm^4 \quad (5-42),$$

where A, B and C are:

$$A = \frac{\cot\beta_{5s}}{r_{5s}} \quad (5-43)$$

$$B = \frac{1}{m_4^2} \left[ \frac{\cot\beta_4}{r_4} - \frac{\cot\beta_{5s}}{r_{5s}} \right] \quad (5-44)$$

$$C = -\frac{B}{2m_4} \quad (5-45)$$

In Equation 5-42,  $m=0$  is the position of exit and  $m=m_4$  is at the inlet and represents the length of the contour. For the camber line along the hub contour:

$$\theta(m) = Dm + Em^2 + Fm^3 \quad (5-46)$$

At inlet,  $\theta_{4s}=\theta_{4h}$ , and they are shown as;

$$\theta_4 = \frac{m_{4s}}{2} \left[ \frac{\cot\beta_4}{r_4} + \frac{\cot\beta_{5s}}{r_{5s}} \right] \quad (5-46)$$

$$D = \frac{\cot\beta_{5h}}{r_{5h}} \quad (5-47)$$

$$E = \frac{3\theta_4}{m_{4s}^2} - \frac{1}{m_{4s}} \left[ 2 \frac{\cot\beta_{5h}}{r_{5h}} + \frac{\cot\beta_4}{r_4} \right] \quad (5-48)$$

$$F = \frac{1}{m_{4s}^2} \left[ \frac{\cot\beta_{5h}}{r_{5h}} + \frac{\cot\beta_4}{r_4} \right] - \frac{2\theta_4}{m_{4s}^3} \quad (5-49)$$

The corresponding blade angle distribution for either contour is calculated by:

$$\cot\beta = r \frac{\partial\theta}{\partial m} \quad (5-50)$$

Figure 5.8 and Figure 5.9 show the camber lines and blade angles along the contours when  $n=5$ . The design looks very similar when  $n=9$ .

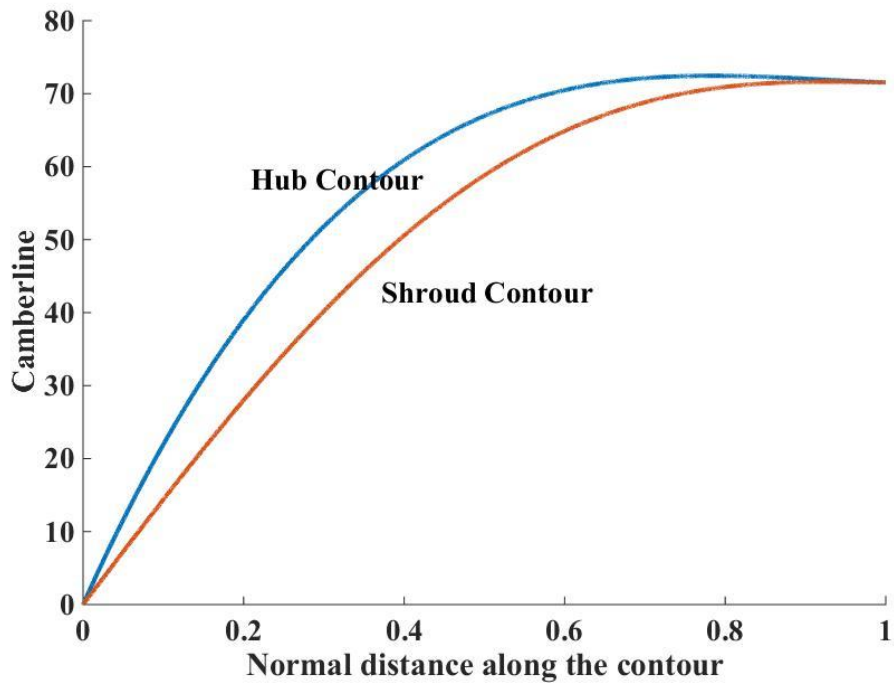


Figure 5.9 Camber line along the contours when  $n=5$

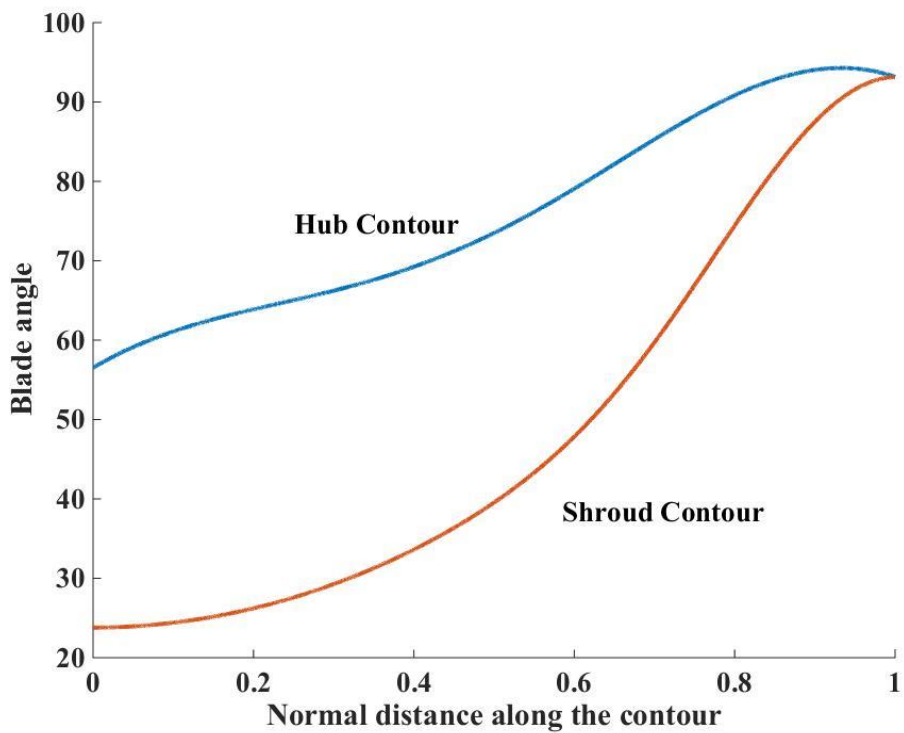


Figure 5.10 Blade angles along the contours when  $n=5$

### 5.3. 1-D Analysis

The performance is based on loss models for the radial inflow turbine. This analysis consists of the flowing loss models: Incidence loss, passage loss, tip clearance loss, windage loss, trailing edge loss and exit energy loss. The total to static efficiency can be calculated from losses as:

$$\eta_{ts} = \frac{\Delta h_0}{\Delta h_0 + \sum \Delta h_{loss}} \quad (5-51)$$

#### 5.3.1. Loss Models <sup>[69]</sup>

Incidence loss

$$\Delta h_{inc} = \frac{1}{2} W_{u4}^2 \quad (5-52)$$

Passage loss

$$\Delta h_p = 0.5 k (W_4^2 \cos^2 i_4 + W_{5,rms}^2) \quad (5-53)$$

In Equation 5-53 k is 0.3.

Tip clearance loss

$$\Delta h_c = \frac{U_4^3 Z}{8\pi} [k_a \varepsilon_a C_a + k_r \varepsilon_r C_r + k_{ar} \sqrt{\varepsilon_a \varepsilon_r C_a C_r}] \quad (5-54)$$

In Equation 5-54 the axial clearance,  $\varepsilon_a$ , and radial clearance,  $\varepsilon_r$ , are equal to 0.00035m.

In addition,  $k_a=0.4$ ,  $k_r=0.75$ ,  $k_{ar}=-0.3$ .

$$C_a = \frac{1-(r_{5s}/r_4)}{C_{m4} \cdot b_4}, \quad C_r = \left(\frac{r_{5s}}{r_4}\right) \frac{\Delta z_R - b_4}{C_{m4} \cdot b_5 \cdot r_5} \quad (5-55)$$

Windage loss

$$\Delta h_w = k_f \frac{\bar{\rho} \cdot U_4^3 \cdot r_4}{2 \cdot \dot{m} \cdot W_5^2} \quad (5-56)$$

$$k_f = \frac{3.7 \left(\frac{\varepsilon_b}{r_4}\right)^{0.1}}{Re^{0.5}}, \quad \text{for } Re < 10^5 \quad (5-57)$$

$$k_f = \frac{0.102 \left(\frac{\varepsilon_b}{r_4}\right)^{0.1}}{Re^{0.2}}, \text{ for } Re > 10^5 \quad (5-58)$$

$\varepsilon_b$  is assumed to be 0.0003m and Reynolds Number is calculated by:

$$Re = \frac{\bar{\rho} \cdot \bar{C} \cdot r_4}{\bar{\mu}} \quad (5-59)$$

$\bar{\rho}$ ,  $\bar{C}$  and  $\bar{\mu}$  are average values between inlet and outlet.

Trailing edge loss

Trailing edge loss is calculated based on relative total pressure loss as:

$$\Delta P_{0,rel} = \frac{\rho_5 W_{5,rms}^2}{2g} \left( \frac{\Delta z_{R-t}}{\pi(r_{5t} + r_{5s}) \cos(\beta_{5,rms})} \right)^2 \quad (5-60)$$

$$\Delta h_{te} = \frac{2}{\gamma M_{5,rel}^2} \frac{\Delta P_{0,rel}}{P_5 \left( 1 + \frac{W_{5,rms}^2}{2T_5 C_p} \right)^{\frac{\gamma}{\gamma-1}}} \quad (5-61)$$

Exit Energy loss

$$\Delta h_{exit} = \frac{C_5^2}{2} \quad (5-62)$$

### 5.3.2. 1-D Analysis results

Table 5.7 is the 1-D analysis results.

From Table 5.7, it is seen that windage loss and trailing energy loss are almost 0 compared to the other losses. The most loss comes from the passage loss. The exit energy loss is the second largest loss after the passage loss. However, a well-designed diffuser can recover most of the exit energy. The tip clearance loss is the third source of loss. For a larger tip clearance, the loss will be higher.

Table 5.7 1-D analysis results

Incidence loss	$\Delta h_{inc}$	0.5426 kJ/kg·K
Passage loss	$\Delta h_p$	7.1440 kJ/kg·K
Tip clearance loss	$\Delta h_c$	1.8980 kJ/kg·K
Windage loss	$\Delta h_w$	0.2267 J/kg·K
Trailing edge loss	$\Delta h_{te}$	0 J/kg·K
Exit energy loss	$\Delta h_{exit}$	5.2327 kJ/kg·K
Enthalpy drop	$\Delta h_0$	14.818 kJ/kg·K
Total to static efficiency in Rotor	$\eta_{ts-rotor}$	89.31 %
Total to total efficiency in Rotor	$\eta_{tt-rotor}$	92.79 %
Total to static efficiency stage	$\eta_{ts-stage}$	87.91 %
Total to total efficiency stage	$\eta_{tt-stage}$	91.28 %
Specific speed	$N_s$	0.55
Specific Diameter	$D_s$	2.2556
Flow coefficient	$\phi = C_{m5}/U_4$	0.2780
Work coefficient	$\psi = \Delta h_0/U_4^2$	0.8989



## 5.4. 3D analysis

### 5.4.1. Model construction and meshing of the rotor in BladeGen

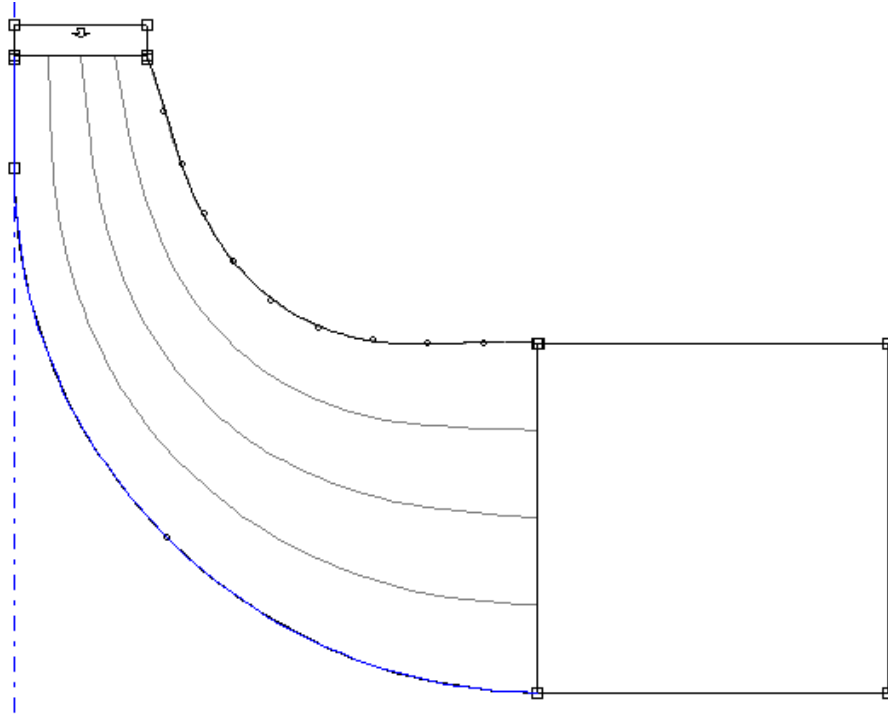


Figure 5.11 Meridional view in Blade Gen

The model of the rotor is built in the software of Blade Gen in ANSYS. As shown in Figure 5.10 and Figure 5.11. The meridional shroud profile is polynomial with power of  $n=5$ . The blade angles are built by inserting ten points of the camber line curves on the hub and the shroud designed in the section 5.2 previously. The curves coincide well with the design, indicating that the software uses the same method to construct the model. One important thing to be noted is that the preference setting for the meridional profile in Blade Gen should be changed to 'from trailing edge to leading edge.'

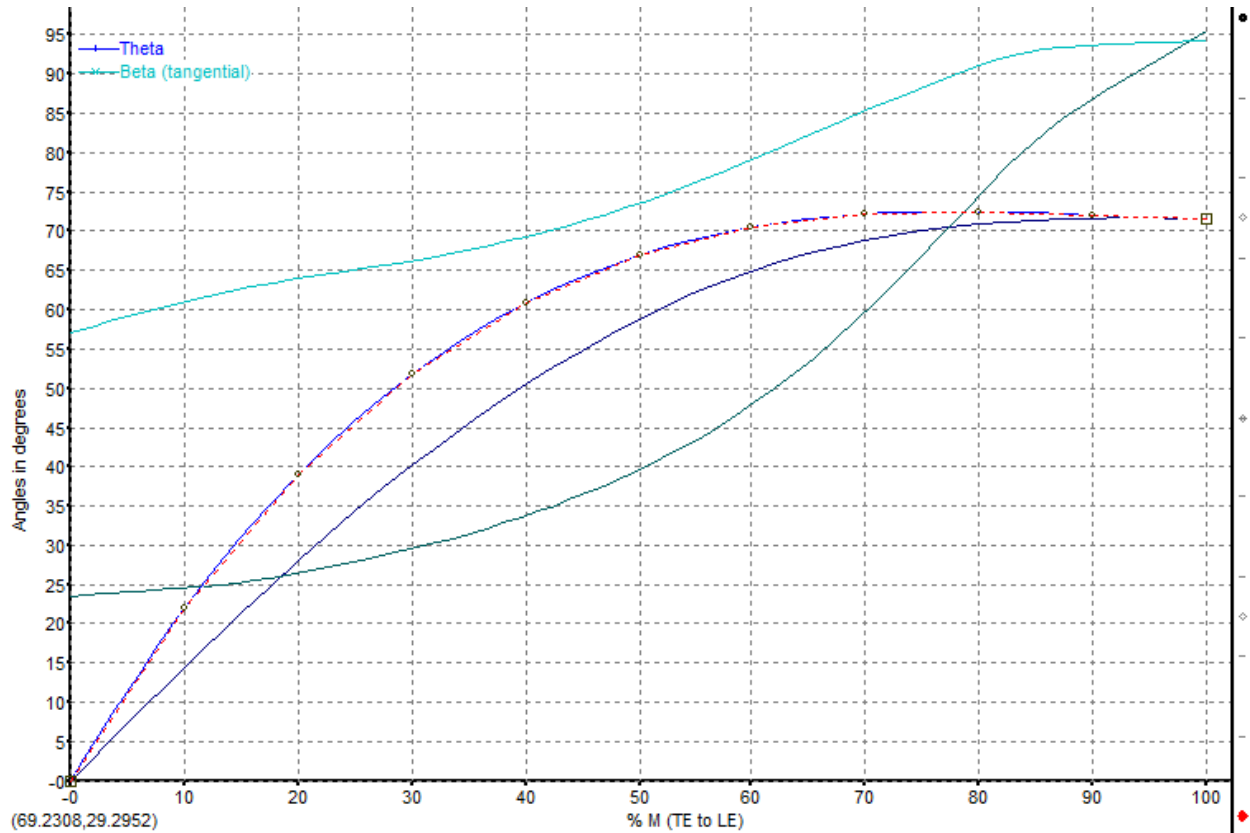


Figure 5.12 Blade angles and camber lines in Blade Gen

The model is meshed with Turbo Grid as in Figure 5.12. The machine type is chosen to be radial turbine. The tip clearance is set with normal distance of 0.5mm. Topology method is used with automatic optimized method. The near wall element size is selected with  $y^+$  of  $1.0e6$ .

The mesh statistics results are presented in Table 5.8. The meshing results meet all the limitations except the maximum element volume ratio. The largest ratio is 5.6024 larger than the limit of 2. These bad elements take 0.0997% of the total elements. However, the meshing result should be good enough to proceed to the simulation process.

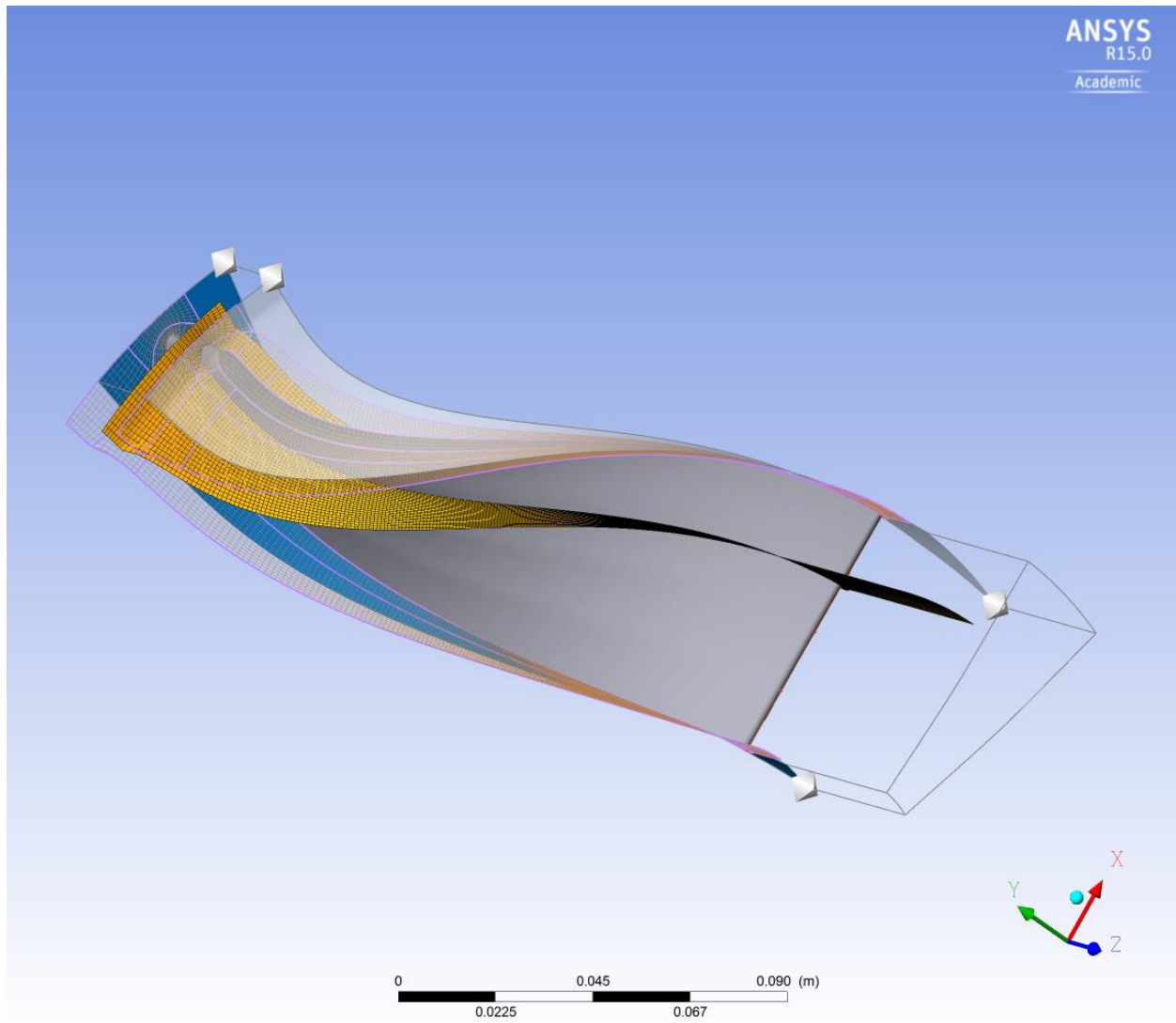


Figure 5.13 Meshing of the rotor

Table 5.8 Mesh statistics of the rotor

Mesh Measure	Value	%bad	Limits	
Minimum Face Angle	30.512 <sup>o</sup>	0	≥15 <sup>o</sup>	√
Maximum Face Angle	144.597 <sup>o</sup>	0	≤165 <sup>o</sup>	√
Maximum Element Volume Ratio	5.6024	0.0997	≤2	!
Minimum Volume	3.2422e-12 m <sup>3</sup>	0	≥0 m <sup>3</sup>	√
Maximum Edge Length Ratio	51.3201	0	≤100	√
Maximum Connectivity Number	10	0	≤12	√

### 5.4.2. Pre-setting of 3-D analysis

To better perform the simulation, a nozzle is implemented before the inlet of the rotor, as shown in Figure 5.13. Several runs were conducted in advance to obtain a right nozzle exit blade angle that would lead a proper inlet flow angle at the inlet of the rotor. However, it should obey the following Equations 5-63 to 5-67 to obtain a proximate flow angle at the exit of the nozzle.

Table 5.9 Flow angles in 1-D calculation and 3-D simulation

		1-D Calculation	3-D simulation in CFX
Flow angle at the nozzle exit	$\alpha_3$	14.78°	15.05°
Flow angle at the rotor inlet	$\alpha_4$	15.096°	15.12°
Flow angle at the rotor inlet with blockage	$\alpha_4^*$	17.419°	17.2°

$$C_{m3}r_3\rho_3 = C_{m4}r_4\rho_4 \quad (5-63)$$

$$C_{u3}r_3 = C_{u4}r_4 \quad (5-64)$$

$$T_{3t} = T_{4t} \rightarrow T_3 + \frac{C_3^2}{2C_p} = T_4 + \frac{C_4^2}{2C_p} \quad (5-65)$$

$$P_{3t} = P_{4t} \quad (5-66)$$

$$\frac{r_3}{r_4} = 1 + 2b_4 \sin \alpha_4 / r_4 \quad (5-67)$$

Solving the above Equations yields an exit flow angle  $\alpha_3$  of 14.42°. The interface between nozzle block and rotor block is set at the middle of the exit of nozzle and the inlet of rotor. Table 5.9 is a comparison between 1-D calculated flow angles and flow angles in CFX simulation.

The 1-D and 3-D calculation results are close. The inlet flow angles at the inlet from the 3-D simulation by CFX are observed at the sudden jump of the curve in Figure 5.14.

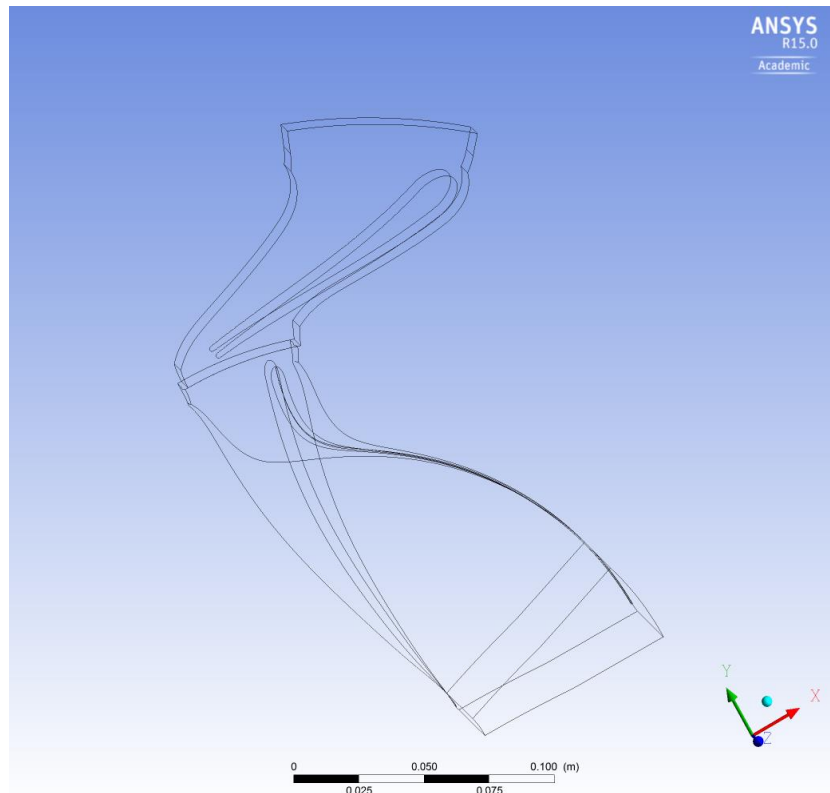


Figure 5.14 Structure simulated in CFX

At the beginning of Figure 5.14, a jump in absolute flow angle occurs because when the flow enters the rotor, the flow area suddenly decreases resulting in a rise of  $C_{m4}$ , due to the appearing blockage.

The CFX simulations use  $k-\epsilon$  method. The components of the gas mixture use ideal gas models. However, the specific heat should vary with temperature. Expressions are built in with Equations 5-3 to 5-6 and applied to the heat capacity of each ideal gas component. The residual target is setting RMS to be  $10^{-5}$ . The Advection Scheme is high resolution, while high resolution is selected for the Turbulence Numerics. Across the nozzle and the rotor, 1.34% pressure drop is assumed based on the 1-D design process by Equation 5-20.

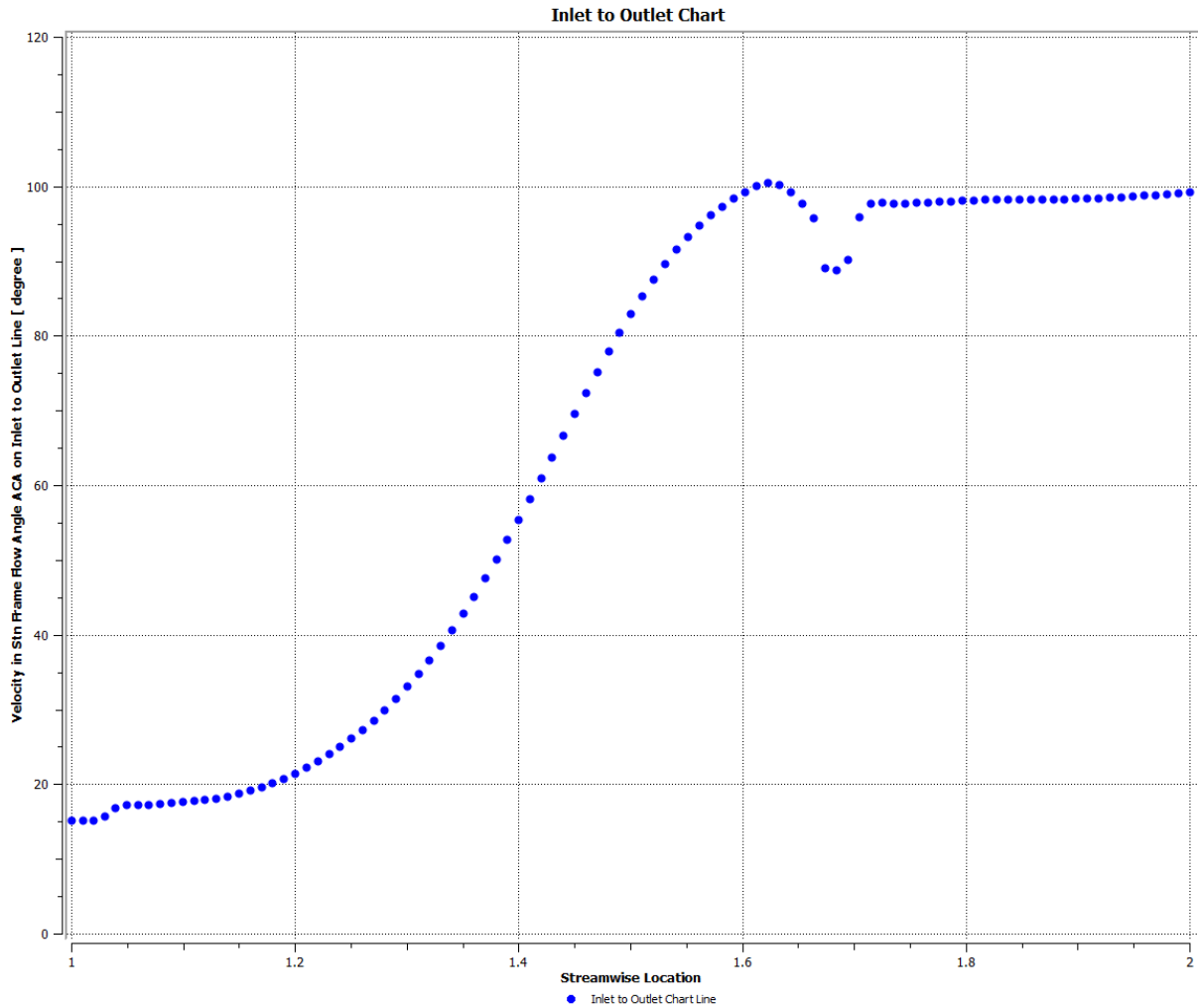


Figure 5.15 Flow angles in stationary frame in the rotor

## 5.5. 3-D analysis results

### 5.5.1. Velocity triangles

Figure 5.15 and Figure 5.16 are the inlet and outlet velocity triangles. The solid lines are velocities calculated from 1-D design, and the dash lines are the results from CFX simulations. The results from all the different designs are very close to each other, so only the simulation results of the design when  $n=5$  are presented in the two figures.

The values of velocities are presented in Table 5.10 and Table 5.11. The inlet velocities are very close to the designed values. The dash lines from CFD simulation almost perfectly sit on the solid lines by 1-D analysis.

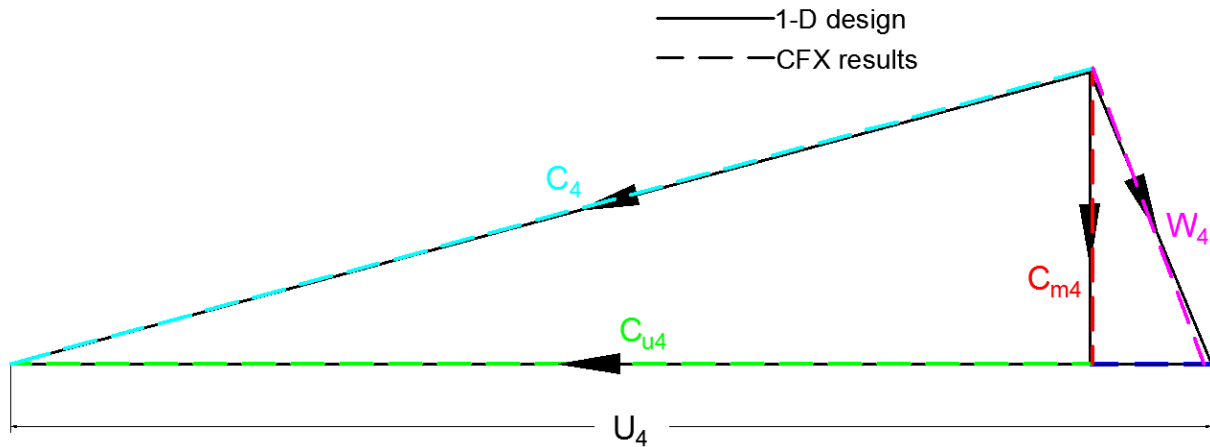


Figure 5.16 Inlet velocity triangles

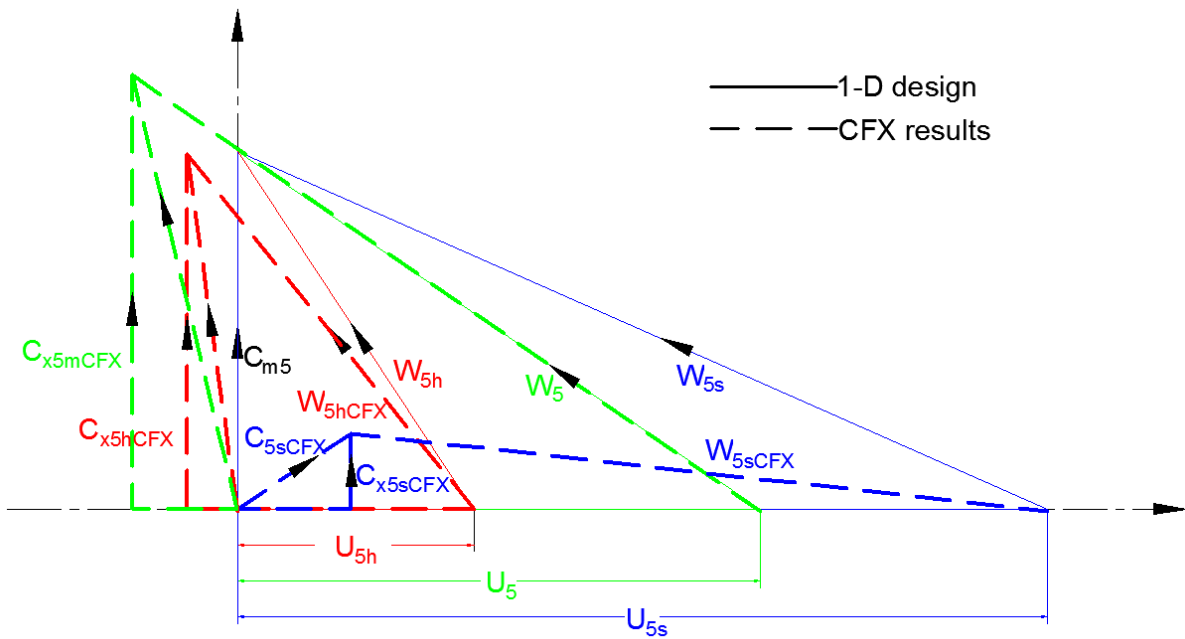


Figure 5.17 Outlet velocity triangles

Table 5.10 Values of inlet velocities

	$C_4$	$C_{u4}$	$W_4$	$W_{u4}$	$C_{m4}$	$U_4$
Designed values (m/s)	343.2354	331.3914	96.8474	37.2713	89.3883	368.6626
Results from CFX (m/s)	344.2781	332.176	96.7163	34.169	90.4794	366.345

Seen from Figure 5.16 and Table 5.11, the velocities obtained from CFX simulation are different from 1-D design. At the middle of the exit, the relative flow angle coincides with the design. However, the axial velocity at the mid is larger than the design. The axial velocity near the hub is close to the expected value in design and axial velocity near the shroud is much smaller than the design. In design process, the axial velocity is assumed to be uniform all around the exit surface. Nevertheless, this cannot be true in the reality considering the viscosity. The relative velocity will decrease at the positions near to the end-walls. Therefore, it can be expected that the axial velocities at the hub and shroud are smaller than the velocities near the middle of the passage. In addition, the tangential components of the absolute velocities are not zeros.

Table 5.11 Values of outlet velocities

	$C_5$	$C_{u5}$	$W_5$	$W_{u5}$	$C_{x5}$	$U_5$
Designed values (m/s)	102.489	0	181.7472	150.0933	102.4892	150.0933
Results from CFX (m/s)	124.363	30.223	213.577	180.281	114.516	150.0585
	$C_{5h}$	$C_{u5h}$	$W_{5h}$	$W_{u5h}$	$C_{x5h}$	$U_{5h}$
Designed values (m/s)	102.489	0	122.8556	67.7454	102.4892	67.7454
Results from CFX (m/s)	119.079	14.407	130.8654	82.2407	101.795	67.8335
	$C_{5s}$	$C_{u5s}$	$W_{5s}$	$W_{u5s}$	$C_{x5s}$	$U_{5s}$
Designed values (m/s)	102.489	0	254.0334	232.4412	102.4892	232.4412
Results from CFX (m/s)	41.3284	32.683	200.8968	199.723	21.6851	232.4061

### 5.5.2. 3-D performances analysis results

1-D analysis won't be able to find the differences in performances for models with different shroud profiles. However, CFD analysis can examine the details in the flow which could result in changes in the performances of the model.

Table 5.12 presents the analysis results for all the models with polynomial shroud profiles with power from  $n=3$  to  $n=9$ . The models with shroud profiles of  $n=4$  and  $n=5$  have the



slight highest efficiencies out of all the other designs. However, to decide the best choice for the design needs close examinations on the details of the flow.

Table 5.12 Results of performances analysis by CFX

	n=3	n=4	n=5	n=6	n=7	n=8	n=9
$\dot{m}$ , kg/s	0.77121	0.77121	0.77121	0.77121	0.77121	0.77121	0.77121
$T_5$ , K	1062.8	1065.88	1064.64	1065.83	1065.12	1065.88	1065.61
$T_{5t}$ , K	1068.99	1071.26	1070.25	1071.16	1070.82	1071.21	1070.71
$P_5$ , kPa	100.862	102.784	102.164	102.514	102.226	102.357	101.989
$P_{5t}$ , kPa	103.339	104.968	104.431	104.671	104.533	104.515	104.042
$\eta_{rtt}$ , %	93.58%	94.71%	94.64%	94.19%	94.26%	93.82%	93.34%
$\eta_{rts}$ , %	88.72%	90.26%	90.07%	89.84%	89.62%	89.50%	89.26%
$\eta_{nrts}$ , %	90.68%	91.85%	91.70%	91.35%	91.38%	91.00%	90.53%
$\eta_{nrts}$ , %	86.13%	87.68%	87.41%	87.27%	87.03%	86.94%	86.70%

### 5.5.3. Pressure on blade and velocity near blade

Figures 5.17-5.23 are the pressure, temperature on the blade and velocity near the blade for each model.

To examine the aerodynamics performances of a blade, blade loading diagrams are good ways to study the aerodynamics properties distributions. For the blades of the radial inflow turbines, blade loading graphs are not good enough to describe the flow near the blade, because the blade is so twisted. Fortunately, CFD is able to present the results in 3-D which is distinct to observe.

Seen from the pressure on the blade, an area of low pressure appears near the place where the curvature is smallest near the profile. The positions that have the smallest curvature turn the direction faster than the other places so that the velocity would accelerate more aggressively. According to the figures of Mach number contours near the blade, the velocities

become higher near places that change the direction fastest. Therefore, a low pressure area occurs at the same time.

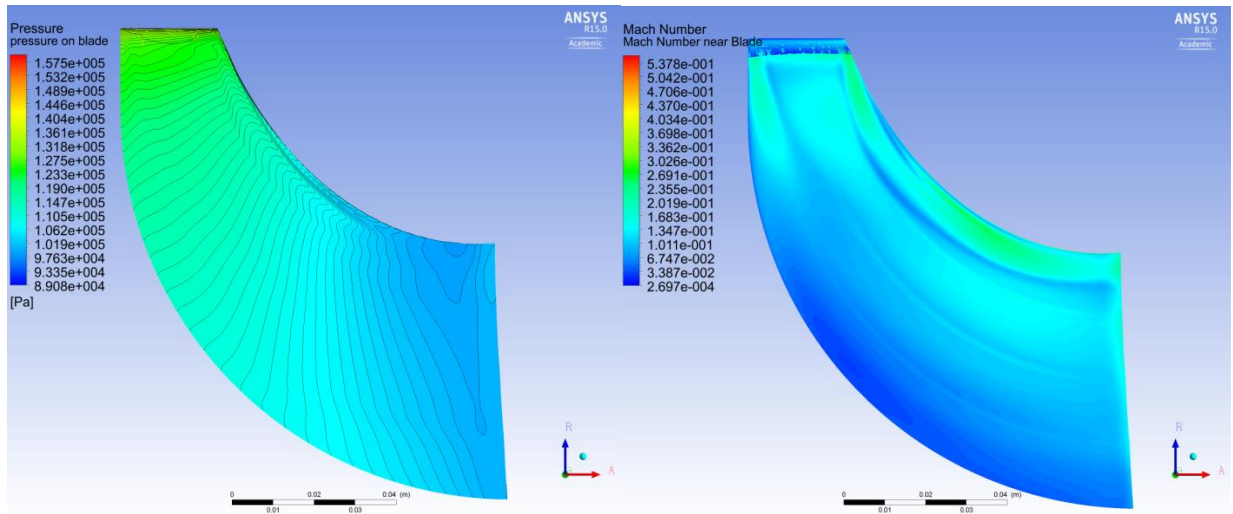


Figure 5.18 Pressure on the blade and velocity near the blade for the design of  $n=3$

The area of low pressure may cause high stress in the blade, and the concentration of high speed flow may erode the surface the blade. Therefore, the area of low pressure and high speed should be avoided, or at least the gradient of the pressure should be minimized if these areas cannot be eliminated.

By comparing all the pressure and velocities distributions on the blade, designs with power from  $n=7$  to  $n=9$  are not as good choices as the other models.

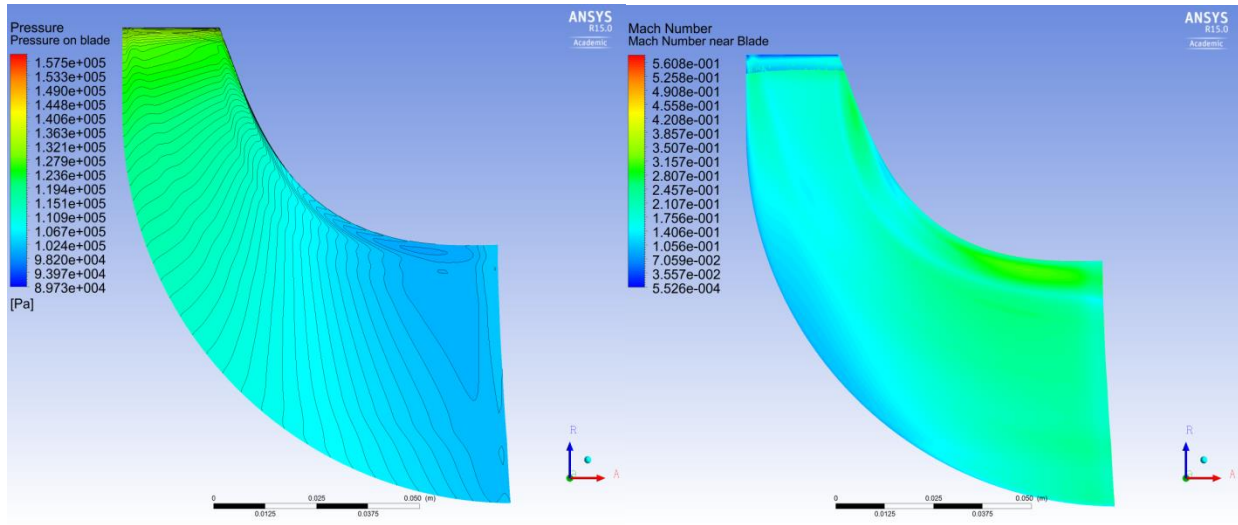


Figure 5.19 Pressure on blade and velocity near the blade for the design of  $n=4$

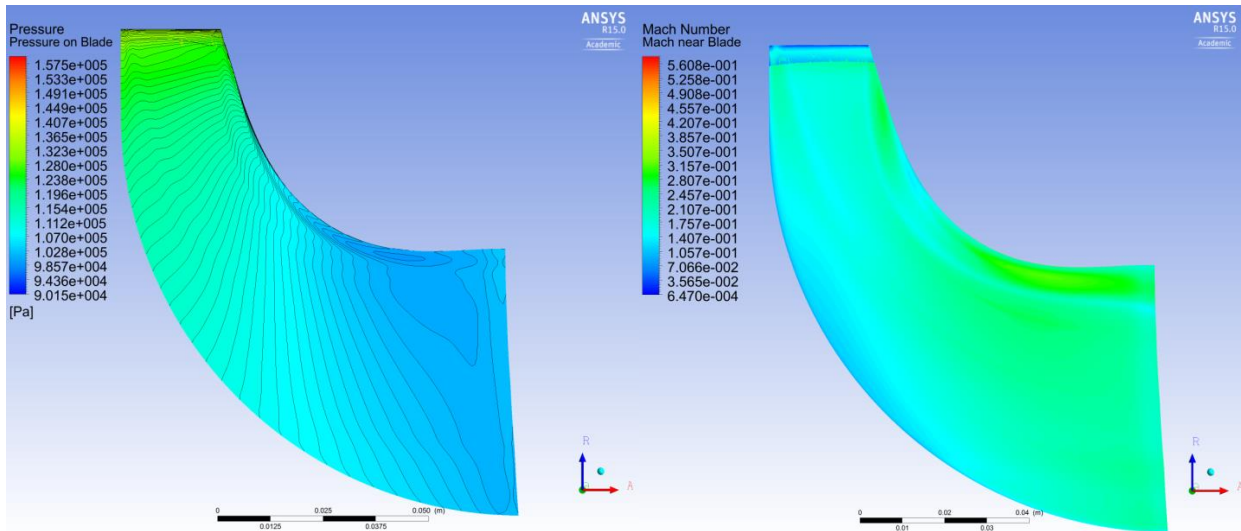


Figure 5.20 Pressure on blade and velocity near the blade for the design of  $n=5$

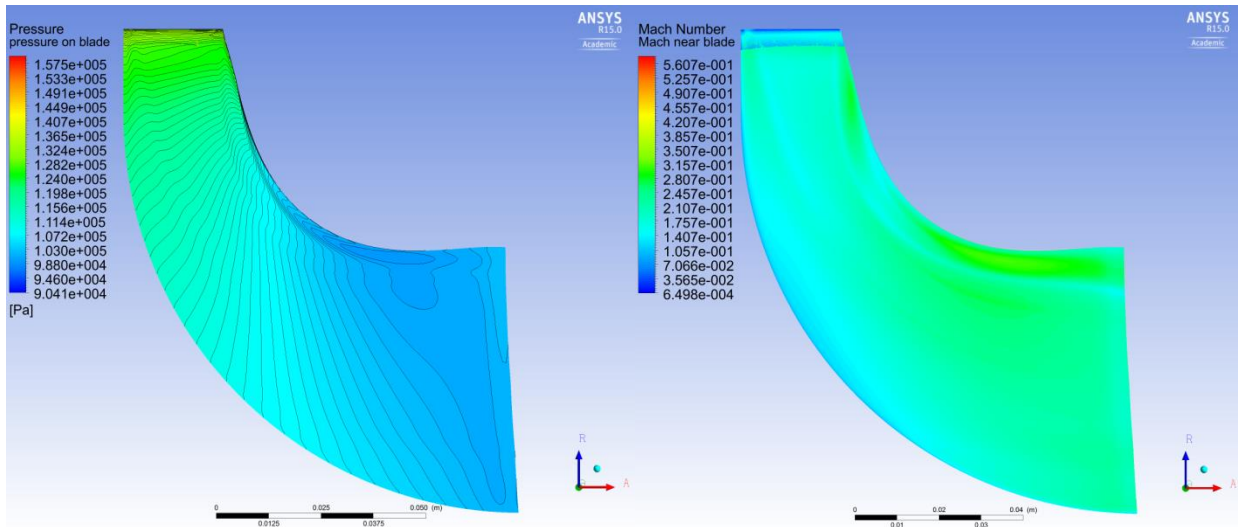


Figure 5.21 Pressure on blade and velocity near the blade for the design of  $n=6$

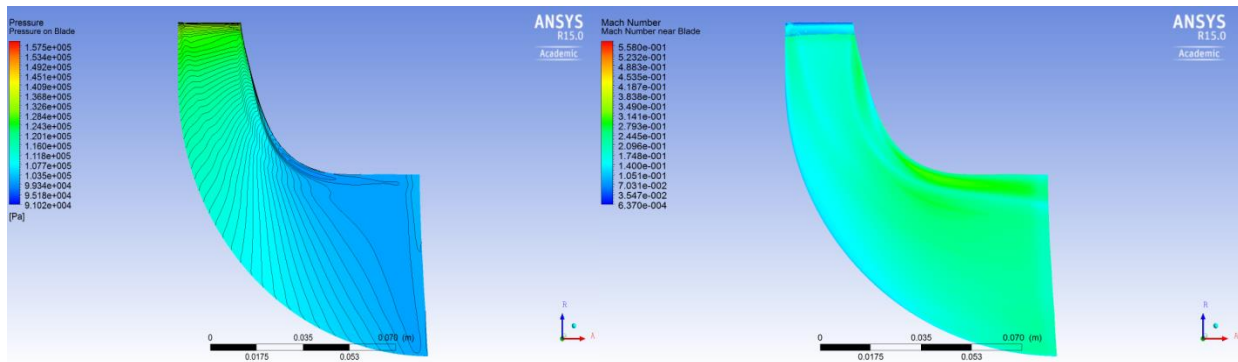


Figure 5.22 Pressure on blade and velocity near the blade for the design of  $n=7$

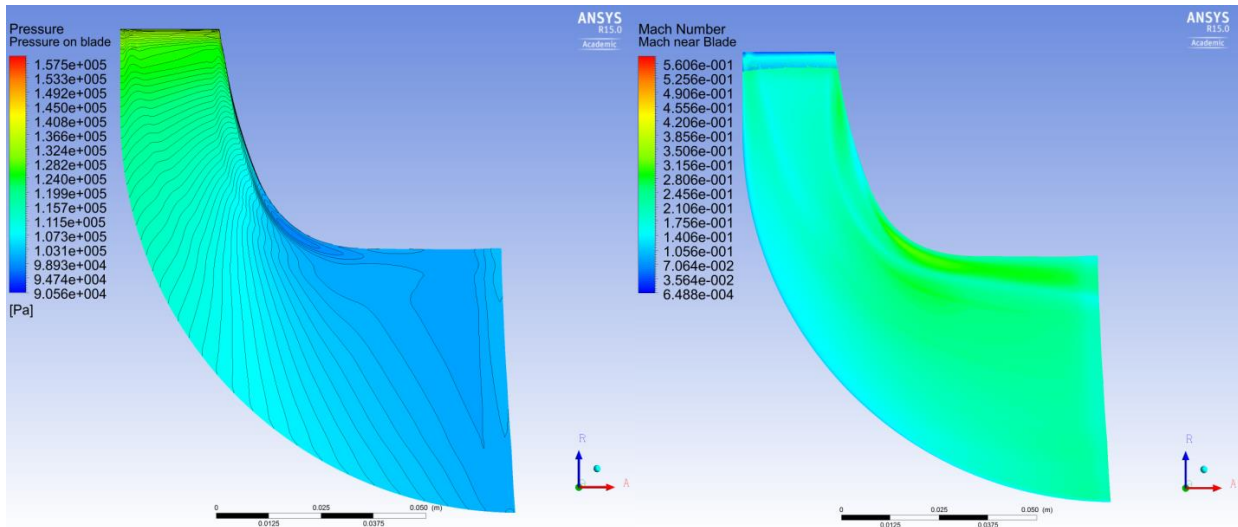


Figure 5.23 Pressure on blade and velocity near the blade for the design of  $n=8$

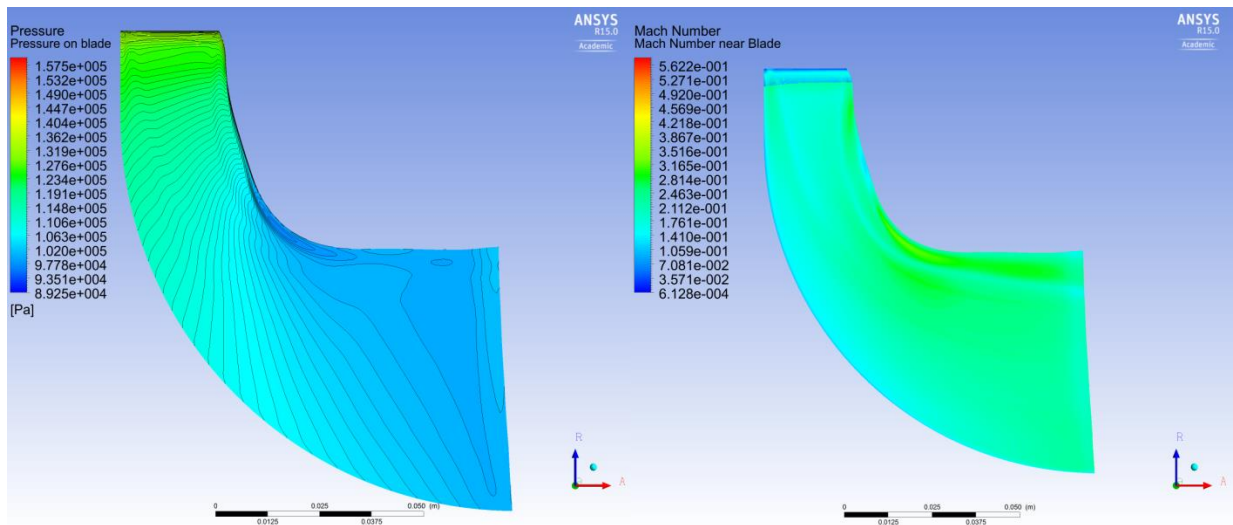


Figure 5.24 Pressure on blade and velocity near the blade for the design of  $n=9$

#### 5.5.4. Flow at the inlet

Figures 5.24 to 5.30 are streamlines in blade-to-blade view near the inlet at the spans of 0.1, 0.5 and 0.9 from left to right. It is important to have stable flow in the gas path and the inlet is one of the positions where the separation and circulation most likely happen. For the designs with the powers of  $n=3$  and  $n=4$ , a circulation happens near the inlet. Therefore, the

designs with polynomial shroud meridional profiles with power of  $n=5$  and  $n=6$  are chosen to be further examined, according to the results in Section 5.5.3 and 5.5.4.

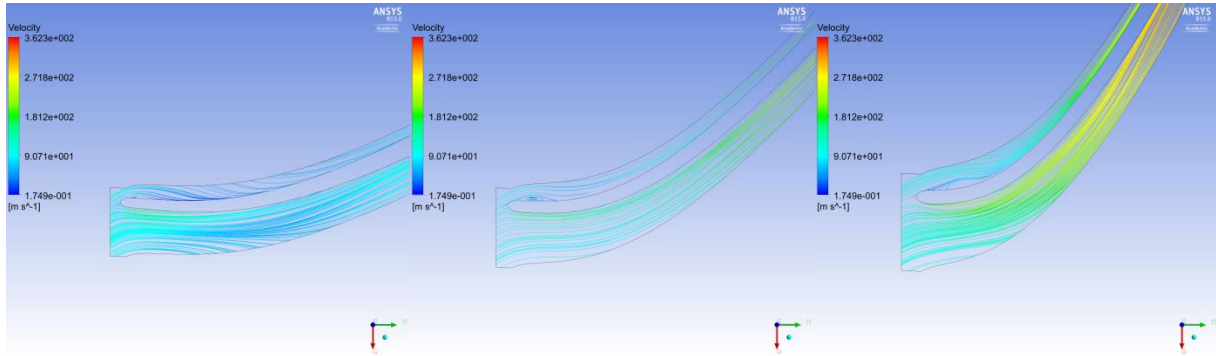


Figure 5.25 Streamlines in blade-to-blade view at spans of 0.1, 0.5 and 0.9 for designs of  $n=3$

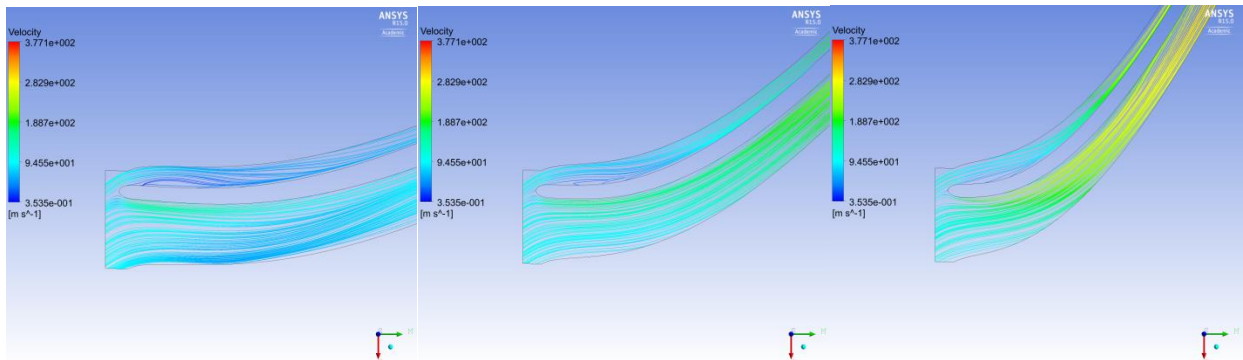


Figure 5.26 Streamlines in blade-to-blade view at spans of 0.1, 0.5 and 0.9 for designs of  $n=4$

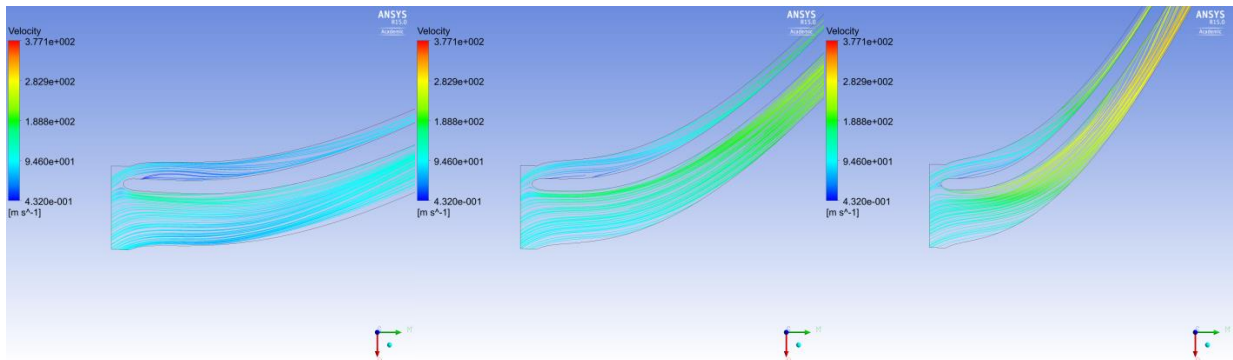


Figure 5.27 Streamlines in blade-to-blade view at spans of 0.1, 0.5 and 0.9 for designs of  $n=5$



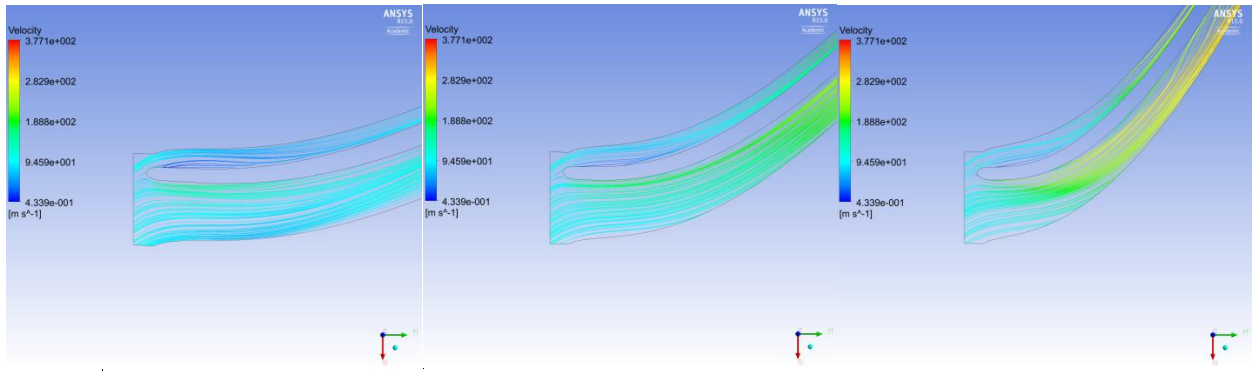


Figure 5.28 Streamlines in blade-to-blade view at spans of 0.1, 0.5 and 0.9 for designs of  $n=6$

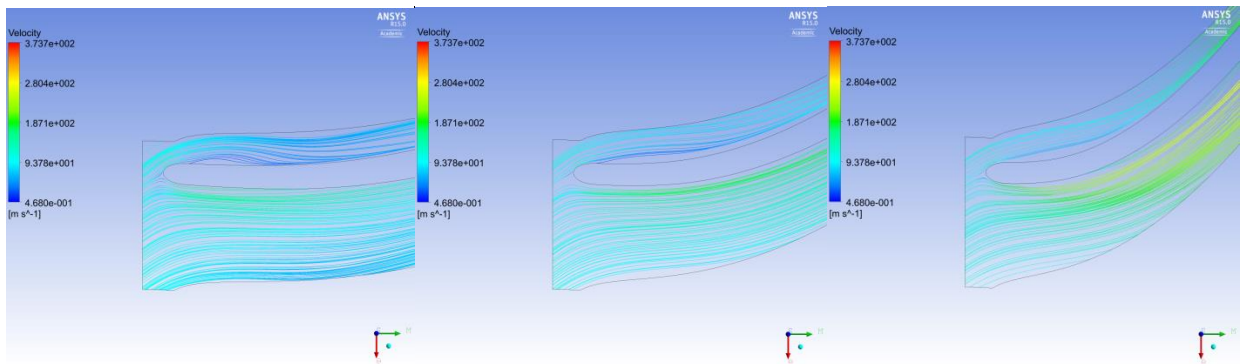


Figure 5.29 Streamlines in blade-to-blade view at spans of 0.1, 0.5 and 0.9 for designs of  $n=7$

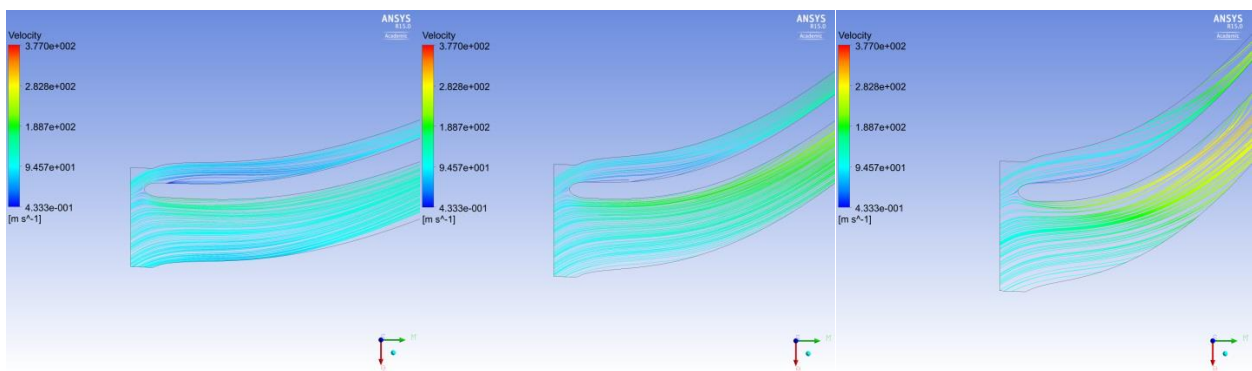


Figure 5.30 Streamlines in blade-to-blade view at spans of 0.1, 0.5 and 0.9 for designs of  $n=8$

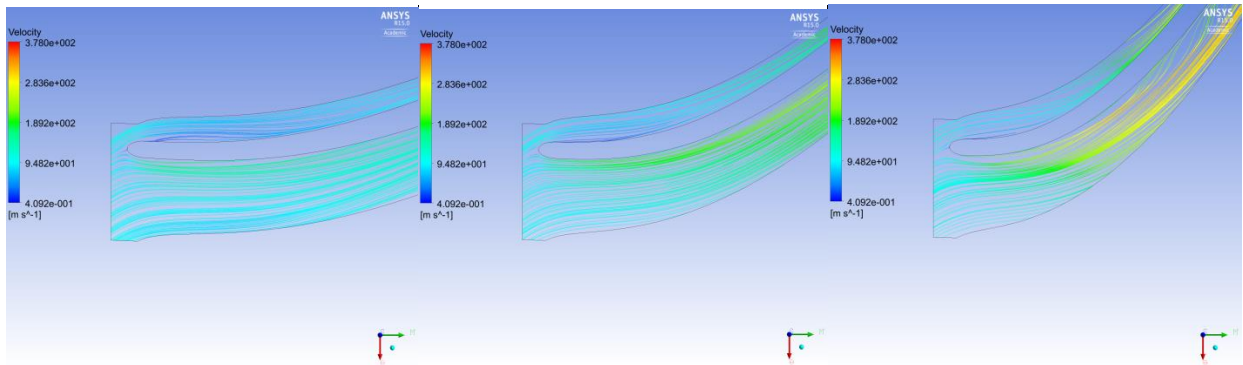


Figure 5.31 Streamlines in blade-to-blade view at spans of 0.1, 0.5 and 0.9 for designs of  $n=9$

### 5.5.5. Temperature and entropy contours on blade

A good distribution of temperature on the blade could result in a well-balanced thermal stress in the blade. It can also indicate less loss occurring near the blade. Figures 5.31 and 5.32 are the total temperature and entropy contours on the blade.

From the temperature contours it can be seen that near the inlet the temperature drops faster in the middle than the positions near the shroud and hub. This implies that losses occur near the shroud and hub on the blade which can be seen in Figure 5.31 and Figure 5.32.

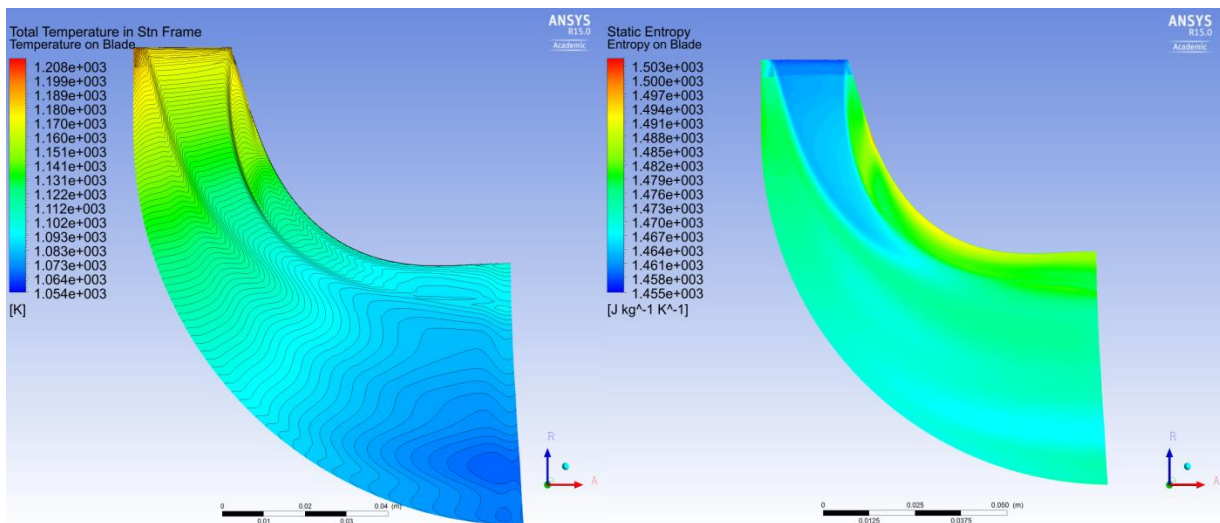


Figure 5.32 Total temperature and entropy on blade for  $n=5$



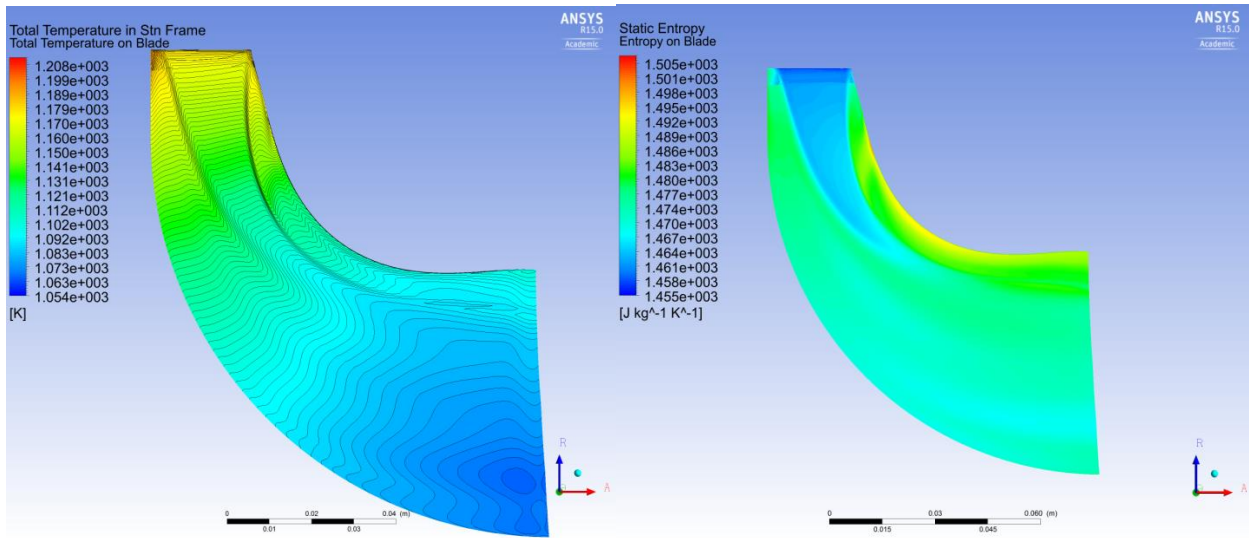


Figure 5.33 Total temperature and entropy on blade for n=6

In the right figure of Figures 5.31 and 5.32, at positions that have higher entropy than the inlet losses are generated. Comparing the two figures, it is not obvious to decide which design is superior.

### 5.5.6. Pressure, temperature, entropy, and velocity on meridional surface

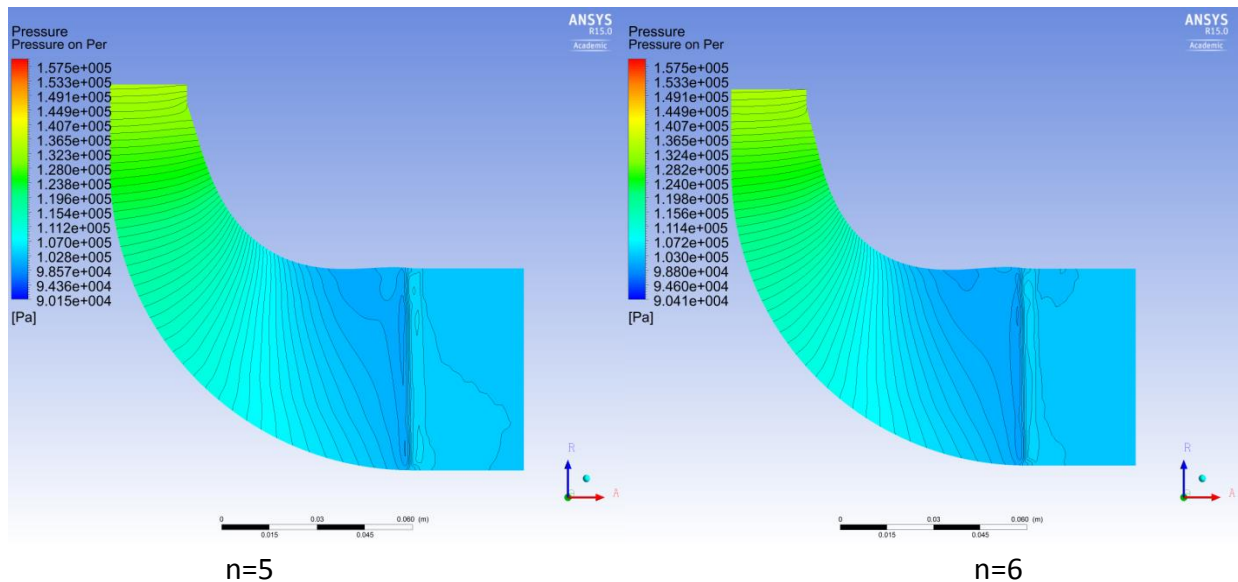


Figure 5.34 Pressure contour on meridional surface

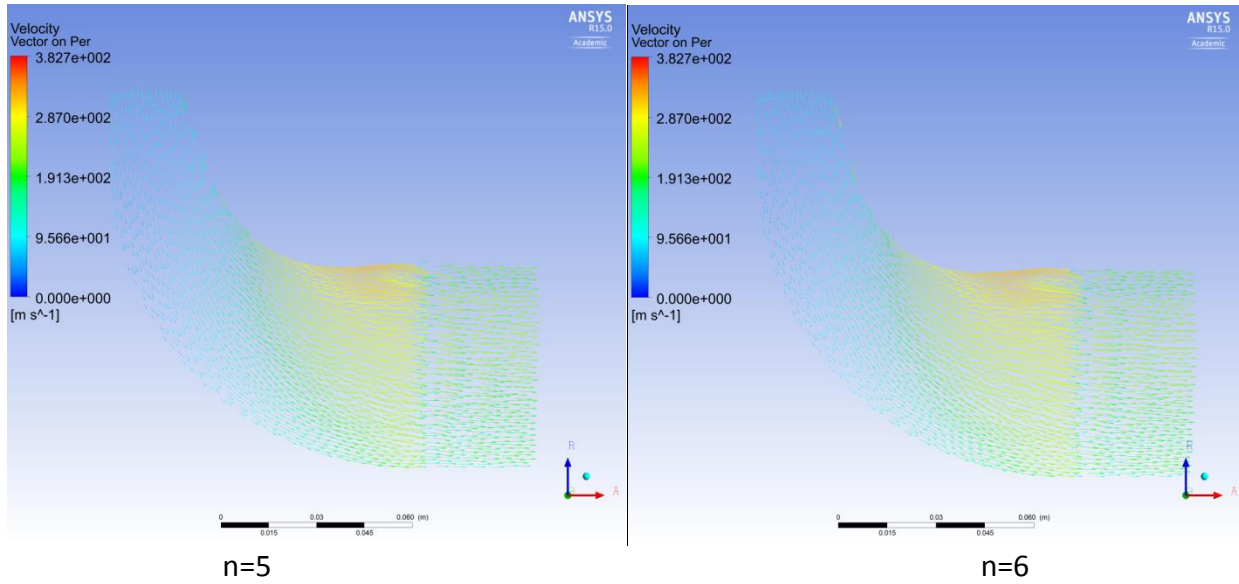


Figure 5.35 Velocity vectors on meridional surface

Figures 5.33 to 5.36 compare the results of the flow on the meridional surfaces, including pressure contours, velocity vectors, temperature contours, and entropy contours.

In Figure 5.33, the pressure contour looks more balanced on the meridional surface of design with  $n=5$  than the contour of design with  $n=6$ , because areas of low pressure appear near the shroud and outlet for the design of  $n=6$ .

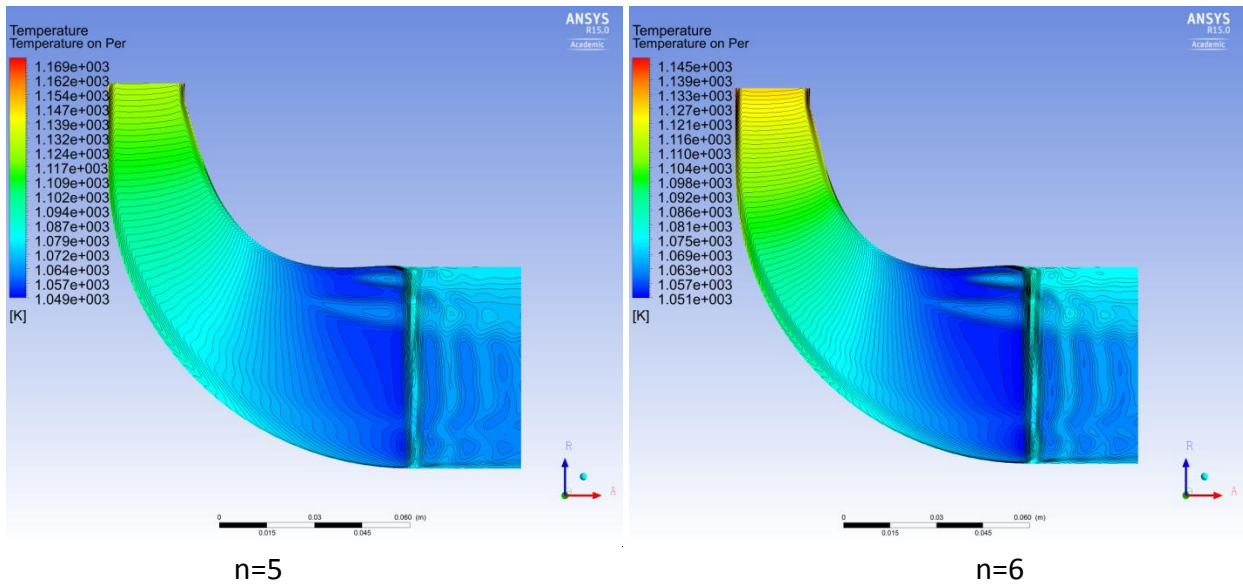


Figure 5.36 Temperature contours on meridional surface

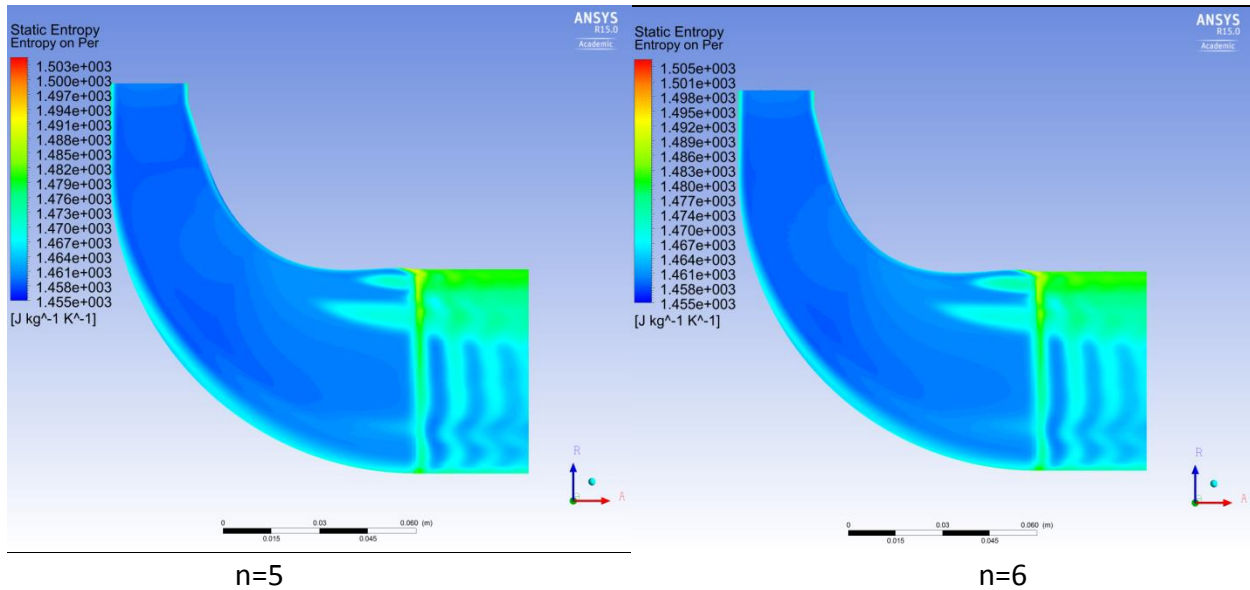


Figure 5.37 Entropy contours on meridional surface

Figures 5.34 and 5.35 cannot conclude which model performs better. In Figure 5.36, the entropy in sum accumulated all over the meridional surface of the design of  $n=5$  should be slightly smaller than the other design. So, there should be less losses in the design of  $n=5$  which coincides the CFD analysis results in Table 5.12.

Therefore, the model with polynomial shroud profile with power of 5 is chosen for the next step, where the shroud profile will be modified.

### 5.5.7. Modification of meridional shroud profile

Figure 5.37 shows the modification on the shroud profile based on the polynomial profile with power of 5. The profile is converted to Bezier curve which is easier to adjust the shape of the profile to smoothly connect ends of inlet and outlet. The profile tries to turn the direction more gradually and avoids flat curve near the outlet.

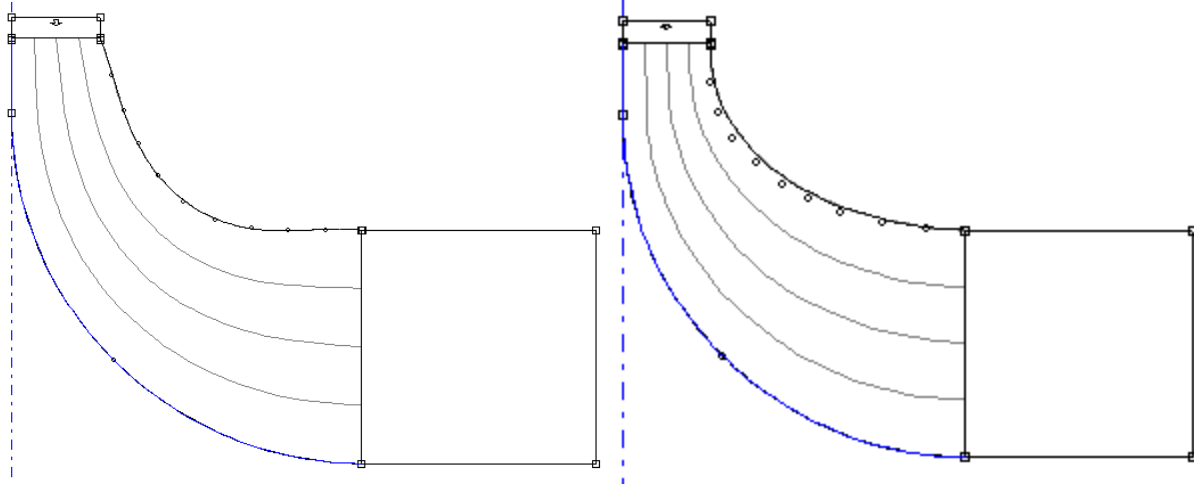


Figure 5.38 Modification of meridional shroud profile on the design of  $n=5$

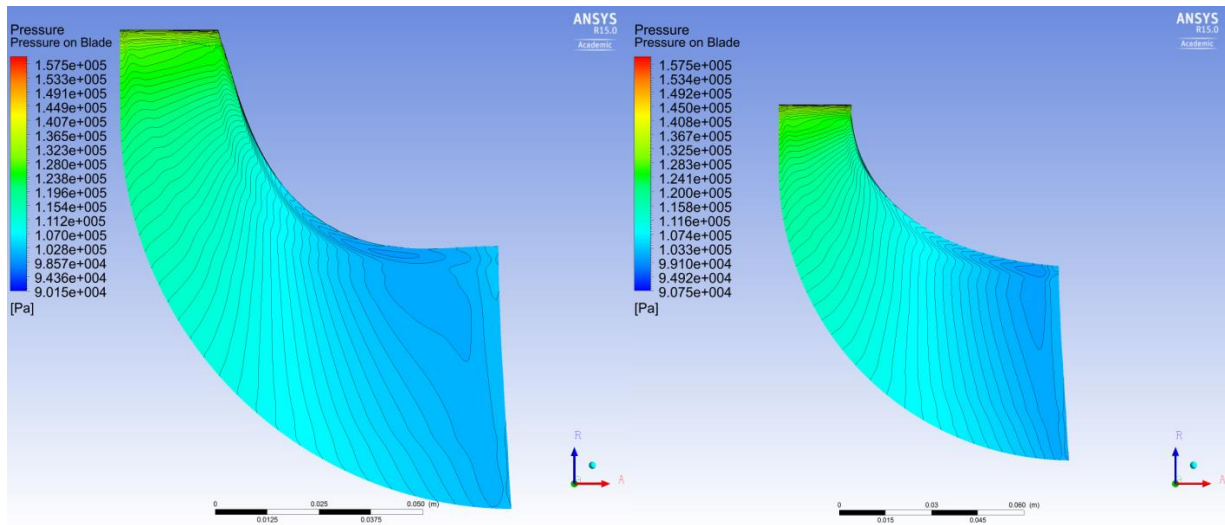


Figure 5.39 Pressure contours on the blade for the modified model

In Figure 5.38, the pressure distributed on the blade is significantly improved. The low pressure area is moved nearly to the exit. The area is smaller and pressure gradient is less aggressive.

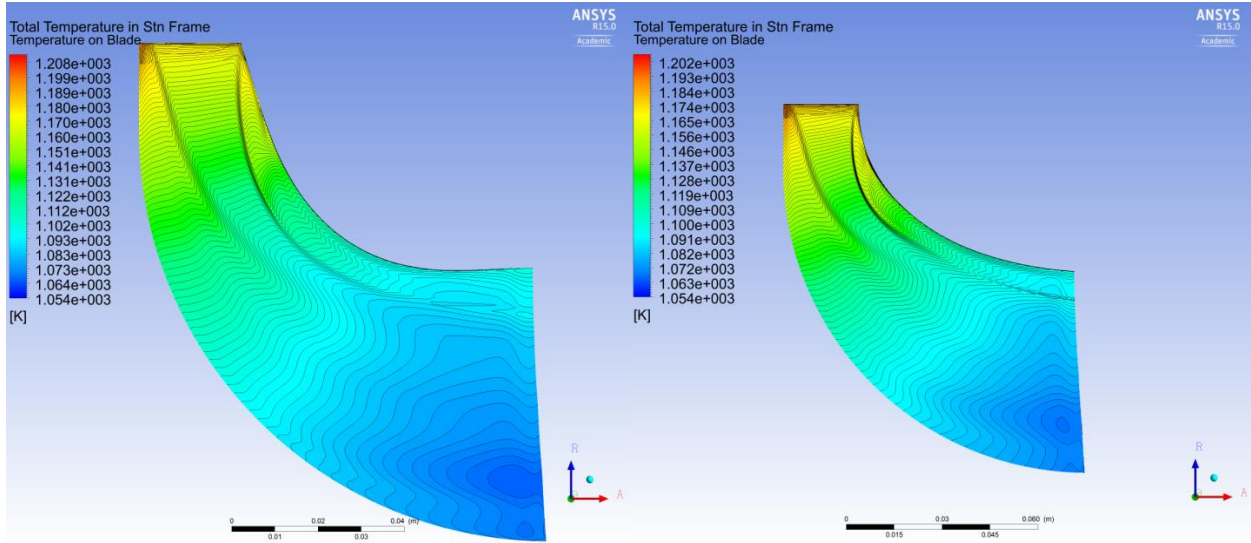


Figure 5.40 Temperature contours on the blade for the modified model

Figure 5.39 presents a better temperature pattern on the blade of the modified design. However, Figure 5.40 does not show a significant improvement in the entropy contour on the blade.

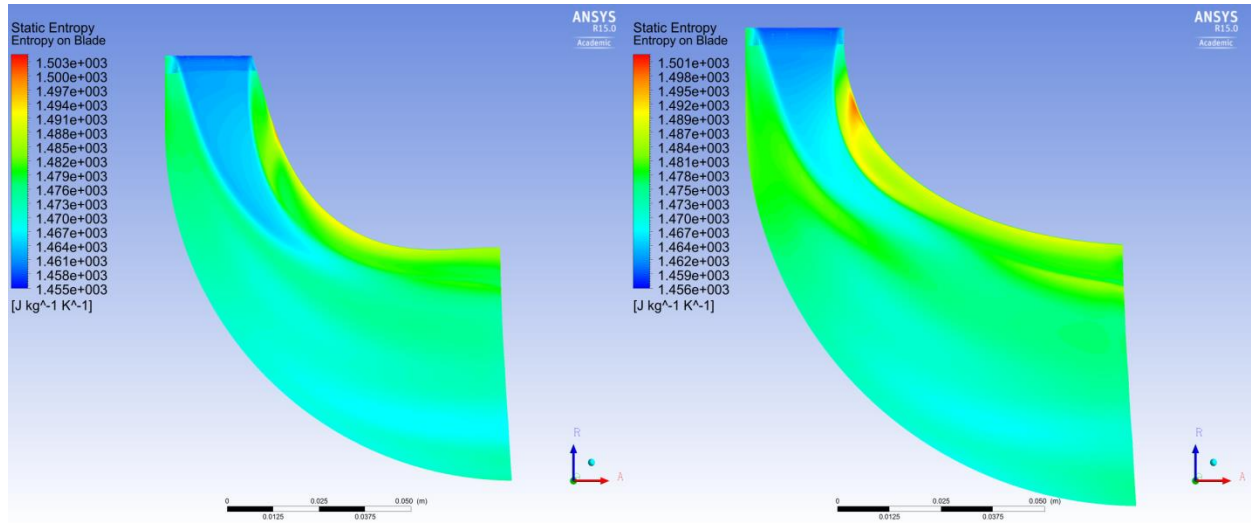


Figure 5.41 Entropy on blade for the modified model



Figures 5.41 to 5.44 show considerable improvements in the pressure, temperature, and entropy temperatures. The cumulated entropy increase cumulated over the meridional surface is smaller than the original design.

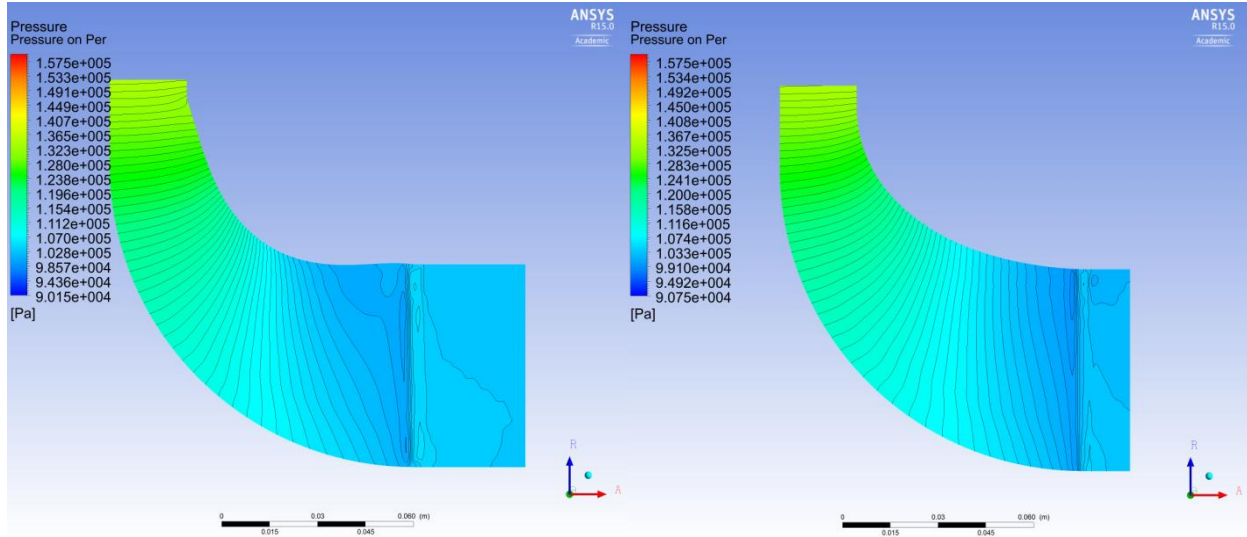


Figure 5.42 Pressure on meridional surface

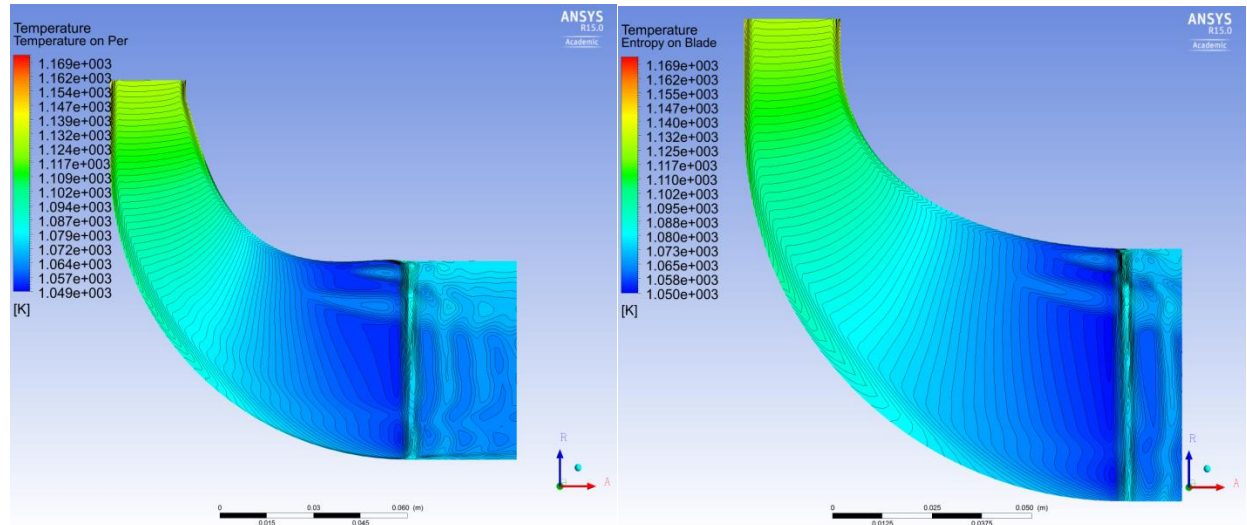


Figure 5.43 Temperature on meridional surface

Table 5.13 CFD Analysis results for the modified design

	$T_5$ , K	$T_{5t}$ , K	$P_5$ , kPa	$P_{5t}$ , kPa	$\eta_{rtt}$ , %	$\eta_{rts}$ , %	$\eta_{nrts}$ , %	$\eta_{nrts}$ , %
n=5	1064.64	1070.25	102.16	104.43	94.64	90.07	91.70	87.41
Modified design	1064.81	1070.35	102.33	104.57	94.83	90.29	91.87	87.61

Table 5.13 lists the CFD analysis results for the modified design. The results of the models are close to each other. The exit temperature becomes slightly higher than the exit temperature of the original design, but both total-to-total and total-to-static efficiencies are slightly improved as well.

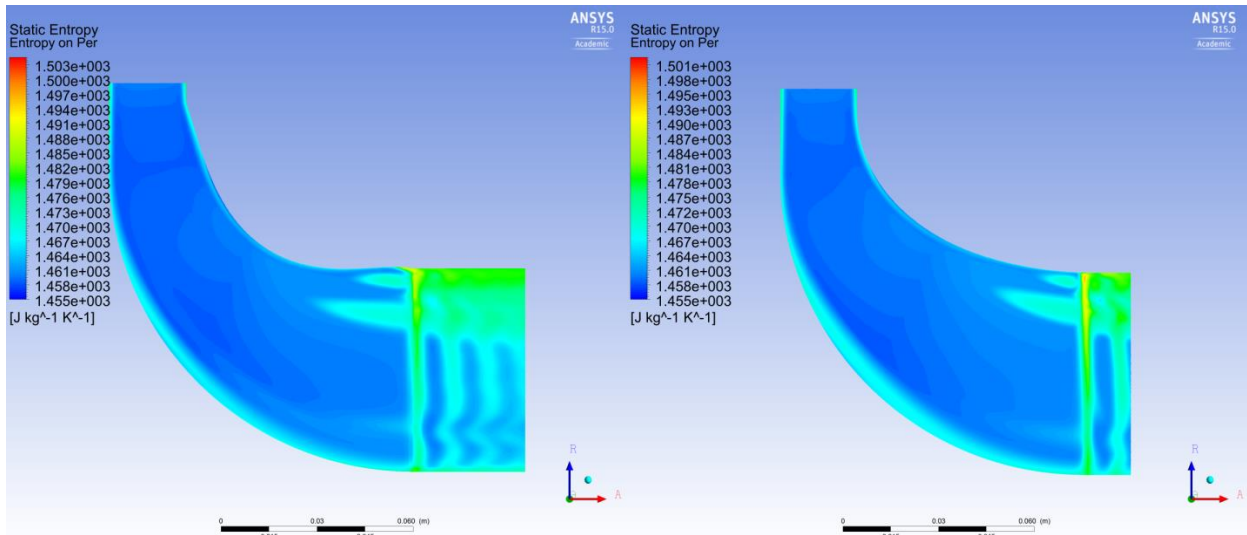


Figure 5.44 Entropy on meridional surface

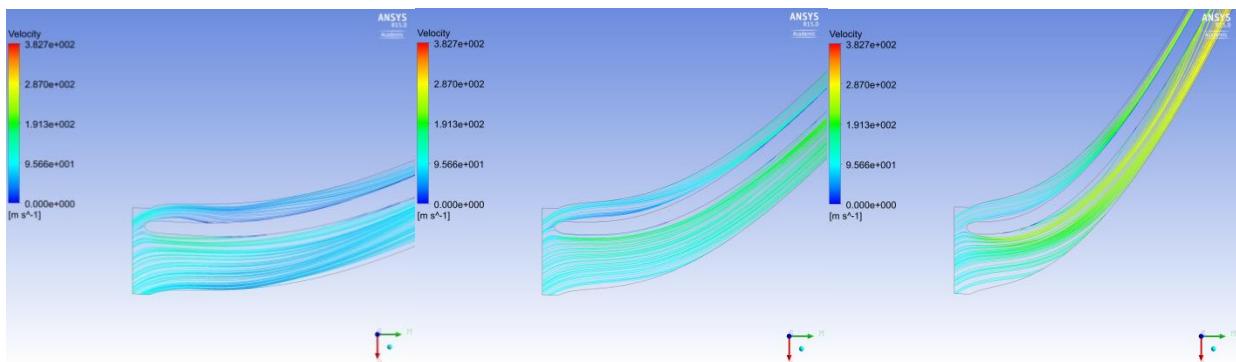


Figure 5.45 Streamline in blade-to-blade view at span of 0.1, 0.5, and 0.9

Compared to Figure 5.26, the streamlines in blade-to-blade view are significantly improved as well. In general, the modified design has improved the performances of the turbine. Nevertheless, there must be a way to further optimize the shroud profile to obtain the

best pressure and temperature contours on the blade. The theoretical study on the shroud profile will be conducted in the future.

### 5.6. Comparison with generalized stage performance chart for design

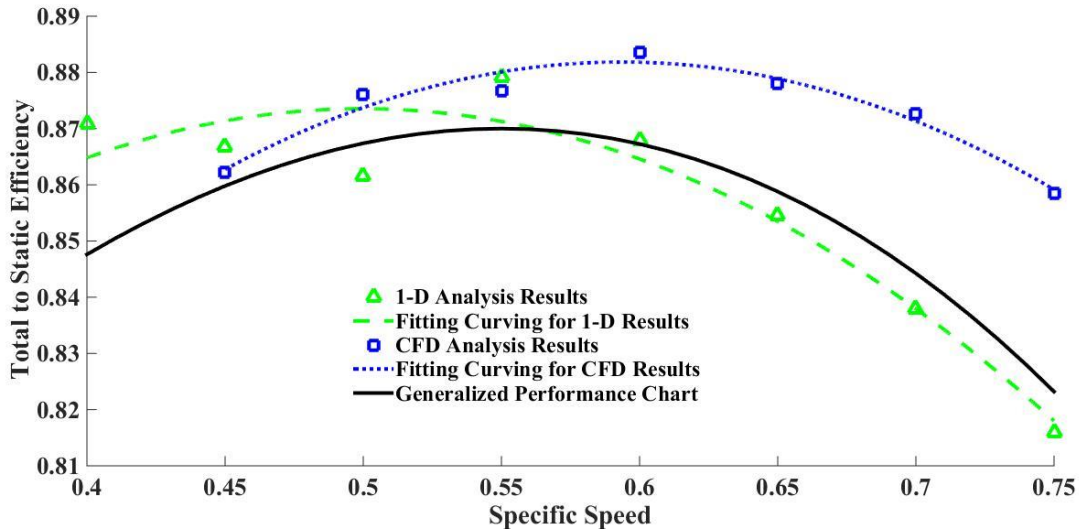


Figure 5.46 Comparison between the designs and generalized performance chart

The model was based on the specific speed of 0.55 that is assumed to be the optimum point for the highest efficiency. However, same method is utilized to generate models based on other specific speed to compare with the generalized performance chart in Equation 1-23. 1-D analysis results are near the curve, and the efficiency of the design of 0.55 specific speed is the optimum design point. CFD analysis yields in higher efficiencies than the prediction chart and the optimum specific speed is between 0.55 and 0.6. The designs of lower specific speeds also have high efficiencies. Nevertheless, based on the same method as in Equation 5-22, the inlet flow will be too tangential which not recommended if the absolute inlet flow angle is lower than  $15^\circ$  when the specific speed is smaller than 0.544. Besides, the size of the rotor may be too large for the system, the space of which is limited.



## 5.7. Performances of the turbine with different working fluids

Table 5.14 The performances of the turbine with different combinations of working fluids

	Propane without recuperator	Propane with recuperator	Ethane without recuperator	Ethane with recuperator	Methane without recuperator	Methane with recuperator
$T_5, K$	1064.81	1065.39	1064.51	1065.35	1064.33	1065.35
$T_{5t}, K$	1070.35	1070.66	1070.18	1070.63	1070.04	1070.64
$P_5, kPa$	102.325	103.931	102.205	103.915	102.109	103.913
$P_{5t}, kPa$	104.568	106.038	104.498	106.024	104.417	106.024
$\eta_{rtt}, \%$	94.83%	94.87%	94.85%	94.87%	94.84%	94.87%
$\eta_{rts}, \%$	90.29%	90.51%	90.21%	90.50%	90.17%	90.50%
$\eta_{nrts}, \%$	91.87%	91.97%	91.89%	91.97%	91.85%	91.97%
$\eta_{nrts}, \%$	87.61%	87.88%	87.54%	87.87%	87.48%	87.87%

The turbine is analyzed also with other kinds of working fluid combinations. When the gases flow into the turbine are produced by the systems with recuperators, the outlet temperatures do not change much indicating that the work outputs almost remain same. Therefore, the future implementation of recuperator or change of fuels will not influence the performance of the turbine.

## 5.8. Off-design analysis

The off-design analysis is based on the flowing assumptions:

1. The inlet flow angle remains same in off-design conditions
2. The inlet total temperature and outlet total pressure must be known

Figure 5.46 shows the flow chart of the off-design analysis. The objective of the program is to find the inlet velocities that can yield the same inlet conditions after going through the 1-D analysis so that the inlet pressure can be obtained.

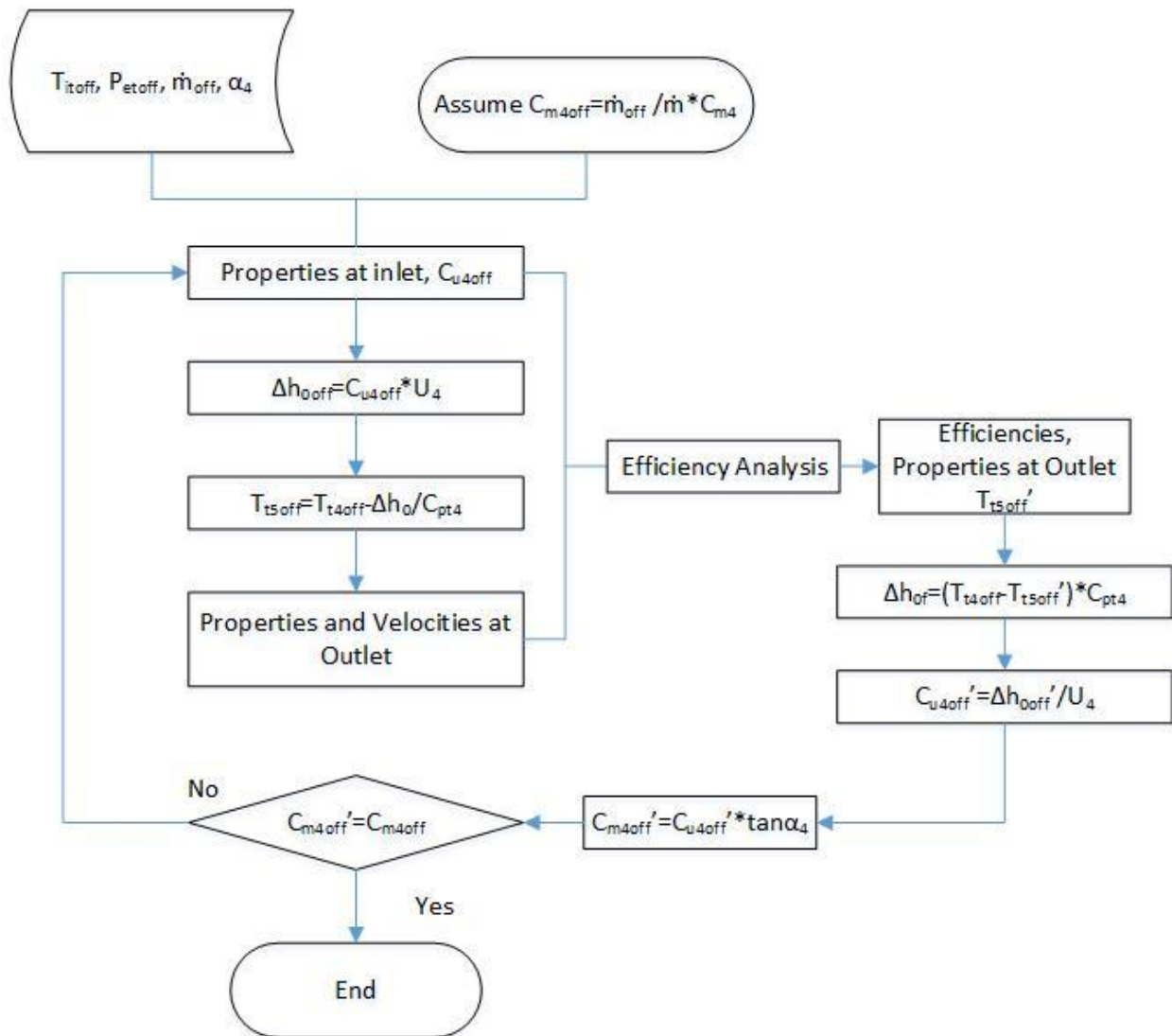


Figure 5.47 Flow chart of off design analysis

CFD analysis is also performed to compare with the 1-D analysis. The mass flow has limit a when the flow is choked. The highest mass flow is about 1.8 times of the designed mass flow. Figure 4.47 is the pressure ratios for different mass flows. To increase the mass flow, the inlet pressure must be higher, while less inlet pressure is required when the flow is smaller. 1-D and 3-D analyses coincide well in the range of normalized flow of 0.8-1.5.

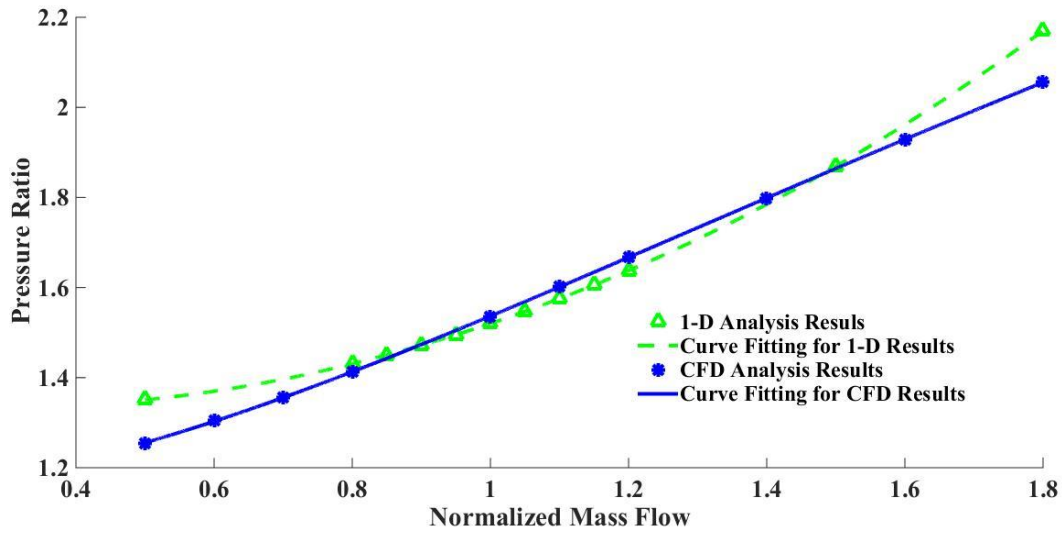


Figure 5.48 Pressure ratios at different mass flow

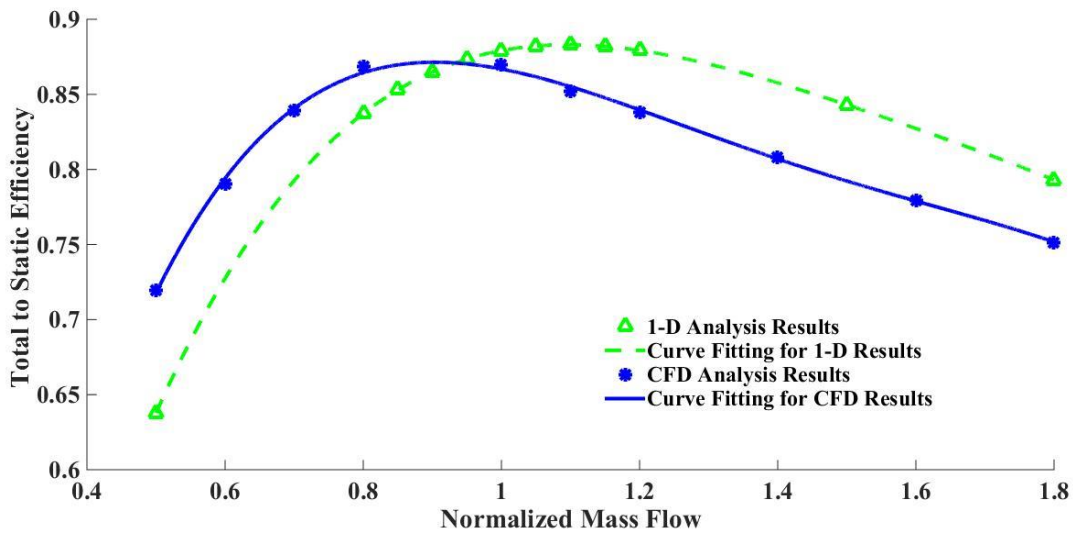


Figure 5.49 Total to static efficiencies at different mass flow

The total-to-static efficiency curves by 1-D analysis and CFD do not coincide well, however it is impossible to tell which curve is more accurate without comparing with the experimental data.

In the figure of total-to-total efficiency, the differences between the results by the two analysis methods are smaller than the results of total-to-total efficiencies.

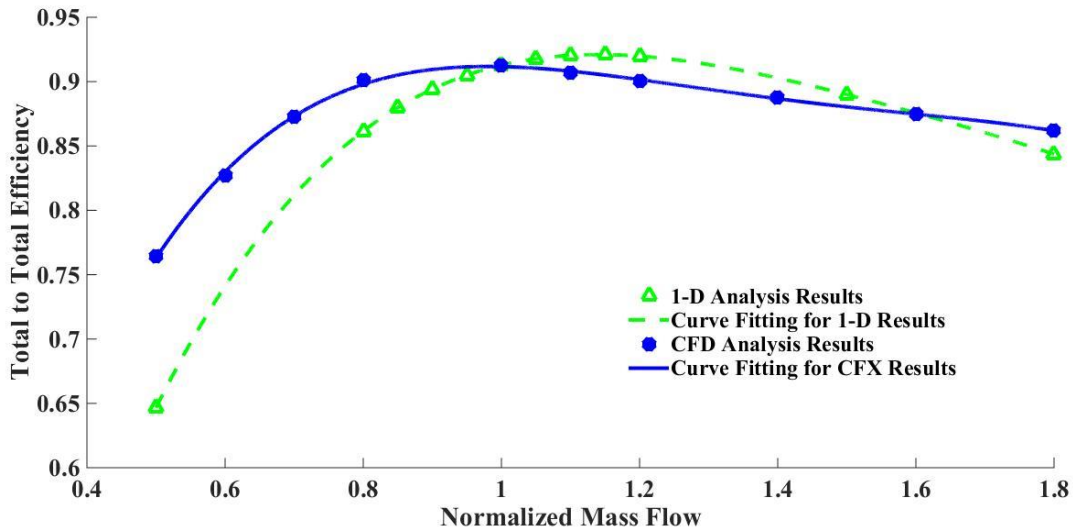


Figure 5.50 Total to total efficiencies at different mass flow

In the next section where the performance of the system is analyzed in off-design conditions, the total-to-total efficiency curve from CFD simulation is used. The curve is obtained by applying polynomial fitting curve with power of 4 on the CFD analysis results.

## 5.9. Performance analysis of the biogas-solar hybrid system with the designed turbine

### 5.9.1. The efficiencies of the system with the designed turbine

Table 5.15 System efficiencies at the design point

	Thermal efficiencies	Fuel efficiencies
System without recuperator	0.082263	0.08517
System with recuperator	0.295448	0.33673

The thermal efficiency and fuel efficiency are calculated with Equation 4-2 and 4-3. The results of efficiencies are higher than the efficiencies calculated in Chapter 4, because the assumed efficiency is 0.8 in Chapter 4. In addition, the efficiencies of the system with recuperator are significantly improved by the recuperator.

### 5.9.2. The efficiencies of the system at off-design conditions

Figure 5.50 is the process of off-design analysis on the system. The inlet temperature is assumed to remain same at off-design conditions. Then with the fitting curving from the CFD analysis, pressure ratio and efficiency of the turbine can be obtained. According to the mass flow and the inlet pressure of the turbine, the efficiency of the compressor at the off-design condition is now obtained. The red lines in Figure 5.51 can look up the efficiencies of the compressor in various off-design conditions. However, the upper boundary of mass flow is 110lb/min, so the range of normalized mass flow is set within 0.7-1.1 times of the designed mass flow.

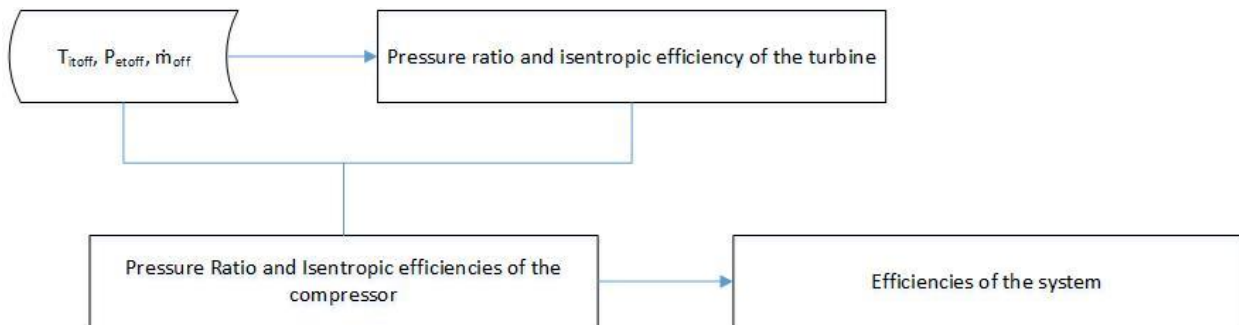


Figure 5.51 Scheme of the calculation of the efficiencies at off-design conditions

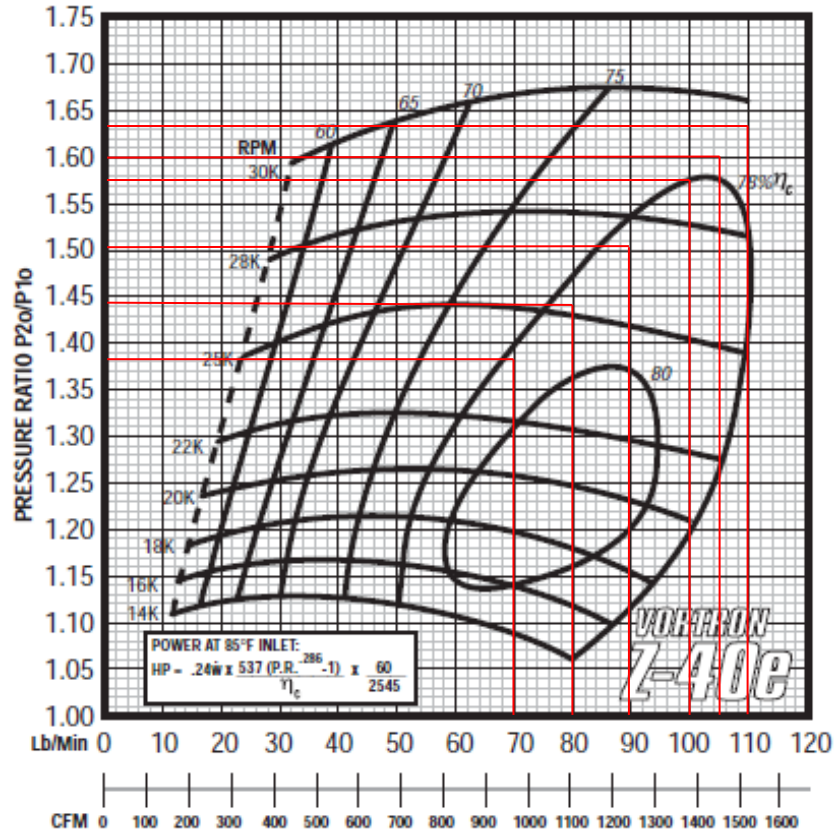


Figure 5.52 Characteristics of the compressor with lines to seek its performance

Figures 5.52 and 5.53 are the efficiencies of the system at different mass flows. As the mass flow increases, the efficiency of the system rises as well, because the pressure ratio of the system is higher too. A higher pressure ratio in the Brayton cycles can marginally improve the systematic efficiencies, and it can sometimes even overcome the slight decrease in efficiencies of the turbine and compressor.

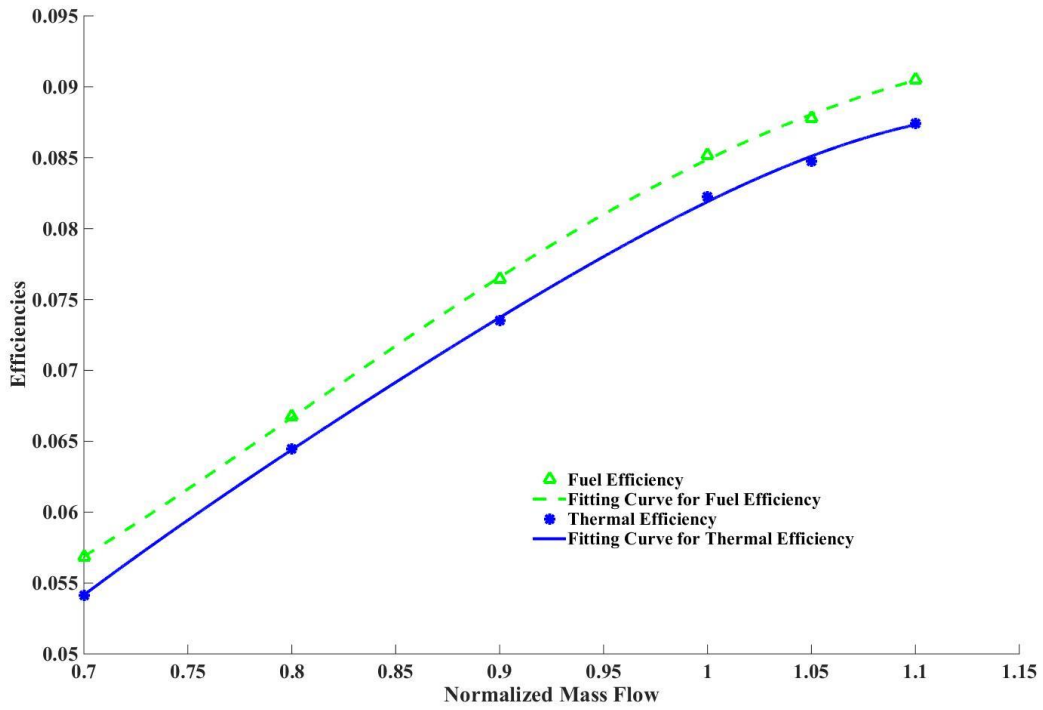


Figure 5.53 Performances of the system without the recuperator at various mass flows

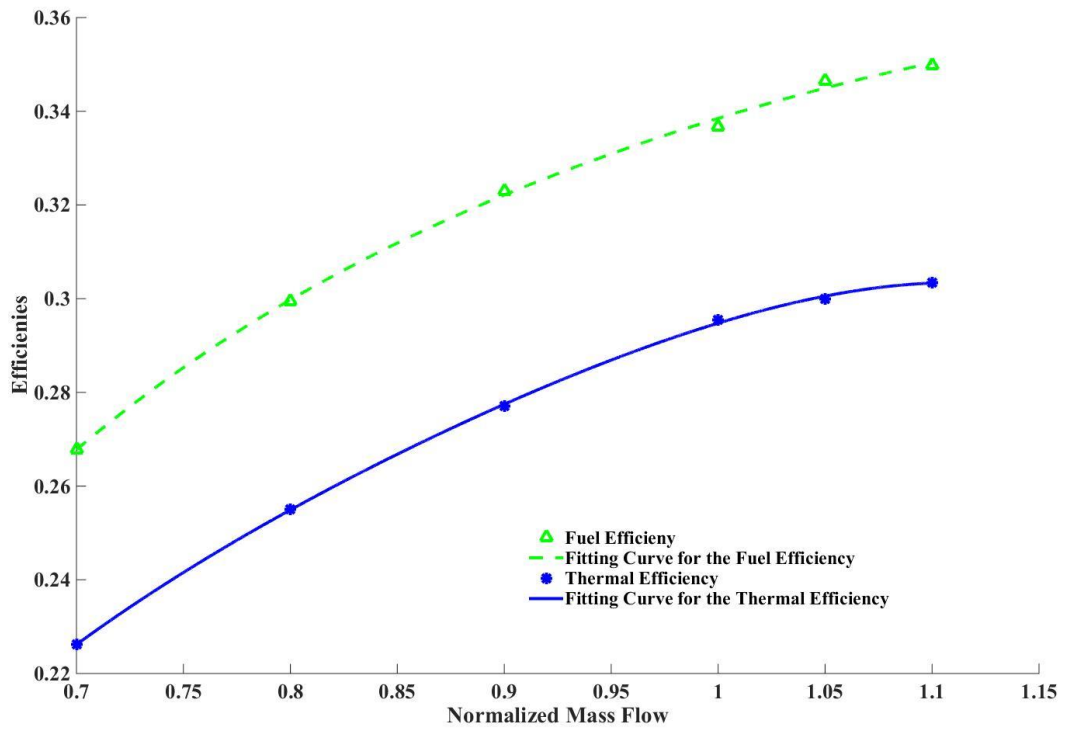


Figure 5.54 Performances of the system with the recuperator at various mass flows

## 5.10. 1-D optimization on the inlet velocities

### 5.10.1. Study on inlet absolute flow angle

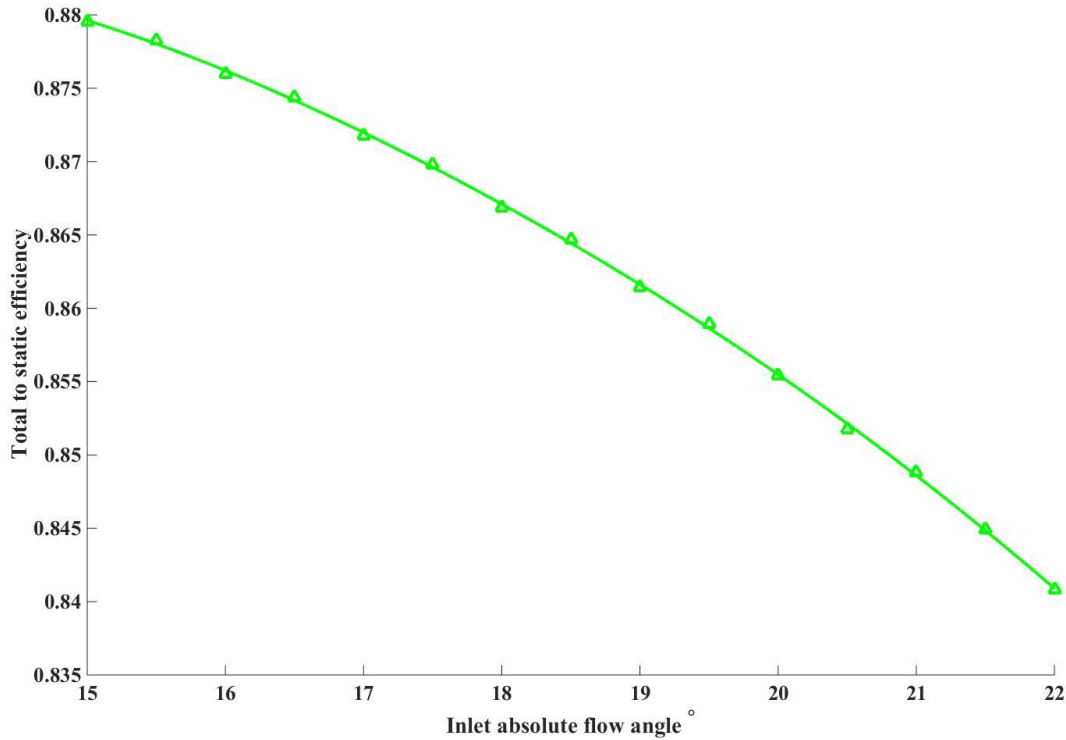


Figure 5.55 Total to static efficiencies of different turbines with different inlet absolute flow angles

Figure 5.54 and Figure 5.55 are efficiencies of the turbines from 1-D analysis with different inlet absolute flow angles ranging from 15° to 22°. When the inlet absolute flow angle increases from 15° to 22°, the total to static efficiency decreases and the total to total efficiency approximately reaches an optimum value of 91.3% near 15.56°. Therefore, the flow angle of 15.1° generated by Equation 5-22 is a good guess based on 1-D analysis results.



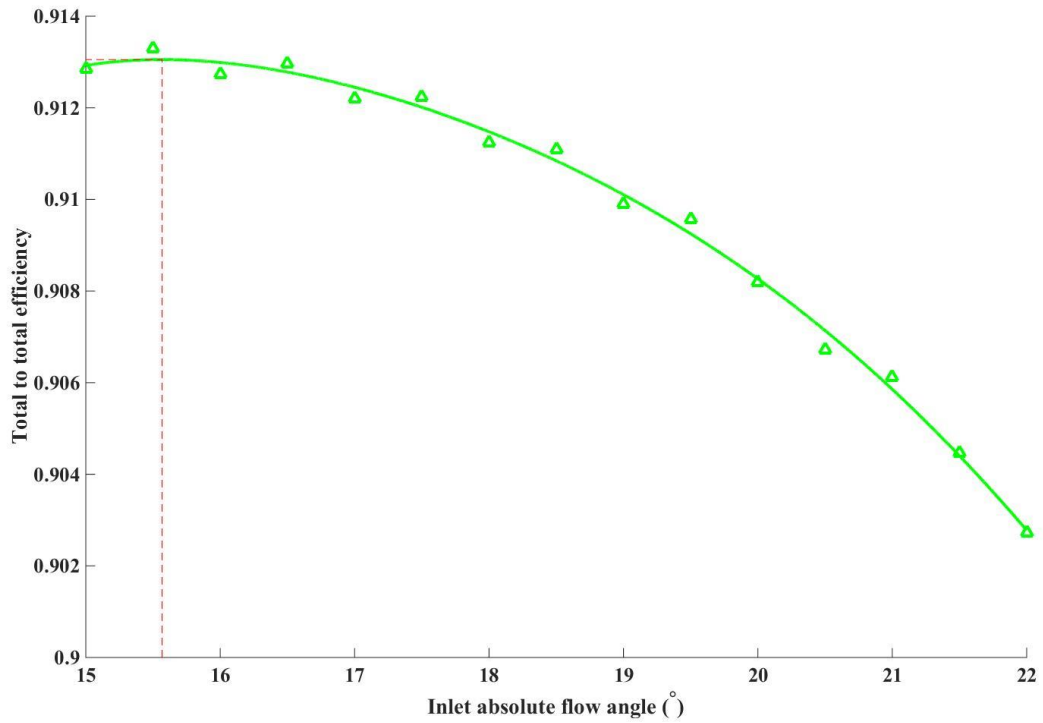


Figure 5.56 Total to total efficiencies of different turbines with different absolute inlet flow angles

### 5.10.2. Study on inlet relative flow angle

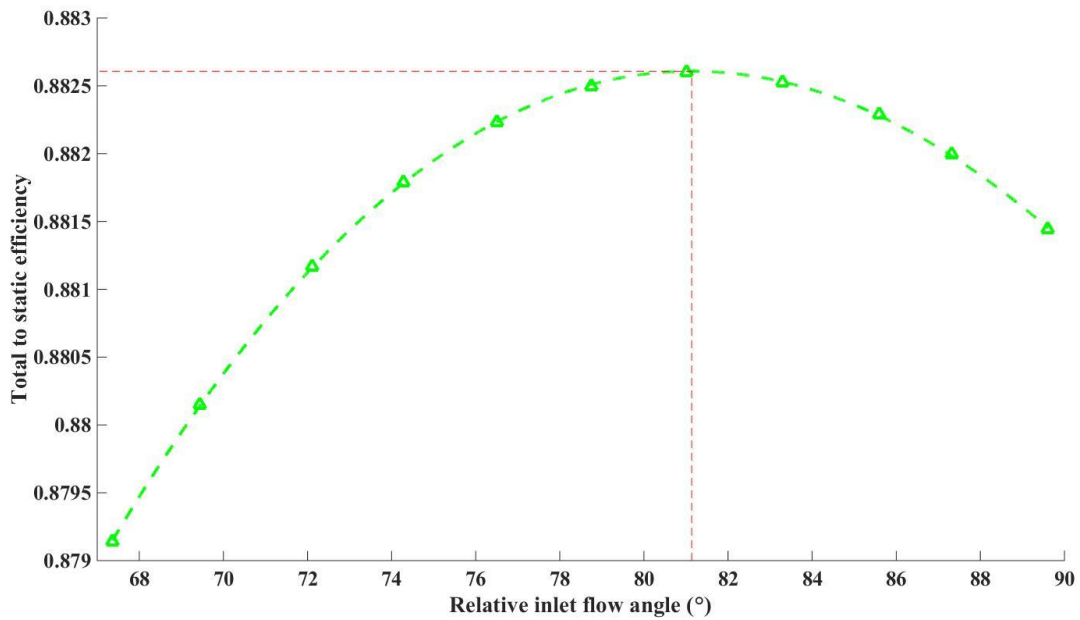


Figure 5.57 Total to static efficiencies of different turbines with different absolute inlet flow angles

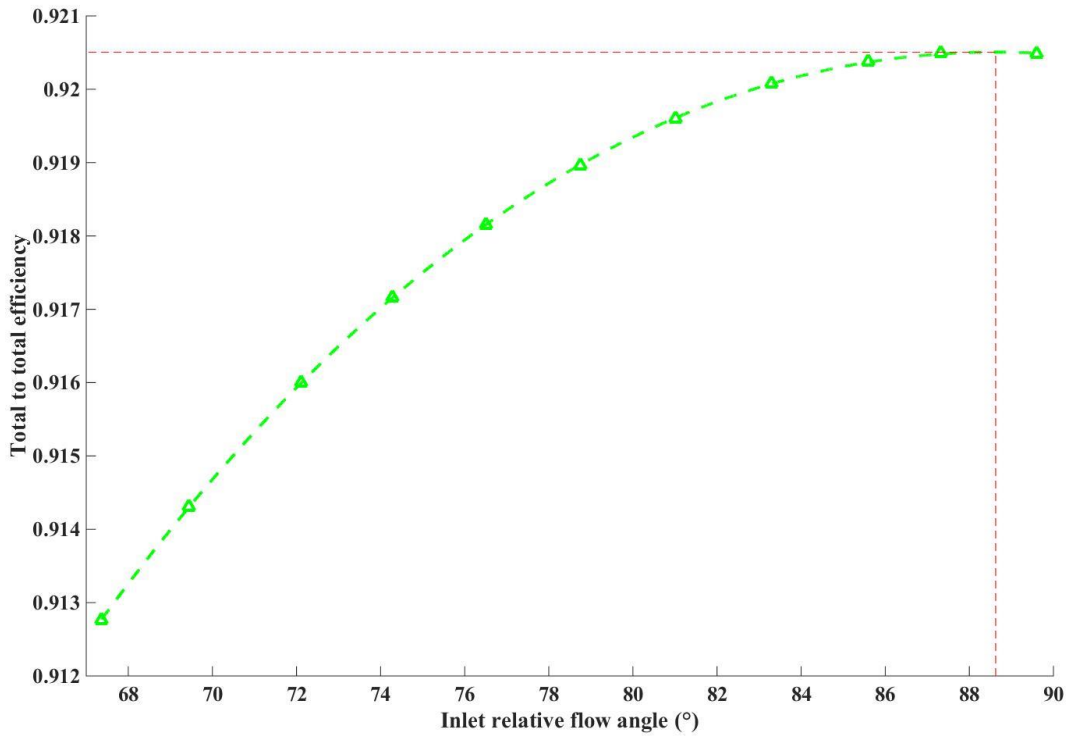


Figure 5.58 Total to total efficiencies of different turbines with different absolute inlet flow angles

Different turbines with relative inlet flow angles ranging from 67° to 89° are designed and analyzed with the 1-D loss model, while the other geometries are generated with the same method, including the 15.1° inlet absolute flow angle based on Equation 5-22 for a specific speed of 0.55.

1-D analysis results show that the best total to static efficiency is at 81.14° inlet relative flow angle and the optimum total to total efficiency is at 88.63° inlet relative flow angle. The efficiencies are improved approximately by 1% compared to the first design.

### 5.10.3. CFD analyses of the turbine with optimized inlet flow angle

Table 5.16 1-D geometry with the relative inlet flow angle for the best total to static efficiencies

		Propane without recuperator
Rotor radius	$r_4$ (m)	0.1363
Rotation Speed	rpm	24819.4
Outlet hub radius	$r_{5h}$ (m)	0.0252
Outlet shroud radius	$r_{5s}$ (m)	0.0874
Inlet blade angle	$\beta_{4b}$ ( $^\circ$ )	105.02
Inlet flow angle	$\alpha_4$ ( $^\circ$ )	15.1
Inlet width	$b_4$ (m)	0.0243
Rotor axial length	$\Delta z_R$ (m)	0.0933
Number of blades	Z	22
Outlet shroud blade angle	$\beta_{5sb}$ ( $^\circ$ )	25.22
Outlet hub blade angle	$\beta_{5hb}$ ( $^\circ$ )	58.52
Inlet blade thickness	$t_{b4}$ (m)	0.0055
Outlet blade thickness	$t_{b5}$ (m)	0.0027

A new rotor is designed and analyzed with CFX to validate the optimized inlet flow angle. The inlet absolute flow angle is still  $15.1^\circ$  because it is decided by Equation 5-22 with a specific speed of 0.55. The inlet relative flow angle is chosen to be  $81.14^\circ$  where the total to static efficiency is the peak of the fitting curve in Figure 5.56. The other geometries are obtained with the same method for the first design. The same analyzing process shows that the polynomial shroud profile with power of 5 is the best among the other options. An optimization on the shroud with the same ideal in the former sections is performed, and the model is analyzed in CFX as well. The CFD analysis results are presented in Table 5.17.

The design with polynomial shroud profile is slightly improved, and an extra modification on the shroud profile yields in even higher efficiencies. Therefore, it can be concluded that the best inlet relative flow angle is not necessarily near  $70^\circ$ , and the ideal of

modifying the shroud profile is reasonable. Nevertheless, the theoretical method to obtain the optimum shroud profile has not been found and requires future studies on it.

Table 5.17 CFX analysis results for the turbines with optimized inlet relative flow angle

	Polynomial curve with n=5	Optimized curve based on polynomial with n=5
$\dot{m}$ , kg/s	0.77121	0.77121
$T_5$ , K	1063.59	1062.08
$T_{5t}$ , K	1069.1	1067.82
$P_5$ , kPa	102.350	101.914
$P_{5t}$ , kPa	104.584	104.235
$\eta_{rtt}$ , %	95.45%	95.89%
$\eta_{rts}$ , %	90.91%	91.19%
$\eta_{nrts}$ , %	93.02%	93.46%
$\eta_{nrts}$ , %	88.72%	89.00%

### 5.11. Summary

In this chapter, 1-D designs are performed based on the inlet conditions of the turbine from theoretical calculation results in Chapter 4. 1-D and 3-D models are generated according to the Aungier's method. Primitively, seven shroud profiles are defined by polynomial profiles from power of 3 to 9. For the profile with power of 5, the mean quasi-normal is closest to the average of the inlet and exit areas than the other designs. In addition, 3-D analysis results showed that the preliminary design with polynomial shroud file of power of 5 has the best performances among all the choice as well.

1-D and 3-D analysis results, such as velocity triangles, efficiencies, and properties, showed good agreements with the design although differences exist. Upon the best preliminary design, the shroud profile is optimized to be smoother. The modification results in better streamlines, and pressure and temperature contours on the blade and the meridional surfaces.

Other designs of different specific speeds are generated with the same method and analyzed with 1-D loss model and CFD. The results show the similar trends as the generalized performance chart provided by Aungier. The designs of lower specific speeds also have high efficiencies. Nevertheless, based on the same method as in Equation 5-22, the inlet flow will be too tangential which not recommended if the absolute inlet flow angle is lower than  $15^\circ$  when the specific speed is smaller than 0.544. Besides, the size of the rotor may be too large for the system, the space of which is limited.

The off-design performances are calculated with 1-D loss model and CFD. The results show reasonable trends but 1-D and 3-D results do not coincide well. However, only experimental data are able to tell which curve is more accurate.

In addition, the hybrid system's performances are analyzed again with the CFD simulation results of the turbine. The off-design performances are also analyzed based on the CFD performance curve of the turbine. As the mass flow increases, the efficiency of the system rises as well, because the pressure ratio of the system is higher too. A higher pressure ratio in the Brayton cycles can marginally improve the systematic efficiencies, and it can sometimes even overcome the slight decrease in efficiencies of the turbine and compressor.

## CHAPTER 6. CONCLUSIONS

### 6.1. Conclusions from the research of pump as turbine

Four pumps are tested in their pump operation mode and turbine mode. Their best efficiency performances, specific speed, and specific diameter are obtained from the testing data. This research innovatively proposed a prediction method that is based on specific speed and specific diameter. The new method is obtained by curve-fitting the specific speeds, specific diameters and efficiency ratios in the pump mode and turbine mode. The fitting curves are then able to predict performances of other pumps in their turbine mode.

As a result, the relation between the specific speeds in pump mode and turbine mode are approximately linear. For specific diameters in two modes, the correlation tends to be linear. However, pump 3's specific diameter deviates a little bit (3.27%) from the straight fitting curve, because its design is different from the other three pumps. Nevertheless, a small error in specific diameter can result in a much larger error in head and flow prediction. The best way to minimize the error for the method proposed in this thesis is creating specific speed and specific diameter correlations for each family of pumps that meet the requirements proposed in the previous sections. This will require a lot of future tests and experiments.

The ratio between the efficiencies of two running modes increases with the pump's specific speed in a roughly linear trend. The errors of efficiency prediction are smaller than 5%.

With predicted specific speed and diameter, the head and flow in turbine mode can be estimated. The errors of prediction results for pump 1 are smaller than 1%. The pump 2's prediction errors of head and flow are 3% and 4% and pump 4's errors are near acceptable 5%

limits. However, pump 3's errors are nearly 10% because it is geometrically modified, thus it does not meet the requirements in Section 3.3.2. Therefore, the new method based on specific speed and specific diameter may be exclusive, which means it could be inaccurate for a different pump design. Hence, future tests for different types of pumps are required.

The new method is compared with 9 previously published prediction methods. Most previous methods are not accurate for the four tested pumps (at least 20% error). All of the previous experimental correlations are invalid. However, Stepanoff's and Sharma's methods are valid near the specific speed of 0.83 rad/s (near 5% error). Yang's method is acceptable around a specific speed range between 1.20 rad/s and 1.51 rad/s. The results clearly reveal that all the prediction methods (without detailed geometry) are only valid conditionally. Special prediction equations should be obtained for each range of specific speed and each type of pump design from testing data.

In addition to comparison with previous prediction methods, the new method is also tested with published experimental data. Data from the four pumps are applied on the prediction methods. The errors for the pump with  $N_{sp}=1.06$  and  $D_{sp}=1.56$  are about 8% because the specific speed and specific diameter are very close to the prediction curve proposed in this thesis. The prediction results for the other three pumps have enormous errors. This is not surprising because their specific speed and specific diameter are scattered away from the fitting curve proposed in this thesis. The inaccuracy at the same time verifies the necessity of more tests on other families of pumps with different ranges of specific speed and specific diameters.

## **6.2. Conclusions from the research of solar biogas hybrid system**

The theoretical analyses of the systems with and without recuperator conclude that higher efficiencies of the compressor and turbine will improve efficiencies of the system. The recuperator significantly increases the performances of the system and amplifies the benefits from the improvements of the compressor and the turbine. At last, the design point for the turbine is estimated as shown in Table 4.3. The pressure ratio of the system is a key factor that decides the performances of the system. For the system without recuperator, as the pressure ratio increases, the fuel efficiency and thermal efficiency go up as well. The work output reaches its peak when pressure ratio is around 5. For the system with recuperator, the system will reach its maximum fuel efficiency and thermal efficiency at the pressure ratio of 3.1, and the maximum work output is obtained at the pressure ratio of 5.24. At last, the design point for the turbine is estimated as shown in Table 4.3.

## **6.3. Conclusions from the design and analysis of the radial turbine**

In this chapter, 1-D designs are performed based on the inlet conditions of the turbine from theoretical calculation results in Chapter 4. 1-D and 3-D models are generated according to the Aungier's method. Primitively, seven shroud profiles are defined by polynomial profile from power of 3 to 9. For the profile with power of 5, the mean quasi-normal is closest to the average of the inlet and exit areas than the other designs. In addition, 3-D analysis results showed that the preliminary design with polynomial shroud file of power of 5 has the best performances among all the choice as well.

1-D and 3-D analysis results, such as velocity triangles, efficiencies, and properties, showed good agreements with the design although differences exist. Upon the best preliminary



design, the shroud profile is optimized to be smoother. The modification results in better streamlines, and pressure and temperature contours on the blade and the meridional surfaces.

Other designs of different specific speeds are generated with the same method and analyzed with 1-D loss model and CFD. The results show the similar trends as the generalized performance chart provided by Aungier. The designs of lower specific speeds also have high efficiencies. Nevertheless, based on the same method as in Equation 5-22, the inlet flow will be too tangential which not recommended if the absolute inlet flow angle is lower than  $15^\circ$  when the specific speed is smaller than 0.544. Besides, the size of the rotor may be too large for the system, the space of which is limited.

The off-design performances are calculated with 1-D loss model and CFD. The results show reasonable trends but 1-D and 3-D results do not coincide well. However, only experimental data are able to tell which curve is more accurate.

In addition, the hybrid system's performances are analyzed again with the CFD simulation results of the turbine. The off-design performances are also analyzed based on the CFD performance curve of the turbine. As the mass flow increases, the efficiency of the system rises as well, because the pressure ratio of the system is higher too. A higher pressure ratio in the Brayton cycles can marginally improve the systematic efficiencies, and it can sometimes even overcome the slight decrease in efficiencies of the turbine and compressor.

#### **6.4. Next steps of the project**

Scientific and engineering researches shall never be truly finished because problems cannot be perfectly solved and new problems will appear too as the researchers explore deeper

and wider from the original problems. This dissertation, as well, has not been perfectly finished. More efforts should be done by either the author or the successive researchers.

#### **6.4.1. Studies on the solar biogas hybrid system**

Experiments and tests shall be done in short future to study the performances of the system. Especially, the outlet properties of the burner or the inlet conditions of the turbine should be obtained by tests, which is the base for the real specification for the design of the turbine.

A recuperator can be either purchased or designed and manufactured in the future which would boost the performances of the system.

The designed radial turbine should be created tested in the system to verify the whole performances of the hybrid system. An axial turbine is another choice for the system, which can be designed and built in the future by successive researchers.

#### **6.4.2. Studies on the design and analysis of the radial turbine**

Besides the inlet flow angles, the sensitivity analyses on the other 1D geometries of the rotor should be supplemented in the future. The changes in performances as each 1D geometry is adjusted within reasonable ranges should be calculated so that they can be used to optimized design.

Methods to optimize the 3D curves of the blade may be obtained from theoretical studies. These methods, if successfully found, would considerably improve the aerodynamic performances of the gas passage and the stability of the blade.

### **6.4.3. CFD simulations with different turbulence models**

In this dissertation, the CFD simulations use  $k-\omega$  method that does not require as refined meshes as SST method, but the simulations inevitably yield less accurate results in exchange for less computational resources (fewer CPU's and less running time). However, if more details of the flow are necessary to evaluate the design, SST method with well-refined meshes should be used in the future.

### **6.4.4. Structural analysis on the rotor**

The high rotation speed requires a robust structure of the rotor. In addition for a rotor of radial inflow turbine, the working fluid is hot and compressed gas with high speeds. Therefore, the heat stresses in the blade and impact on the surface of the blade should be taken into account seriously in future work. The applicability of the design should be decided by structural analysis even if the aerodynamic performances are highly efficient.

## REFERENCES

## REFERENCES

- [1] Earl Logan Jr, Turbomachinery: basic theory and applications, New York: M. Dekker, c1993
- [2] S.L. Dixon, Fluid mechanics, thermodynamics of turbomachinery, Amsterdam; Boston: Elsevier-Butterworth-Heinemann, 2005
- [3] Budugur Lakshminarayana, Fluid dynamics and heat transfer of turbomachinery, New York: Wiley, c1996
- [4] Ronald H. Aungier, Turbine aerodynamics: axial-flow and radial-inflow turbine design and analysis, New York: ASME Press, c2006
- [5] J Zhang, M Zangeneh, A 3D inverse design based multidisciplinary optimization on the radial and mixed-inflow turbines for turbochargers
- [6] Hossein Pourfarzaneh, Ali Hajilouy-Benisi, A New Analytical Model of a Radial Turbine and Validation by Experiments, IEEEAC paper#1007, Version 3
- [7] F. J. Wallace, A Systematic Approach to the Design of Radial Inflow and Mixed Flow Turbines, Bath University of Technology, 1971
- [8] C. Rodgers, Advanced Radial Inflow Turbine Rotor Program Design and Dynamic and Testing, NASA Lewis Research Center, Contract NAS 3-18524
- [9] V. A. Pukhlii, Calculation of Stresses in the Blades of A Radial Turbine, Central Scientific-Research Institute of Industrial Design, Vol. 12, No. 6, pp. 93-97, June, 1976
- [10] J. Galindo, P. Fajardo, R. Navarro, L.M. Garcia-Cuevas, Characterization of a radial turbocharger turbine in pulsating flow by means of CFD and its application to engine modeling, Applied Energy, 103 (2013) 116 – 127
- [11] Jie Gao, Qun Zheng, Comparative investigation of unsteady flow interactions in endwall regions of shrouded and unshrouded turbines, Computers & Fluids 105 (2014) 204 – 217
- [12] Wang Yunfe, Chen Huanlong, Chen Fu, Design and Numerical Simulation on Coupled Flow Field of Radial Turbine with Air-Inlet Volute, Trans. Tianjin Univ. 2015, 21: 153-160
- [13] Daniele Fiaschi, Giampaolo Manfrida, Francesco Maraschiello, Design and performance prediction of radial ORC turboexpanders, Applied Energy 138 (2015) 517 – 532
- [14] Anthony C. Jones, Design and Test of A Small, High Pressure Ratio Radial Turbine, International Gas Turbine and Aeroengine Congress and Exposition, June 13-16, 1994

- [15] S. Han, JongBeom Seo and Bum-Seog Choi, Development of a 200 kW ORC radial turbine for waste heat recovery, *Journal of Mechanical Science and Technology* 28 (12) (2014) 5231~5241
- [16] Lei FU, Zhen-ping FENG, Guo-jun LI, Qing-hua DENG, Yan SHI, Tie-yu GAO, Experimental validation of an integrated optimization design of a radial turbine for micro gas turbines, *Journal of Zhejiang University-SCIENCE A (Applied Physics & Engineering)*, 2015 16(3):241-249
- [17] K. R. Pullen, N. C. Baines and S. H. Hill, The Design and Evaluation of a High Pressure Ratio Radial Turbine, *International Gas Turbine and Aeroengine Congress and Exposition*, Cologne, Germany June 1-4. 1992
- [18] LIU Yixiong, YANG Ce, MA Chaochen, LAO DaZhong, Forced Responses on a Radial Turbine with Nozzle Guide Vanes, *Journal of Thermal Science* Vol.23, No.2 (2014) 138-144
- [19] Xuwen Qiu, Nick Baines, Performance Prediction for High Pressure –Ratio Radial Inflow Turbines, *Proceedings of GT2007*
- [20] Qinghua DENG, Jiufang NIU, Zhenping FENG, Tip Leakage Flow in Radial Inflow Rotor of a Micro-turbine with Varying Blade-shroud Clearance, *Proceedings of GT2007*
- [21] Lisheng Pan, Huaixin Wang, Improved analysis of Organic Rankine Cycle based on radial flow turbine, *Applied Thermal Engineering* 61 (2013) 606-615
- [22] V. E. Gokhberg and O. S. Sadakov, Limiting State of Radial Turbine Rotors, *UDC 621.438-235:539.4*
- [23] Ammar Benguedouar, Types of Turbomachinery Best Suited for Space Missions Requiring Power Outputs in the Range of Few kW to 1 MW, *Massachusetts Institute of Technology*, February 1988
- [24] Himanshu Nautiyal, Varun, Anoop Kumar, Reverse running pumps analytical, experimental and computational study: A review, *Renewable and Sustainable Energy Reviews*, 14 (2010) 2059–2067
- [25] SanjayV.Jain n, RajeshN.Patel, Investigations on pump running in turbine mode: A review of the state-of-the-art, *Renewable and Sustainable Energy Reviews*, 30(2014)841–868
- [26] Himanshu Nautiyal, Varun, Anoop Kumar, Sanjay Yadav, Experimental Investigation of Centrifugal Pump Working as Turbine for Small Hydropower Systems, *ENERGY SCIENCE AND TECHNOLOGY*, Vol. 1, No. 1, 2011 PP. 79-86
- [27] Tarang Agarwal, Review of Pump as Turbine (PAT) for Micro-Hydropower, *International Journal of Emerging Technology and Advanced Engineering*, Volume 2, Issue 11, November 2012

- [28] Shahram Derakhshan, Ahmad, Nourbakhsh, Theoretical, numerical and experimental investigation of centrifugal pumps in reverse operation, *Experimental Thermal and Fluid Science*, 32 (2008) 1620–1627
- [29] Shahram Derakhshan, Ahmad Nourbakhsh, Experimental study of characteristic curves of centrifugal pumps working as turbines in different specific speeds, *Experimental Thermal and Fluid Science*, 32 (2008) 800 – 807
- [30] H. Ramos, A. Borga. Pumps as turbines: an unconventional solution to energy production, *Urban Water* 1 (1999) 261-263
- [31] A. A. Williams, PUMPS AS TURBINES FOR LOW COST MICRO I-HYDRO POWER, WREX 1996
- [32] R Barriol, J Fernandez, E Blanco, J Parrondo, and A Marcos, Performance characteristics and internal flow patterns in a reverse-running pump–turbine, *Proc IMechE Part A J Power Energy* 2004;218(4):265–71.
- [33] Punit Singh, Franz Nestmann, Internal hydraulic analysis of impeller rounding in centrifugal pumps as turbines, *Experimental Thermal and Fluid Science*, 35 (2011) 121–134
- [34] Punit Singh, Franz Nestmann, An optimization routine on a prediction and selection model for the turbine operation of centrifugal pumps, *Experimental Thermal and Fluid Science*, 34 (2010) 152–164
- [35] Sharma R.L. Pumps as turbines (PAT) for small hydro, *Proceedings of the international conference on hydro power development in Himalayas*; 1998. p. 137–46.
- [36] Grant A, Bain JM. Pump turbine—the economic answer .In: *Proceedings of the international conference on small hydropower – a developing asset*; 1985.
- [37] Williams AA. The turbine performance of centrifugal pumps: a comparison of prediction methods. *Proc IMechE Part AJ Power Energy* 1994; 208:59–66
- [38] Joshi S, Holloway AGL, Chang L .Selecting a high specific speed pump for low head hydro-electric power generation. *IEEETrans*2005:603–6.
- [39] Yang SS, Derakhshan S, Kong FY. Theoretical, numerical and experimental prediction of pump as turbine performance, *Renew Energy* 2012; 48:507–13.
- [40] Derakhshan S, Mohammadi B, Nourbakhsh A. Incomplete sensitivities for 3D radial turbomachinery blade optimization, *Computers & Fluids* 2008; 37:1354–63.
- [41] Alatorre-Frenk. Cost minimization in micro hydro systems using pumps-as-turbines [PhDME thesis]. *University of Warwick*, 1994

- [42] Gulich. *Centrifugal Pumps*. Berlin Heidelberg: Springer Heidelberg Dordrecht London New York. 2010.
- [43] G Ventrone. Direct and reverse flow condition in radial flow hydraulic turbomachines. *Proc Instn Mech Engrs*, , 2000, (p. Vol 214 Part A).
- [44] Sanjay V. Jain, A. S. Effects of impeller diameter and rotational speed on performance of pump running in turbine mode. *Energy Conversion and Management*, pp. 89 (2015) 808-824.
- [45] Li Deyou, W. H. Unsteady simulation and analysis for hump characteristics of a pump turbine model. *Renewable Energy*, pp. 77 (2015) 32-42.
- [46] Luca Da Lio, Giovanni Manente, Andrea Lazzaretto, New efficiency charts for the optimum design of axial flow turbines for organic Rankine cycles, *Energy* 77 (2014) 447-459
- [47] M S Y Ebaid and Q Z Al-Hamdan, Optimization techniques for designing an inward flow radial turbine rotor, *Proc. Instn Mech. Engrs* Vol. 218 Part A: J. Power and Energy
- [48] Harold E. Rohlik, Analytical Determination of Radial Inflow Turbine Design Geometry for Maximum Efficiency, NASA TN D-4384
- [49] Harold E. Rohlik, *Turbine Design and Application*, NASA SP-290
- [50] A. Whitfield, the Application of A Computer-aided Design Technique to the Conceptual Design of Turbochargers, 96-6T-64
- [51] Emilie Sauret, Yuantong Gu, Three-dimensional off-design numerical analysis of an organic Rankine cycle radial-inflow turbine, *Applied Energy* 135 (2014) 202 – 211
- [52] Childs, S.M. (1962). Convert pumps to turbines and recover HP. *Hydro carbon processing and petroleum refiner*, 41(10)
- [53] McClaskey, B.M., Lundquist, J.A. (1976). Hydraulic power recovery turbines, ASME Conference, 19, 76
- [54] Lueneburg, R., Nelson, R.M. (1985). Hydraulic power recovery turbines, *Centrifugal Pumps: Design and Applications*
- [55] Hancock, J.W. (1963), Centrifugal pump or water turbine. *Pipe Line News*, 25-27.
- [56] Grover, K.M. (1980), Conversion of pumps to turbines. GSA Inter Corp., Katonah, New York.
- [57] Lewinsky, Keslitz (1987). H.-P. pumpen als turbinen fur kleinkraftwerke, *Wasserwirtschaft*, 77(10), 531-37
- [58] Engeda A., Rautenberg, M. (1987) Performance of Centrifugal pumps as Hydraulic Turbines", *Trans of ASME*, Vol. 43, 1987, Anaheim, USA.



- [59] Engeda A., Rautenberg, M. (1988) Comparisons of the performance of hydraulic turbines and reversible pumps for small-hydro applications, American Society of Mechanical Engineers, Fluids Engineering Division FED. 1988; 68:45-50
- [60] Engeda A., Rautenberg, M. (1988) Comparisons of the performance of hydraulic turbines and reversible pumps for small-hydro applications, fifth int. Symposium On hydro power fluid machinery, presented at ASME winter annual meeting, (Chicago, U.S.A.: Nov. 27-dec. 1988;68 ).
- [61] Engeda A., Rautenberg, M. (1988) Are Pumps Worthwhile Turbines?, International Water Power and Dam Construction. 1988; 40(7):19-20.
- [62] Stepanoff, A.J. (1957). Centrifugal and axial flow pumps. New York: John Wiley.
- [63] Alatorre-Frenk, C., Thomas, T.H. (1990). The pumps-as-turbines approach to small hydropower, World Congress on Renewable Energy, Proceedings of the 1st World Renewable Energy Congress. Pergamon Press, 5, 2914-8
- [64] Engeda A., Strate P., Rautenberg M.: (1988) Auswahl von Kreiselpumpen als Turbinen. Pumpentagung Karlsruhe'88, Sektion A6, Fachgemeinschaft Pumpen im VDMA, Frankfurt/Main, Oktober 1988
- [65] Kittredge, C.P. "Centrifugal Pumps Used as Hydraulic Turbines". Trans. ASME, Vol. 63, 1941
- [66] Knapp, R. T. "Centrifugal Pump Performance as Affected by Design Features". Trans. ASME, Vol.63, 1941
- [67] Buse, F., —Using Centrifugal Pumps as Hydraulic Turbines- Pumps as Turbines Experience Profile || , Acc. 02, IDO-10109, EG & G Idaho Inc., pp. C-1-1 to C-1-5, September1982
- [68] Hergt, P. Krieger, P. Tommes, S. (1984), Die strömungstechnischen Eigenschaften von Kreiselpumpen im Turbinenbetrieb; In: Pumpentagung Karlsruhe der Fachgemeinschaft Pumpen im VDMA, Germany.
- [69] Carlos A.M. Ventura, Peter A. Jacobs, "Preliminary Design and Performance Estimation of Radial Inflow Turbines: An Automated Approach" Journal of Fluids Engineering, MARCH 2012, Vol. 134 / 031102-1